5-2010

Design and Scale-Up of Production Scale Stirred Tank Fermentors

Ryan Z. Davis
Utah State University

Recommended Citation

Davis, Ryan Z., "Design and Scale-Up of Production Scale Stirred Tank Fermentors" (2010). *All Graduate Theses and Dissertations*. 537.
https://digitalcommons.usu.edu/etd/537

DESIGN AND SCALE-UP OF PRODUCTION SCALE STIRRED TANK FERMENTORS

by

Ryan Z. Davis

A thesis submitted in partial fulfillment
of the requirements for the degree

of

MASTER OF SCIENCE

in

Mechanical Engineering

Approved:

Dr. Heng Ban Major Professor	Dr. Timothy Taylor Committee Member
Dr. Robert Spall Committee Member	Dr. Byron R. Burnham Dean of Graduate Studies

UTAH STATE UNIVERSITY
Logan, Utah

2009

ABSTRACT

Design and Scale-Up of Production Scale Stirred Tank Fermentors

by

Ryan Z. Davis, Master of Science

Utah State University, 2009

Major Professor: Dr. Heng Ban
Department: Mechanical and Aerospace Engineering

In the bio/pharmaceutical industry, fermentation is extremely important in pharmaceutical development, and in microbial research. However, new fermentor designs are needed to improve production and reduce costs of complex systems such as cultivation of mammalian cells and genetically engineered micro-organisms. Traditionally, stirred tank design is driven by the oxygen transfer capability needed to achieve cell growth. However, design methodologies available for stirred tank fermentors are insufficient and many times contain errors. The aim of this research is to improve the design of production scale stirred tank fermentors through the development of dimensionless correlations and by providing information on aspects of fermentor tanks that can aid in oxygen mass transfer.

This was accomplished through four key areas. Empirical studies were used to quantify the mass transfer capabilities of several different reactors. Computational fluid dynamics (CFD) was used to assess the impact of certain baffle and impeller geometries.

Correction schemes were developed and applied to the experimental data. Dimensionless correlations were created from corrected experimental data to act as a guide for future production scale fermentor design. The methods for correcting experimental data developed in this research have proven to be accurate and useful. Furthermore, the correlations found from the corrected experimental data in this study are of great benefit in the design of production scale stirred tank fermentors. However, when designing a stirred tank fermentor of a different size, further experimentation should be performed to refine the correlations presented.

(114 Pages)

I would like to dedicate this thesis to my wife, Patricia.

Without her loving support I never would have finished this project.

ACKNOWLEDGMENTS

Everyone that has written a thesis knows the difficulties and hang-ups that accompany the research. My research has experimental, numerical, and analytical elements. Each of these carry with it inherent difficulties that require specific skill sets to overcome. I would like to express my thanks to all those who helped me with this project, by involving their expertise and helpfulness.

First and foremost I would like to express my gratitude for my colleague Kristan. Without her help and input I never would have finished this project. I would also like to express thanks to my advisor, Dr. Heng Ban, who patiently helped me through every stage of my research and never gave up on me. My advisors, Dr. Timothy Taylor and Dr. Robert Spall, have also added their expertise and experience to help me complete this process. I appreciate all the time and effort they have put into helping me with my research. I would also like to state my appreciation for Thermo Fisher Scientific for their partial funding of this project. Several of their engineers, especially Jeremy Larsen and Heather Kramer, have also helped with the critical thinking and design aspects for this project. I thank you all for believing in me and supporting me through this process.

Ryan Z. Davis

CONTENTS

LIST OF TABLES

Table Page

LIST OF FIGURES

NOMENCLATURE

a	*gas-liquid interfacial area per unit volume*
$A(t)$	*total surface area of gas bubbles in tank at time t*
A_0	*total surface area of gas bubbles at steady-state*
CFD	*acronym for Computational Fluid Dynamics*
C	*actual oxygen concentration of the liquid phase (%)*
C_{AL} or C_L	*dissolved oxygen concentration*
$\overline{C_{AL}}$	*final dissolved oxygen concentration*
C_{AL1} and C_{AL2}	*DO concentrations at times* t_1 *and* t_2 *respectively*
C_m	*measured oxygen concentration*
C_o	*initial oxygen concentration*
$C(t)$	*oxygen concentration in tank at time t*
C^*	*oxygen concentration in a saturated liquid (%)*
d_i	*impeller diameter*
DO	*acronym for Dissolved Oxygen*
D_L	*diffusivity of gas into the liquid*
d_t	*tank diameter*
$F(t)$	*external forcing function*
g	*acceleration due to gravity*
g_c	*dimensional constant (1 kg-m/N-*s^2*)*
G_k	*generation of turbulent kinetic energy due to mean velocity gradients*
G_b	*generation of turbulent kinetic energy due to buoyancy*
h	*time step*
h_m	*mass transfer coefficient*
H	*Henry's law constant*
H_L	*liquid height*
k	*spring stiffness constant*
k_G	*local gas phase mass transfer coefficient (*$1/m^2s$*)*
k_L	*local liquid phase mass transfer coefficient (*$1/m^2s$*)*
K_G	*overall gas phase mass transfer coefficient*
K_L	*overall liquid phase mass transfer coefficient*
k_La	*volumetric mass transfer coefficient*
k_La_{ss}	k_La *measured from steady-state model*
k_La_t	k_La *measured from transient model*
J	*molar flux*
m	*mass*
n	*number of impellers*
N	*mixing speed*
N_P	*impeller power number*
Pe	*Peclet number*
P	*power input*
P_{dp}	*percent of data points within the transient time period*

P_k	percent change in k_La
p^*	oxygen pressure at equilibrium
p_G	oxygen partial pressure
q	gas flow rate
Re	Reynolds number
s	displacement
STRs	acronym for Stirred Tank Reactors
Sc	Schmidt number
Sh	Sherwood number
t	time
t_0	time when steady state is achieved
t_{95}	time required to reach 95% oxygen saturation
t_m	mixing time
t_{trans}	time of the transient volume rise
U_{cdp}	uncertainty of a corrected data point
$U_{\tau 1}$	uncertainty of τ_1
$U_{\tau 2}$	uncertainty of τ_2
U_{Cb}	bias uncertainty of dissolved oxygen concentration
V	liquid volume
V_0	steady-state liquid volume
$V(t)$	volume of gas in tank at time t
v_s	superficial gas velocity

α	volume rate coefficient
β	surface area rate coefficient
ζ	ratio of first and second time constants (τ_1/τ_2)
ζ_d	damping coefficient
μ	viscosity
ρ	liquid density
σ	surface tension
τ	time constant
υ	kinematic viscosity

CHAPTER 1

INTRODUCTION

Fermentation can be defined as the metabolism of sugars by microorganisms. The term is used by microbiologists to describe any process for the production of a product by means of the mass culture of a microorganism [1]. Fermentation has been practiced worldwide since ancient times in the processing of many familiar food products [2]. However, since WWII fermentation has spread to more applications and is now used in many areas [1]. The modern biotechnology era can be traced to the mid-1970s with the developments of recombinant DNA and hybridoma technologies. Thus far, the most prominent applied impact of these technologies has been the successful development of biotech-derived therapeutic agents – the biopharmaceuticals [3].

In the Bio/Pharmaceutical industry today, fermentation is extremely important in the development of pharmaceuticals and health products, and in microbial research. To achieve cell growth this industry relies heavily on stirred tank reactors (STRs) which introduce nutrients and oxygen into various medias in order for cells to survive and grow. The design and scale-up of STRs is typically performed via experimental means due to the complex nature of cell kinetics and mass transfer in these applications. The design of STR's generally begins with obtaining lab scale results from laboratory scale fermentors. A particular operating or equipment variable is then held constant to scale the system [4] [5]. These variables can include specific power input, impeller tip speed, mixing time, mass transfer, or a combination of these. There are many theories as to which of these variables is the most important and thus which to hold constant in the scaling process. Extensive research has been done to prove that some of these variables should be scaled.

Thus far, different researchers have not reached a consensus as to which variable(s) should be held constant [6, 7, 8, 9].

Results from practice show that new reactor designs are needed to improve production of complex systems such as cultivation of mammalian cells and genetically engineered micro-organisms [6]. With the recent surge in production of bio-fuels there is an anticipation of an increase in the market for cell cultivation. This surge will be supported with improved fermentor design. With these improvements in fermentor design, several industries (i.e. bio-fuels, pharmaceuticals, genetic engineering, etc.) will be able to increase production and reduce costs which will, in turn, benefit the economy.

Stirred tank design is difficult because of the highly experimental approach used by researchers. The most difficult part of the design is matching the fermentor capability to the oxygen demand of the fermentation culture [10, 11]. Some general guidelines have been offered on how to improve mass transfer in stirred tank reactors. In addition some correlations have been formed to provide predictions on stirred tank performance. However, the guidelines offered do not provide information on how different aspects of the tank (i.e. impeller and baffle geometry) specifically effect oxygen transfer in stirred tanks. The correlations offered do not provide a wide enough range of tank sizes, power inputs or gas flow rates to be useful to more than just a handful of people. In addition, the experimental methods used by researchers in this area are not well documented. This means that errors could exist in the data due to probe response times and unsteady state measurements.

This research has improved the design process of stirred tank fermentors by developing dimensionless correlations. In addition the efficacy of different baffle and impeller types in STRs were assessed. This was accomplished through four key areas. First, empirical studies were used to quantify the mass transfer capabilities of several different reactors; second, computational fluid dynamics (CFD) was used to assess the impact of certain baffle and impeller geometries; third, correction schemes were developed and applied to the experimental data; and fourth, dimensionless correlations were created to act as a guide for future production scale fermentor design.

CHAPTER 2

LITERATURE REVIEW

Biological Reactors

Fermentation Technology

Biological reactors vary in technical sophistication from the primitive banana leaf wrappings to modern, highly automated, machines. Common fermentors used in today's industry include the following: tray fermentors, static bed/tunnel fermentors, rotary disk fermentors, rotary drum fermentors, fluidized beds, agitated tank fermentors, and continuous screw fermentors [3]. One of the most common fermentors used on a large scale, and the type this thesis is concerned with, is the agitated/stirred tank fermentor. The stirred tank fermentor can be divided into two subsets: the bioreactor, which is used for mammalian cells, and the fermentor which is used for bacteria, yeasts, and algae. The bioreactor is typically utilized when growing cells that are sensitive to shear and have less of an oxygen demand. The fermentor is typically used for cells that are more robust, tolerant of high shear rates and have higher oxygen demands.

Mass Transfer in Stirred Tank Fermentors

The oxygen demand of the cells in stirred tank fermentors plays a vital role in cell culture and growth. For this purpose, fermentors typically employ a sparge located near the bottom of the tank to introduce air into the media. Fermentors also employ one, or several, impellers to provide bubble break up and bulk mixing of the media. Since the organisms used in fermentation generally have a large oxygen demand, the sparge and impellers of a fermentor are typically designed with mass transfer in mind. During the aerobic bioprocess oxygen is transferred from a gas bubble into a liquid phase and ultimately to the microbe that uses the oxygen to survive and grow. The transport of oxygen from air bubbles to these cells can be represented by a number of resistances as shown in Figure 1.

According to the two film theory [13], the flux through the gas film and the liquid film can be modeled as the product of the driving force and the mass transfer coefficient:

$$J = k_G(p_G - p_i) = k_L(C_i - C_L) \tag{1}$$

In this equation, the subscript *G*, *L* and *i* represent the gas, the liquid and the interface between the two respectively [12].

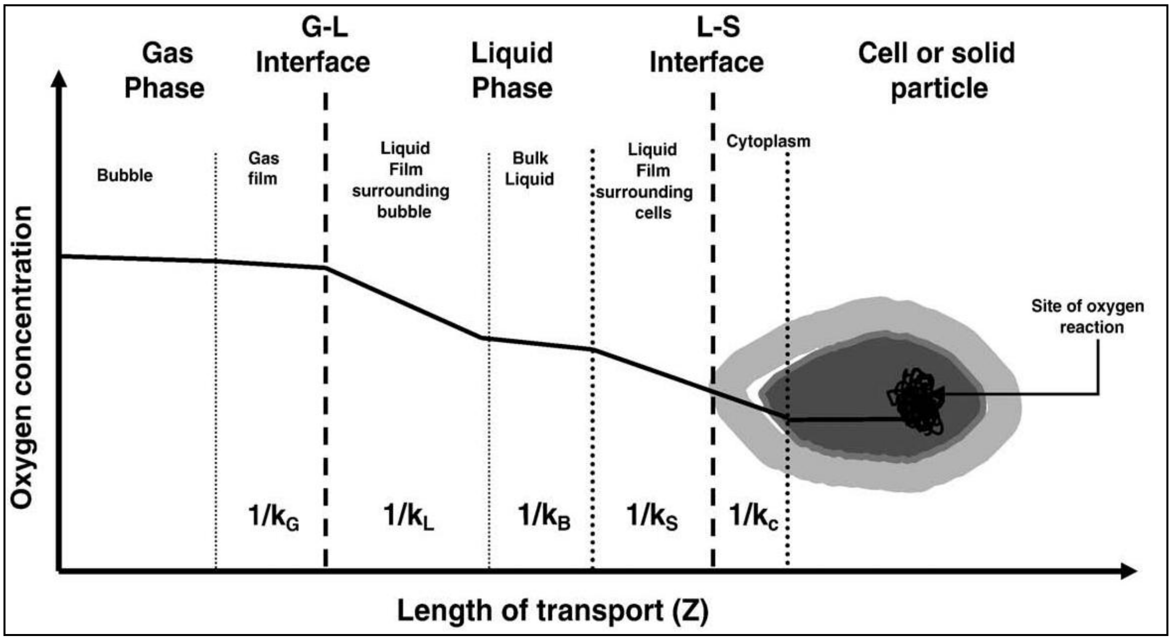

Figure 1: Schematic showing the resistances to oxygen mass transfer in the aerobic bioprocess. (Taken from Gomez and Ochoa 2008 [12])

Since the interfacial concentrations are not directly measureable, we can consider the overall mass transfer coefficients and Equation (1) can be written as:

$$J = K_G(p_G - p^*) = K_L(C^* - C_L) \tag{2}$$

where C^* is the oxygen saturation concentration according to Henry's law ($p^*=HC^*$.) Combining Equations (1) and (2) we obtain the following relation:

$$\frac{1}{K_L} = \frac{1}{Hk_G} + \frac{1}{k_L} \tag{3}$$

Since oxygen is only slightly soluble in water (H>>1) it is commonly accepted that the overall mass transfer coefficient is equal to the local mass transfer coefficient (i.e. $K_L=k_L$). From this we can find the oxygen mass transfer rate per unit of reactor volume by multiplying the overall flux by the gas-liquid interfacial area per unit of liquid volume, a:

$$N = a \cdot J = k_L a \cdot (C^* - C_L) \tag{4}$$

Due to the difficulty of measuring k_L and a separately, usually the product k_La is measured as a lumped term and characterizes the mass transport from gas to liquid [12]. The volumetric mass transfer coefficient, k_La, is often used as a quantitative measure of fermentor performance [14].

Stirred Tank Design and Scale-Up

Stirred Tank Design Guidelines

Stirred-tank fermentors typically follow general guidelines in order to optimize mixing and reduce power requirements. Extensive research has been performed to give guidelines on sizing of stirred tank fermentors and their components. However, none of these guidelines are absolute; rather they are meant to direct the basic geometric design of stirred tank fermentors while other factors are held constant. These guidelines are outlined in the following paragraphs.

Impellers: The ratio of the impeller diameter to the diameter of the tank (d_i/d_t) should be between 0.3 and 0.5. In the case of using radial flow impellers the ratio should be approximately 0.3. If the impellers are too small they will not generate enough fluid movement, whereas if they are too large they require much more power and become less efficient [15]. Typically stirred tank fermentors employ Rushton turbines using either a single impeller or a set of impellers for tank mixing. Recent developments in impeller design have led to the use of several different types of impellers (e.g. Smith, He3, A320, Intermig) [16]. Even though these new types of impellers claim to produce better mixing and have less power consumption, typical fermentors only employ standard Rushton turbines.

Impeller Spacing: The spacing between impellers should be $1.0d_i$ to $2.0d_i$, where d_i is the diameter of the impeller. In addition, the bottom-most impeller should be located $1.0d_i$ from the bottom of the tank [15, 17]. If the impellers are spaced too close together (less than $1.0d_i$) the power imparted to the fluid can get as low as 80% of that obtained from proper spacing. On the other hand, if the impellers are spaced too far apart the fluid does not experience adequate mixing [17]. Thus, the number of impellers can be determined from the following equation:

$$\frac{H_L - d_i}{d_i} > n_i > \frac{H_L - 2d_i}{2d_i} \tag{5}$$

where H_L is the height of liquid in the vessel and n_i is the number of impellers [17].

However, this is assuming all the impellers are spaced equally between the bottom of the tank and the liquid surface. As stated before, the bottom-most impeller is usually spaced one impeller diameter from the tank bottom, and the upper-most impeller is spaced 1.5 or more impeller diameters from the liquid surface.

Baffling: Stirred tank fermentors generally use baffles because of the need to disrupt the bulk fluid flow in the tank. Bioreactors do not need this disruption. In most cases, four flat baffles on 90° centers are used and have a width of $.08d_t$ to $.10d_t$, where d_t is the diameter of the tank [15]. For low-viscosity flows baffles are attached directly to the wall of the tank, but for moderate to high-viscosity flows baffles are set a small distance away from the wall [18]. While the flat, four-baffle configuration is most common, other sizes, shapes and number of baffles have been researched, but only on a limited basis [19].

Tank Height: The height to diameter ratio of the tank is typically between 2.0 and 3.0; however, taller tanks (up to H_L/d_t=4.0) have been used to reduce the power requirement of the impellers [20]. Typical tanks also employ a dish-shaped bottom to enhance mixing and prevent dead zones.

Empirical Design and Scale-Up of Stirred Tank Fermentors

Design and scale-up of stirred tank fermentors are largely based on empirical data. Some research suggests that the design of stirred tanks should be based on mixing time, while others claim it should be based on the specific power input [21]. Others argue it should be based on impeller tip speed [22]. A few researchers have suggested dimensionless number correlations be used for reactor scale-up and design [12]. Scale-up strategies usually maintain one of these factors constant, along with k_La, and base the rest of the design as close to the preceding design criteria as possible [21, 22]. Many of these strategies are used to design fermentors; however, none can accurately define what advantages one scale-up strategy has over others.

Challenges in Design and Scale-Up

The most difficult task in tank design is getting the fermentor capability to match the oxygen demand of the fermentation culture [10, 11]. When designing a stirred tank fermentor, the main concern is providing sufficient oxygen to the cells without exceeding any limits of shear or power consumption. For example, it is possible to obtain higher values of k_La by simply increasing the impeller speed. However, this causes a great increase in impeller tip speed which can damage the organisms because of the increased shear. The increase in tip speed also creates an exponential increase in power consumption which can make the fermentation uneconomical. In order to avoid these pitfalls, correlative models can be used by imposing limits on power consumption and impeller tip speed. With this, the rest of the tank can be designed to match the oxygen demand of the organisms being fermented.

Computational Fluid Dynamics (CFD)

CFD History and Uses

Computational fluid dynamics is one of the branches of fluid mechanics that uses numerical methods and algorithms to solve and analyze problems that involve fluid flows. Flow fields are discretized into small nodes and the finite volume technique is used to calculate fluid flows in and around complex geometries. CFD codes were originally developed as codes to analyze the potential flow around 2-D airfoils as early as the 1930's. However, computer speed and power was not sufficient to calculate 3-D codes until the 1960's when numerous panel codes were developed to analyze airfoils. Since the 1960's CFD codes have been adapted to meet almost any type of fluid flow application and are used in almost every industry that deals with complex fluid flow [23]. Because of the expense and expertise involved in performing CFD analyses it has traditionally only been used in research applications to design and analyze complex flows. However, because of availability of commercial codes and technology advances, CFD is spreading rapidly into the commercial sector.

CFD Analyses Used in the Design and Scale-Up of Stirred Tank Fermentors

The first instances of CFD being used in fermentor development came about through studying the steady-state flow field. Using a visualization of the flow field researchers could study how the media in the tank interacted with the various geometries within the tank. One of the first developments utilizing this technique was impeller design. Around 1990 several papers were published on flow field computation and the development of different types of impellers with experimental verification [16, 24]. These studies modeled several different shapes and sizes of impellers to show how the fluid flow was affected in stirred tanks. The goal of these studies was to find impellers that produced equal mixing capability for less power consumption compared to the traditional Rushton type impeller. These studies all verified the flow field computation using Laser Doppler Velocimetry or Particle Image Velocimetry and stated that computational predictions will not eliminate the need for experimental validation of a proposed design. Complex physical phenomena, such as two phase flooding, free-surface waves, and air entrainment can arise in mixing equipment and are unlikely to be accurately predicted given the enormous complexity of such flows [24, 25].

Another early development in CFD analysis of stirred tank fermentors was calculating mixing times for different tank configurations. By injecting neutrally buoyant particles into the flow field and calculating the time to reach homogeneity, stirred tanks can be quantitatively compared to one another [16, 26]. The mixing time of stirred tanks has been used to model the effectiveness of not only mixers, but also STRs where mass transfer is an important design factor. Several studies have shown that reactors which produce faster mixing times will have better mass transfer rates and reaction kinetics than reactors with slower mixing times [27, 28].

Many fermentors involve sparging air into the reactor to feed the reaction taking place. Accordingly, recent computational studies of STRs have been focused on modeling bubbles within the flow field. The earliest of these studies aimed at predicting how bubbles affect the flow field [29, 30]. Even though they are few in number, recent studies attempt to show how the mass transfer from the bubbles is affected by impeller, baffle, and tank geometries [31]. Being able to quantify the mass transfer capabilities of a stirred tank fermentor using only CFD is the ultimate goal. To date these technologies are still unproven, so the CFD used in this field is still largely based on mixing time calculations.

Empirical Correlations Used in the Analysis of
Stirred Tank Fermentors

Dimensionless Correlations

Dimensionless number correlations are used in several fields of engineering (i.e. heat transfer, fluid flow, etc.) where geometries make it difficult or impossible to find an analytical solution or where scaling of the system is required. In this study both of these conditions apply. The impellers, baffles, and tank shape take part in complex fluid flows that are impossible to predict analytically, which makes it necessary to create empirical correlations that help calculate the parameters needed in stirred tank design.

Normally dimensionless correlations for stirred tank reactors come as a Sherwood number correlation of the following form:

$$Sh = f(Re, Sc, Pe) \tag{6}$$

$$Re = \frac{\rho V d}{\mu} \tag{7}$$

$$Sc = \frac{\mu}{\rho D} \tag{8}$$

$$Pe = \frac{Vd}{D} \tag{9}$$

Equation (6) shows that the Sherwood number is given as a function of the Reynolds number (Re), Schmidt number (Sc), and the Peclet number (Pe). Even though this is not always the case, all dimensionless number correlations used for stirred tank fermentors do relate an equation of tank inputs to a dimensionless number associated with k_La [7, 32, 33, 34]. These correlations serve to predict k_La values for a given tank geometry. Few dimensionless number correlations have been published to date. Those that have include vastly different ranges of power input, gas flow rate and tank geometry. This wide range of correlations, since they are few in number, serve very little purpose in providing accurate k_La values unless they are used for very specific tank geometries [12].

Errors in Empirical Data

It has been shown that k_La estimates can be biased by the probe response time of a dissolved oxygen probe [35]. This error particularly occurs if the inverse of k_La is of the same or lesser order as the response time of the electrode [12]. This is generally the case for highly aerated fermentation vessels with traditional dissolved oxygen probes. Thus, the response time of a dissolved oxygen probe is one of the largest sources of error in k_La determination. A correction to the traditional probe response is required to determine correct oxygen transfer values.

Accurate k_La determination by the unsteady-state method is also affected by a transient volume rise due to gas hold-up. The volumetric mass transfer coefficient, k_La, is meant to be a steady-state measurement of the mass transfer in a reactor. However, when air is sparged into the tank, the liquid volume rises due to gas hold-up. Even if the duration of this transient state is much less than the duration of the dissolved oxygen measurement, it still has the possibility of introducing error into the calculation of k_La.

Due to the lack of publication in this area it is likely this phenomenon has never been researched. Its study, however, will enhance the understanding of mass transfer in stirred tanks and reduce the error introduced into mass transfer calculations.

Errors in Dimensionless Correlations

The errors discussed in the previous section are of great importance to the validity of dimensionless correlations that have already been developed. In the reports where these correlations are presented usually there is no mention of how the data was collected [7, 12, 22, 32, 33]. This leads us to believe that there is a possibility of errors in the data. For this reason, existing correlations will be examined to determine if they are useful in stirred tank design. If the existing correlations do not correlate with new data, new correlations (or new coefficients for existing correlations) will need to be developed.

CHAPTER 3

OBJECTIVES

The overall goal of this project was to develop tools to enhance the design process of production scale fermentors. The specific objectives were to:

- Determine how different impeller and baffle geometries affect the mass transfer and mixing of a stirred tank fermentor.
- Examine the possibility of a correlation between mixing time and mass transfer in a stirred tank fermentor.
- Create a method for correcting data obtained from a dissolved oxygen probe that has a long response time.
- Develop a technique for correcting data obtained during the transient volume rise of the unsteady-state k_La measurement technique.
- Develop a dimensionless correlation that is able to accurately predict k_La values for different geometries of production scale fermentor tanks.

CHAPTER 4

PROCEDURE

Experimental Setup

The tests for this study were carried out in a 250 L stirred tank with a dish shaped floor. The tank was 66 inches tall and 18.625 inches in diameter giving it a 3:1 height to diameter ratio for the working volume. The tank was made of clear plastic acrylic so as to have the ability to observe flow patterns in the tank while conducting experiments. Five probe holes were built into the side of the tank to allow the dissolved oxygen sensors to pass through into the liquid. The impellers used in these studies had a diameter of either 6.0 or 6.25 inches. This gives impeller diameter to tank diameter ratios of .32 and .36. Rushton, Smith, Lightnin A320 and Chemineer He3 impellers were all used in this study. These impellers are pictured in Figure 2 through Figure 5. The bottom-most impeller for each configuration was placed 6.0 inches from the bottom of the tank and the upper-most impeller was placed 10.0 inches from the ungassed liquid surface. The remaining impellers were spaced evenly between these two. The system schematic and the tank, with impeller and probe locations, are pictured in Figure 6 and Figure 7.

These experiments studied the effect of having three or four impellers on the drive shaft. As mentioned earlier, commercial fermentors do not always follow published guidelines for impeller spacing. For the 3 and 4-impeller configurations the impellers were spaced 19.5 and 13.0 inches apart, respectively. To prevent bulk fluid movement, four baffles on 90° centers were placed in the tank. Three types of baffles were tested.

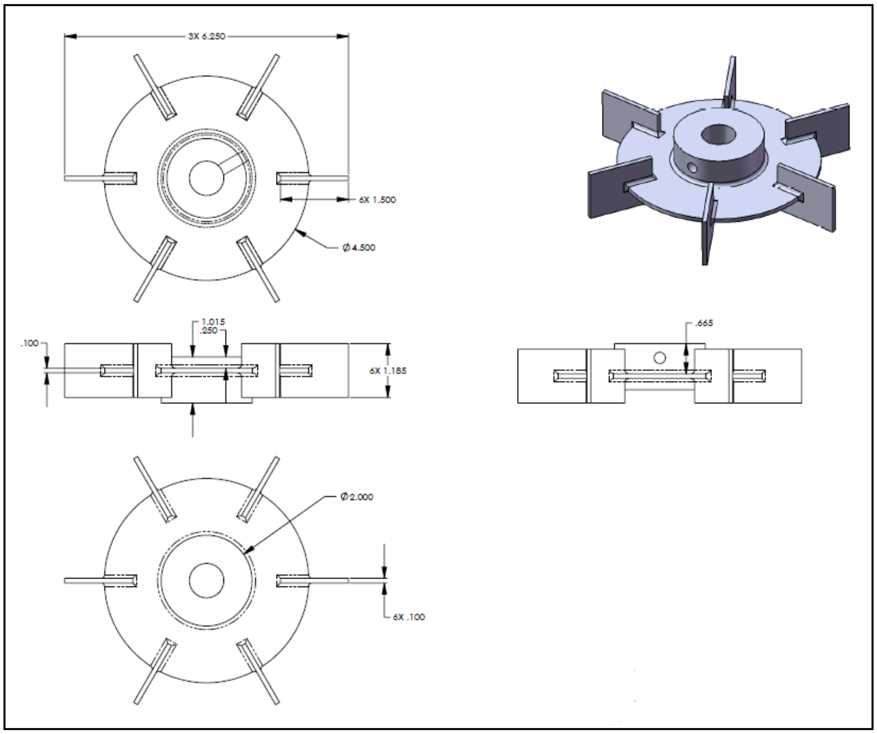

Figure 2: Rushton turbine impeller.

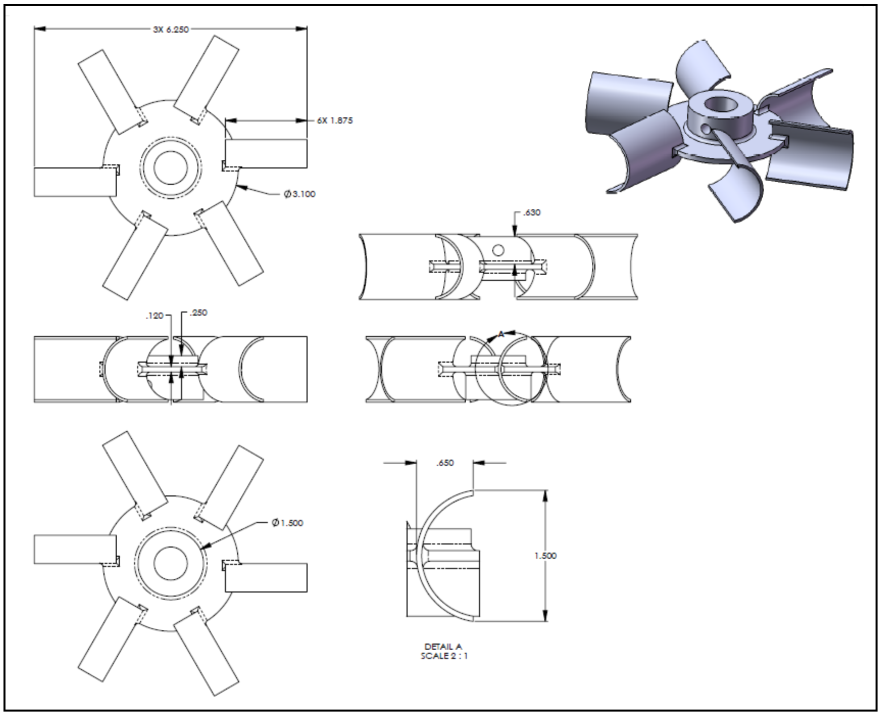

Figure 3: Smith turbine impeller.

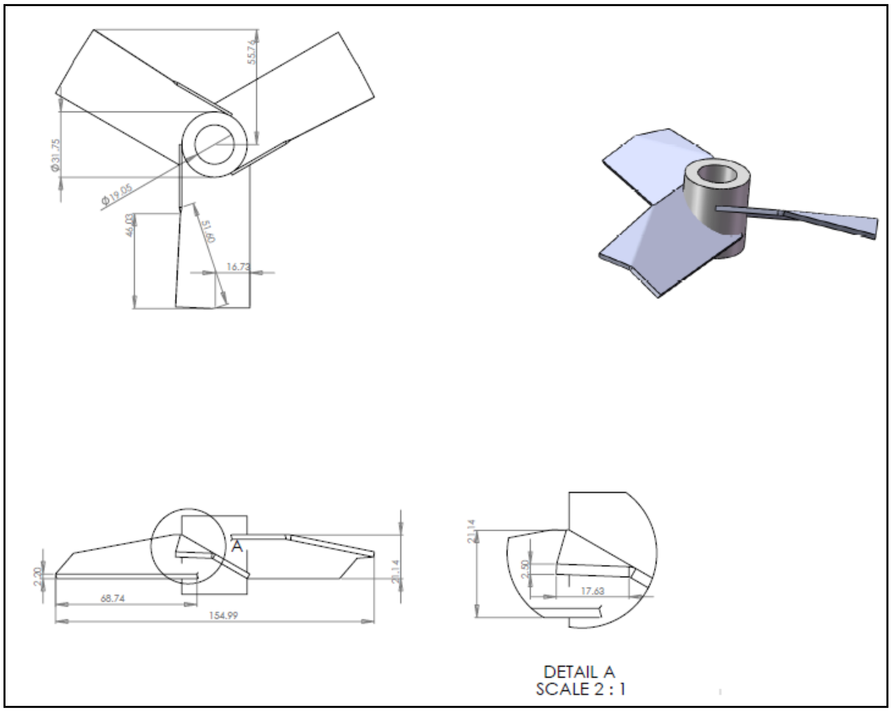

Figure 4: He3 axial flow impeller.

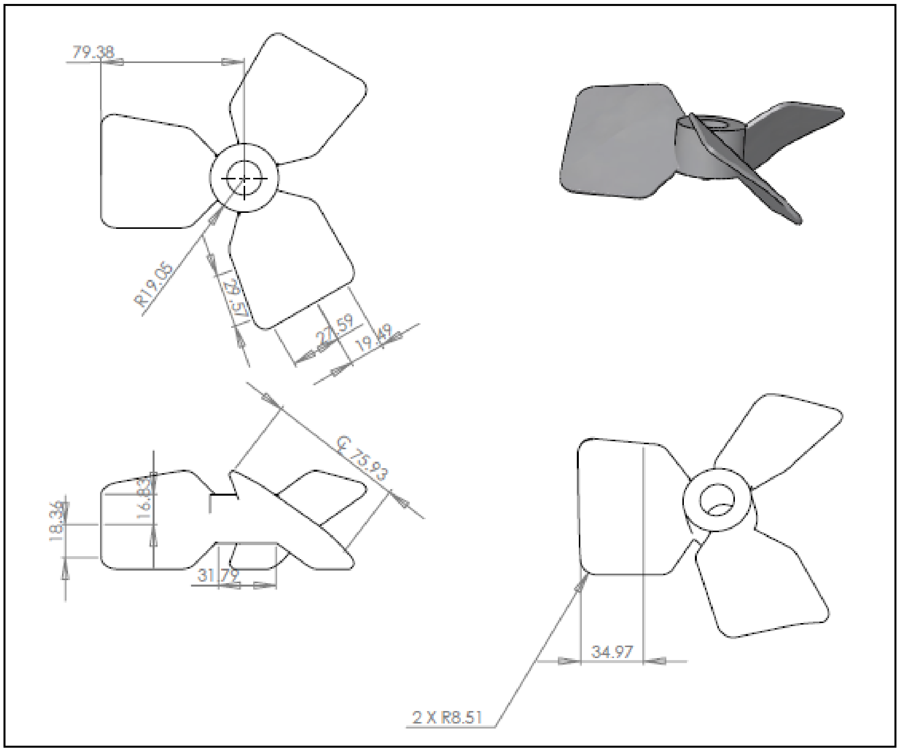

Figure 5: A320 axial flow impeller.

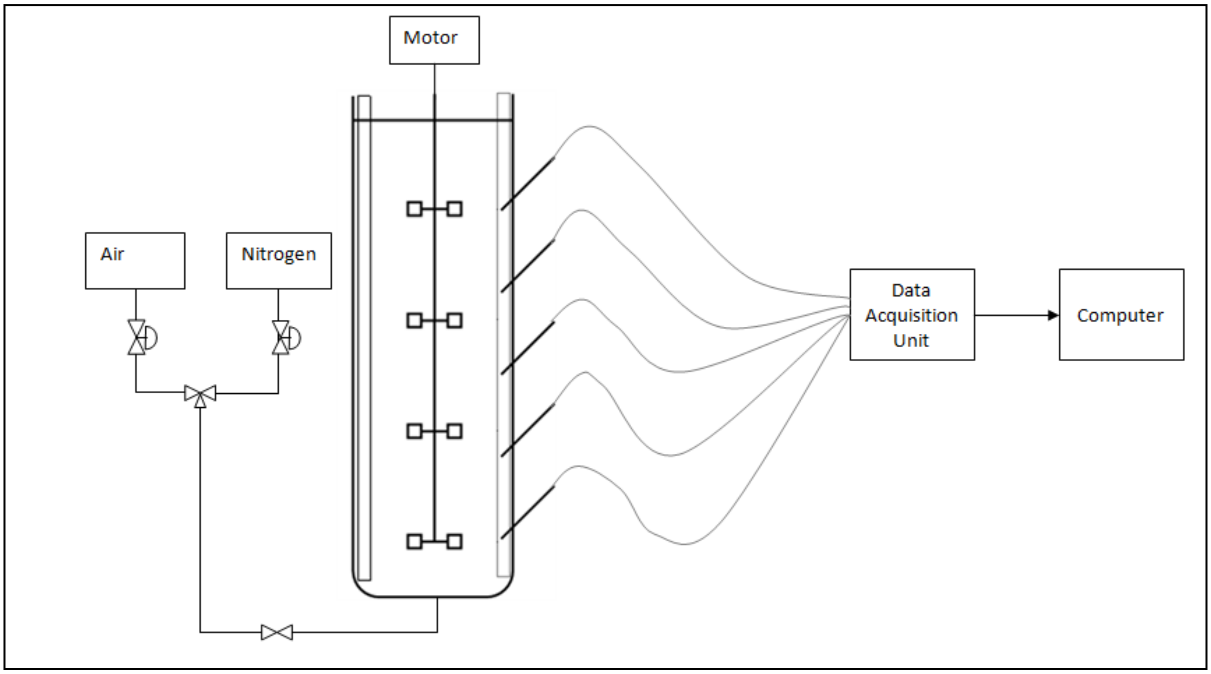

Figure 6: Schematic of test tank setup.

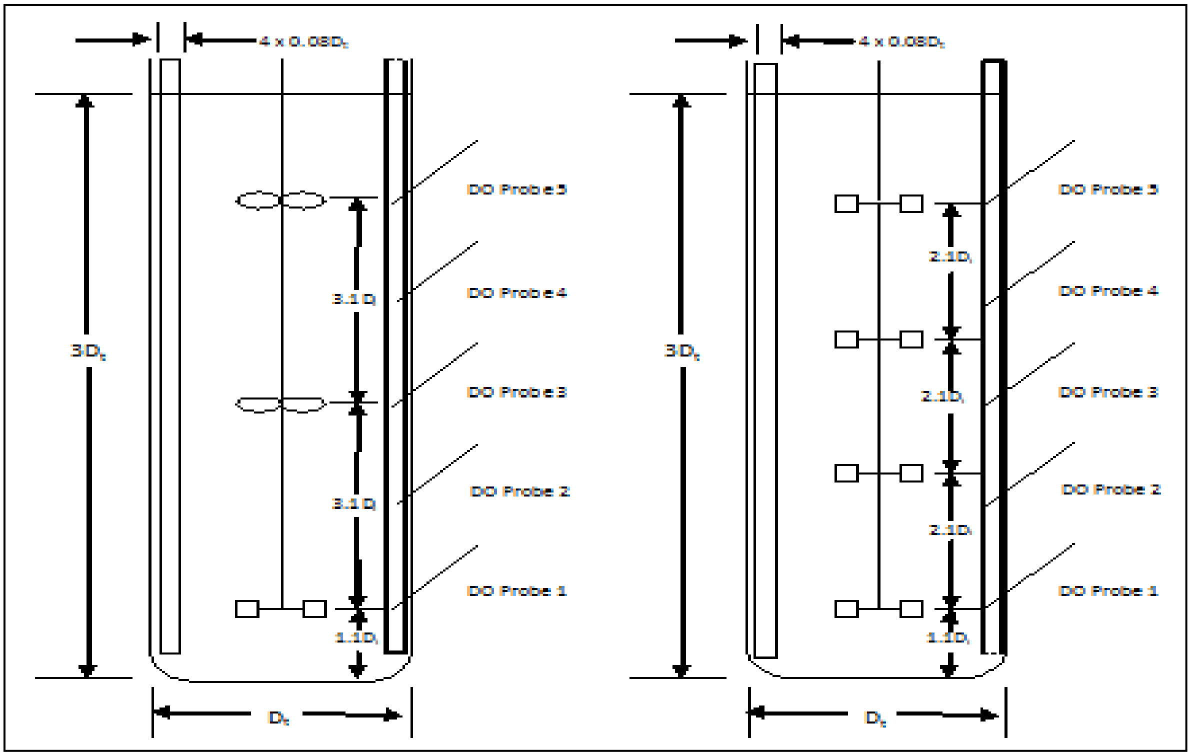

Figure 7: Picture of test tank with dimensions of impellers and probe locations.

The first type is a more traditional flat baffle measuring 1.55 inches tall standing straight out from the tank wall. This baffle was spaced .25 inches off the wall as to follow traditional baffle design. The second type of baffle was one of two semi circles protruding from the tank wall with radii of either .75 inches or 1.5 inches. The third type of baffle studied was exactly like the flat traditional type baffle, only with a simulated plastic film draped over the baffle. A list of configurations that will be used and what studies they were used in are provided in Table 1 and Table 2.

Table 1: 3-Impeller Tank Configurations and in Which Studies They Were Used

Impeller Configuration	Baffle Configuration	Experimental Determination of k_La	CFD: Steady-State Calculation	CFD Mixing Time Calculation	Dimensionless Correlation
He3 He3 Rushton	Flat	Yes	Yes	Yes	No
He3 He3 Smith	Flat	Yes	Yes	Yes	Yes
He3 He3 Smith	Lg. Round	No	Yes	Yes	No
A320 A320 Rushton	Flat	Yes	Yes	Yes	No
A320 A320 Smith	Flat	Yes	Yes	Yes	Yes
Rushton Rushton Rushton	Flat	No	Yes	Yes	No
Rushton Rushton Rushton	Sm. Round	No	Yes	Yes	No
Rushton Rushton Rushton	Lg. Round	No	Yes	Yes	No

Table 2: 4-Impeller Tank Configurations and in Which Studies They Were Used

Impeller Configuration	Baffle Configuration	Experimental Determination of k_La	CFD: Steady-State Calculation	CFD: Mixing Time Calculation	Dimensionless Correlation
Rushton Rushton Rushton Rushton	Flat	Yes	Yes	Yes	Yes
Rushton Rushton Rushton Rushton	Film	Yes	Yes	Yes	No
Smith Smith Smith Smith	Flat	No	Yes	Yes	No
Smith Smith Smith Smith	Lg. Round	No	Yes	Yes	No
He3 Rushton Rushton Rushton	Flat	No	Yes	Yes	No
He3 He3 Rushton Rushton	Flat	No	Yes	Yes	No
He3 Smith Smith Smith	Flat	No	Yes	Yes	No
He3 He3 Smith Smith	Flat	No	Yes	Yes	No

Experimental Determination of the Volumetric Mass Transfer Coefficient: k_La

There are several techniques for determining the volumetric mass transfer coefficient. All of the techniques have advantages and disadvantages, but when measuring k_la the most common, and usually the most accurate, is the unsteady-state method [36]. For this method first the water in the tank is deoxygenated by sparging nitrogen until the dissolved oxygen (DO) in the tank reaches below 10% of the saturation level. Then air is reintroduced into the tank through the sparge at a known mass flow rate while the DO is monitored over time. This is monitored until the oxygen reaches close to 85% of the saturation level. Equations (10) through (12) describe the calculation of k_La.

$$\frac{dC_{AL}}{dt} = k_L a(\overline{C_{AL}} - C_{AL}) \tag{10}$$

$$k_L a = \frac{ln\left(\frac{\overline{C_{AL}} - C_{AL1}}{\overline{C_{AL}} - C_{AL2}}\right)}{t_2 - t_1} \tag{11}$$

In these equations C_{AL} is the dissolved oxygen concentration in percentage of saturation, t is time, $\overline{C_{AL}}$ is the final DO concentration and C_{AL1} and C_{AL2} are the DO concentrations at times t_1 and t_2, respectively. When several dissolved oxygen concentration points have been collected over time, Equation (4) applies [37]:

$$ln(\overline{C_{AL}} - C_{AL}) = -k_L at \tag{12}$$

Figure 8 illustrates the oxygen concentration over time during unsteady-state testing for determination of k_La.

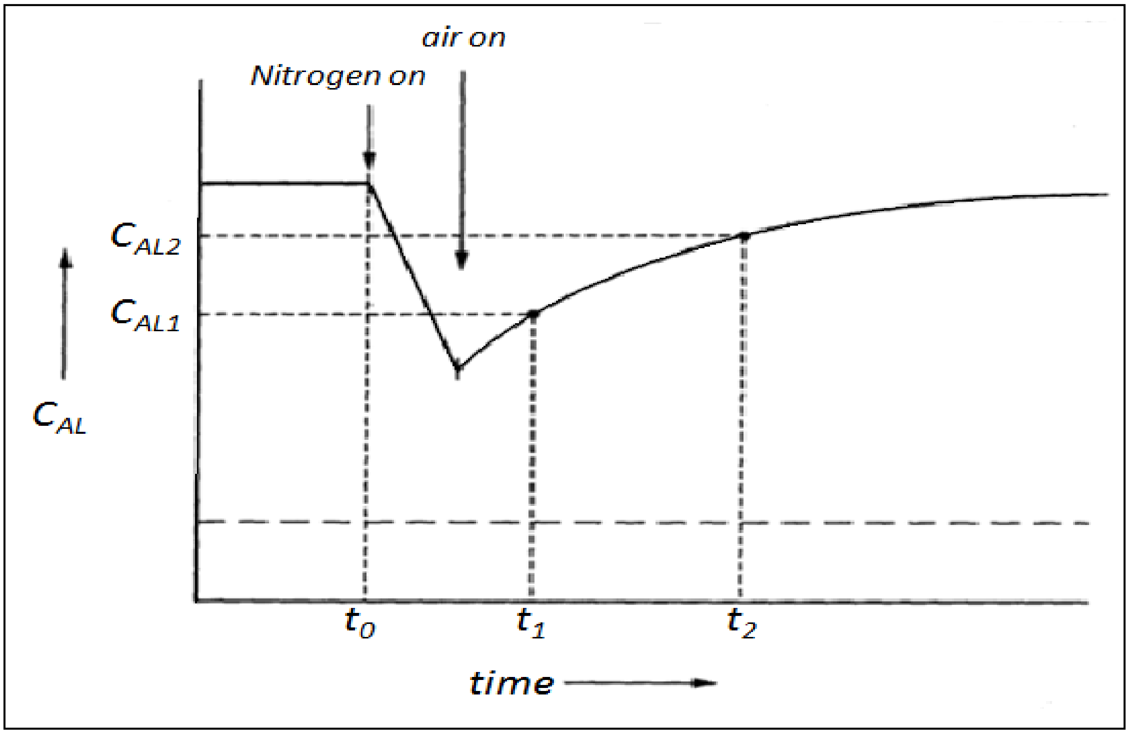

Figure 8: Graphical representation of the dissolved oxygen concentration during the unsteady-state test.

For the configurations outlined in Table 1 and Table 2 the unsteady-state method was used to give k_La values which serve as a quantitative comparison of the tanks. The volumetric mass transfer coefficient was determined at several points throughout the tank to give a volume-averaged mass transfer coefficient for each configuration. This data was used to empirically derive the dimensionless correlations. It also assisted in assessing the mass transfer capabilities of specific impellers and baffles.

Computational Fluid Dynamics Calculations

Setup of CFD Models

The second tool used in this study to enhance reactor design was computational fluid dynamics (CFD). The entire basis of CFD is formed on discritizing a fluid volume into cells and using a finite difference technique to approximate fluid properties in each of those cells. This general discritization is referred to as “meshing” or “creating a mesh.” There are several software packages used for meshing, but for this study the program “Gambit” was used. Gambit functions as both a solid modeling tool and as a meshing tool. It can also import certain types of solid models and create meshes from those models.

The models for this research were created in Solid Works® and imported into Gambit as Step files. Once the models were imported, they were slightly modified (i.e. removing fillets) to assist in the meshing process and the mesh was created for the fluid volume in the tank. The head space in the tank was not modeled; rather, a pressure outlet boundary condition was used, which allows mass to flow in and out across the boundary. Gambit was also used to apply boundary conditions to the surfaces and interior regions of the volume being meshed. These meshes were then exported for use in the CFD package FLUENT. An example of the mesh around a Rushton impeller is given in Figure 9.

For this study a 3D mesh using tetrahedral cells was used. The mesh was created by specifying the node spacing on the surfaces of the tank, baffles and impellers. All of the surfaces of the impellers were specified with 0.05 inch spacing. The surfaces of the rotating reference frame, the baffles and the impeller shaft were specified with 0.2 inch spacing. The node spacing of the tank walls and the interior of the tank was specified at 1.0 inch intervals. However, the “pave” and “tgrid” features were used when meshing which adapt the spacing as the mesh approaches surfaces with more nodes. Using less dense grids caused divergence in calculating the solutions. For several of the calculations

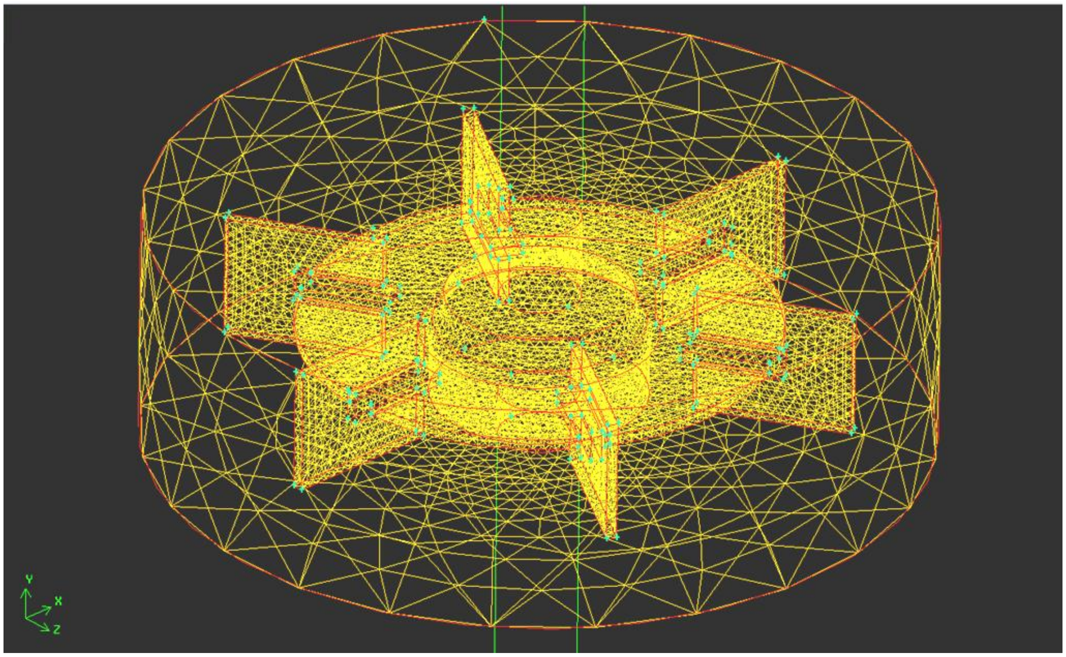

Figure 9: Rotating reference frame mesh surrounding a Rushton turbine impeller.

a polyhedral mesh was used to decrease computation time. Figure 10 and Figure 11 show the tetrahedral and polyhedral meshes, respectively.

Grid convergence and time step convergence tests were performed and shown to not affect the results of mixing time or velocity profiles. Figure 12 shows an example of the residuals over iterations for the A320-A320-Smith configuration; most of the configurations converged in a similar way. All of the models created for this study were run for 3000 iterations or more and the residuals on each of them converged to within one order of magnitude of each other. The continuity always converged to a point between 10^{-3} and 10^{-4}. The turbulent kinetic energy and the x, y, and z-velocities converged to 10^{-5} +/- one half order of magnitude. The turbulence dissipation rate (epsilon) converged to 10^{-4}, or very close to it in every case.

CFD uses the pressure flow field to calculate the velocity formation, which can be

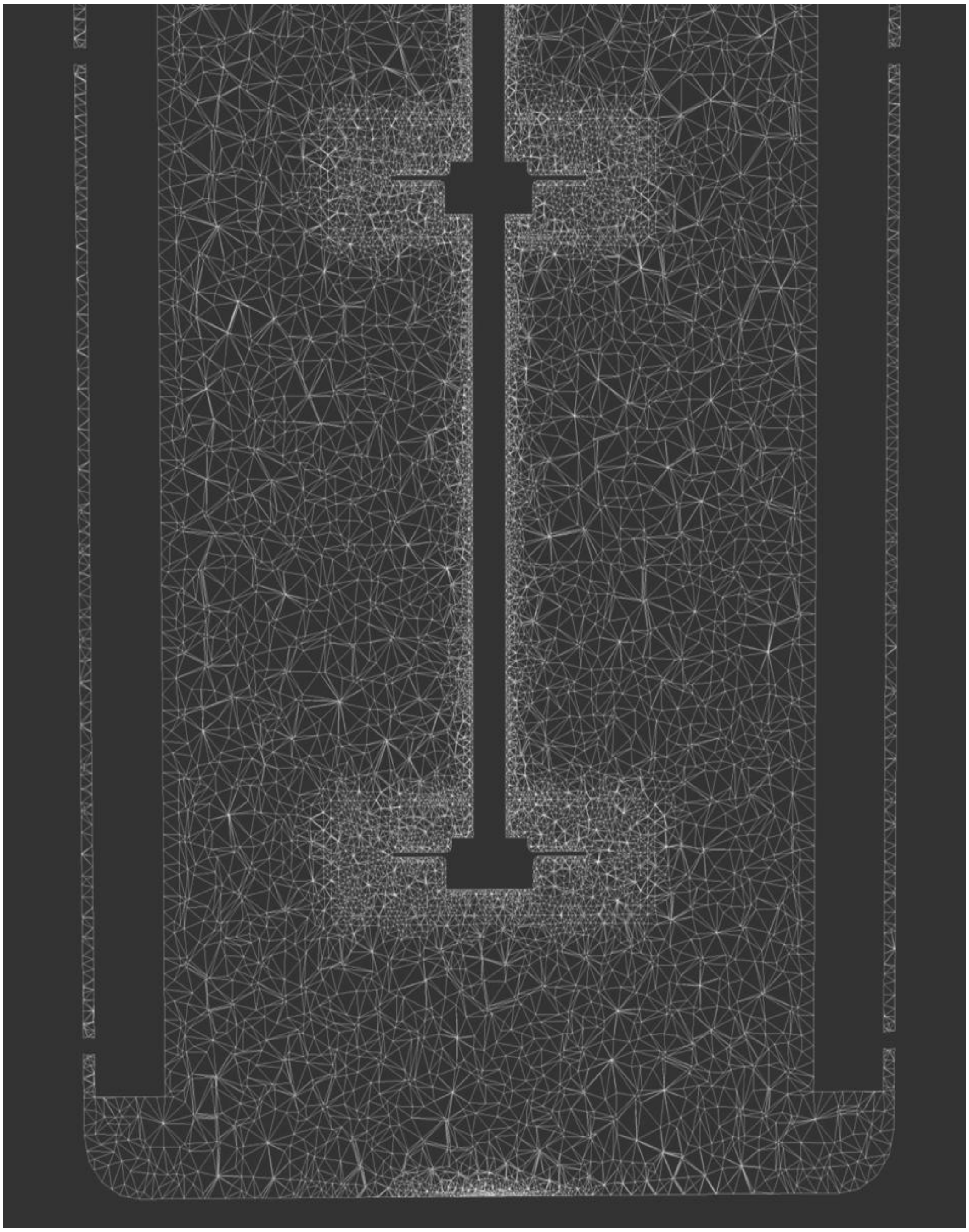

Figure 10: Picture of the tetrahedral mesh.

calculated using a pressure-based or a density-based approach. Historically speaking, the pressure-based approach was developed for low-speed incompressible flows, while the density-based approach was mainly used for high-speed compressible flows [38]. Both

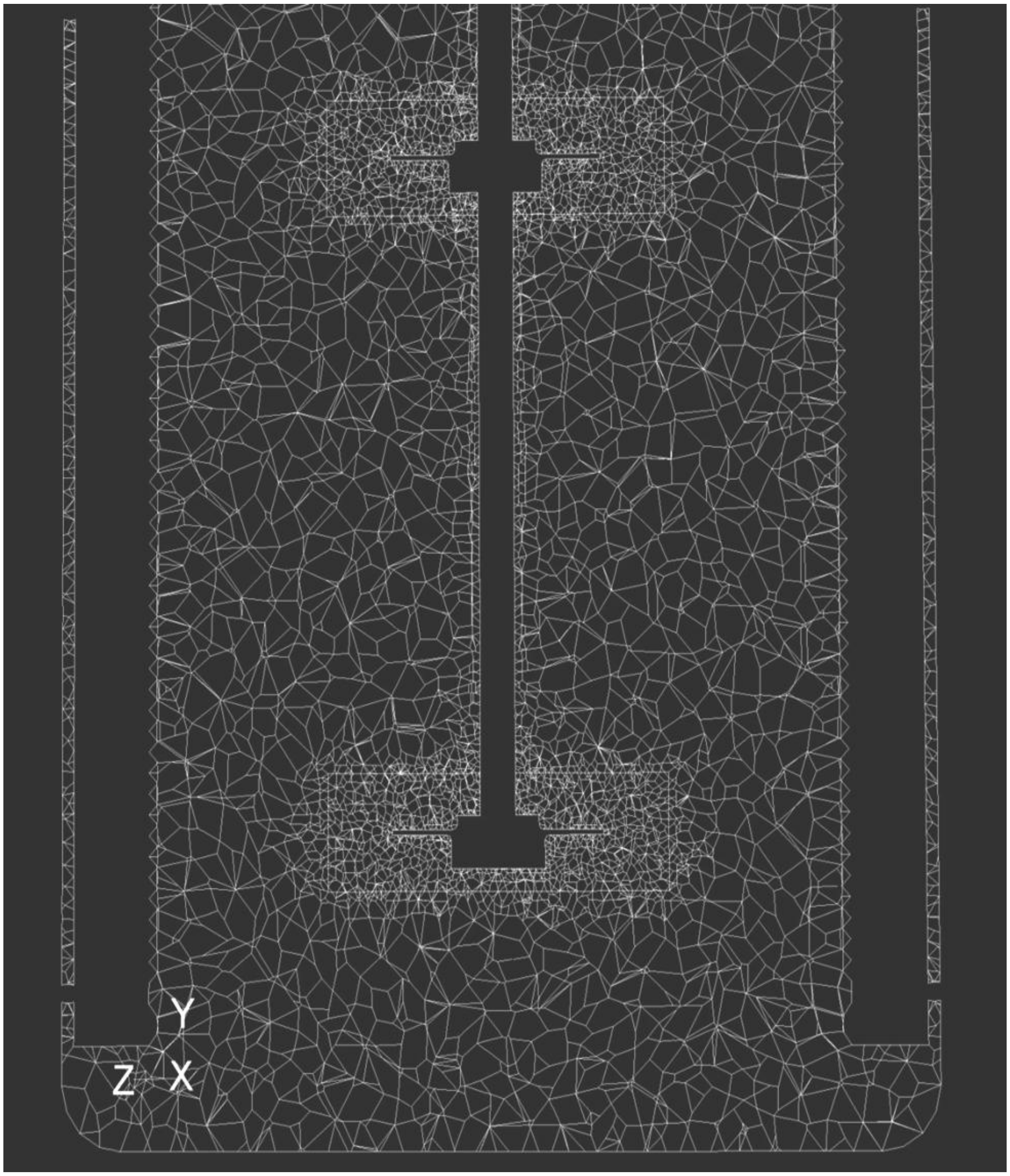

Figure 11: Picture of the polyhedral mesh.

solvers employ a similar discritization process, but different approaches to linearize and solve the discretized equations. Although both solvers have recently been reformulated to accommodate both types of flow, it is more reliable to use the pressure-based solver for incompressible flows, which was used in this study.

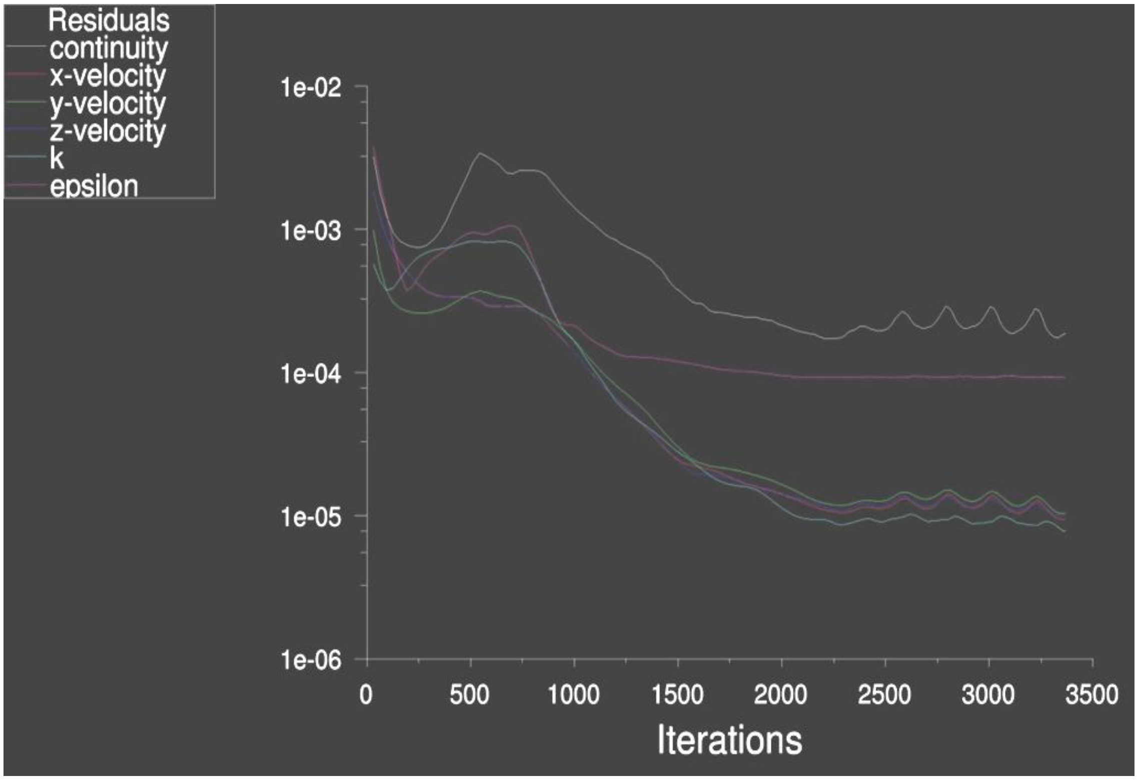

Figure 12: Residuals from the Steady-State A320-A320-Smith configuration.

There are four methods used by FLUENT to couple the velocity and the pressure fields: SIMPLE, SIMPLEC, PISO, and the Coupled Algorithm. SIMPLE and SIMPLEC are generally used for steady-state calculations while PISO and the Coupled Algorithm are used in unsteady (transient) calculations. PISO is generally used with non-uniform or highly skewed grids while the Coupled Algorithm is generally used for uniform grids because of its large memory usage. For this study the steady-state and transient solutions were calculated. Many of the impellers used cause a high skewness to the grid because of the curvature of the impeller blades. Because of this, the SIMPLE solver was used for the steady-state calculation, and the PISO solver was used for the transient.

FLUENT allows the user to choose the discritization scheme for the convection terms of each governing equation. Each term can be solved using the First-Order Upwind, Second-Order Upwind, Quick, or Power Law schemes. The First-Order Upwind scheme is less accurate than the Second-Order, but it can provide more stability in computation. The First-Order Upwind scheme also creates more artificial diffusion than the higher order schemes. The QUICK scheme is second-order accurate, and combines the central differencing scheme and the second-order upwinding scheme. However, when a hexahedral mesh is not used, the QUICK scheme uses second-order upwinding only [38]. Each convection term for this study was evaluated according to Table 3. It should be noted that First-Order upwinding was used for the tracer fluid diffusion. This does create more artificial diffusion than the second-order schemes; however, case studies of stirred tanks have shown to be unstable when second-order schemes are used, as was the case here.

Table 3: Discritization Schemes Used in the Diffusion Terms of the CFD

CONVECTION TERM	DISCRITIZATION SCHEME
Momentum	Second-Order Upwind
Turbulent Kinetic Energy	Second-Order Upwind
Turbulent Dissipation Rate	Second-Order Upwind
Tracer Fluid Diffusion	First-Order Upwind
Transient Formulation	First-Order Upwind

Modeling turbulence is difficult in CFD simulations. There are many different theories on how turbulence is formed and how it dissipates. There are also multiple techniques within each theory to model the turbulence. The turbulence formulations that are applicable to this study are: k-ε, k-ω, k-kl-ω, SST, Reynolds Stress, and Spalart-

Allmaras. The most commonly used models for stirred tank mixers are the *k*-ε, and Reynolds Stress models. The Reynolds Stress model allows multiple inputs for turbulent kinetic energy and turbulence length scale which makes it very precise to each particular case, but it is also very complicated. The Reynolds Stress formulation requires user inputs that are usually only accessible through physical testing of the system. Also it requires much more computation time when calculating the solution, and can become unstable. The *k*-ε model, however, requires less computation and fewer inputs. In the *k*-ε model the turbulent kinetic energy *k*, and its rate of dissipation, ε, are obtained from the following transport equations:

$$\frac{\partial}{\partial t}(\rho k)+\frac{\partial}{\partial x_i}(\rho k u_i)=\frac{\partial}{\partial x_j}\left[(\mu+\frac{\mu_t}{\sigma_k})\frac{\partial k}{\partial x_j}\right]+G_k+G_b-\rho\epsilon-Y_M+S_k \tag{13}$$

$$\frac{\partial}{\partial t}(\rho\epsilon)+\frac{\partial}{\partial x_i}(\rho\epsilon u_i)=\frac{\partial}{\partial x_j}\left[(\mu+\frac{\mu_t}{\sigma_\epsilon})\frac{\partial\epsilon}{\partial x_j}\right]+C_{1\epsilon}\frac{\epsilon}{k}(G_k+C_{3\epsilon}G_b)-C_{2\epsilon}\rho\frac{\epsilon^2}{k}+S_\epsilon \tag{14}$$

In these equations, G_k represents the generation of turbulent kinetic energy due to the mean velocity gradients and G_b represents the generation of turbulent kinetic energy due to buoyancy. As seen in these equations, the turbulence calculations are very complicated and require several user defined constants to model the turbulence correctly. However, it is still much less complicated than the Reynolds Stress model. The constants required for the k-ε formulation have been computed for several stirred tank applications and are widely available in the literature.

In order to decrease computation time and increase the accuracy of the standard *k*-ε model, the realizable *k*-ε model utilizes a new formulation for turbulent viscosity and turbulent dissipation rate. The term ‘realizable’ is used to denote that the model satisfies certain mathematical constraints on the Reynolds stresses, consistent with the physics of turbulent flows [38]. The realizable k-ε model was chosen for this study because it provides superior performance (both in accuracy and computation time) for flows involving rotation (impellers), and more accurately predicts the spreading rate of both planar and round jets (for possibly including an air sparge in future research) [38].

Another important aspect of turbulence is how the computation is integrated to the wall. The near-wall modeling significantly impacts the fidelity of the solution, as walls are the main source of mean vorticity and turbulence [38]. Experiments have shown that the near-wall region can be largely subdivided into three layers: the viscous sublayer, the interim layer and the fully-turbulent layer [38]. The first two layers occur at y^+ values of less than 60, where y^+ is defined by Equation (15).

$$y^+ = \frac{\rho u_t y}{\mu_t} \tag{15}$$

Fluent uses two approaches to modeling this “near-wall” region. The wall function approach bridges the viscosity-affected region between the wall and the fully-turbulent region. The near-wall approach enables the viscosity-affected region to be resolved with a mesh all the way to the wall. The approach used in this study is a hybrid of these two models called “Enhanced Wall Treatment”. The enhanced wall treatment is a near-wall modeling method that combines a two-layer model with enhanced wall functions. As such, the enhanced wall treatment can be used with coarse meshes, as well as fine meshes [38]. Pictures of the y^+ values are shown in Figure 13 and Figure 14.

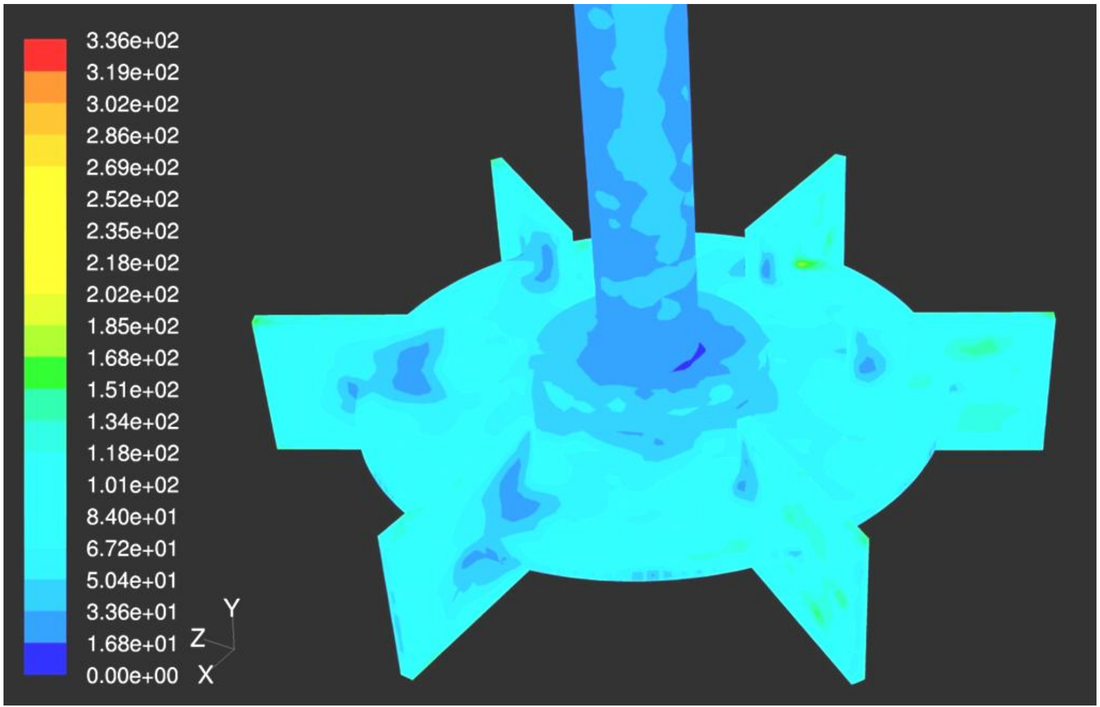

Figure 13: Graphical representation of y^+ values around a Rushton impeller.

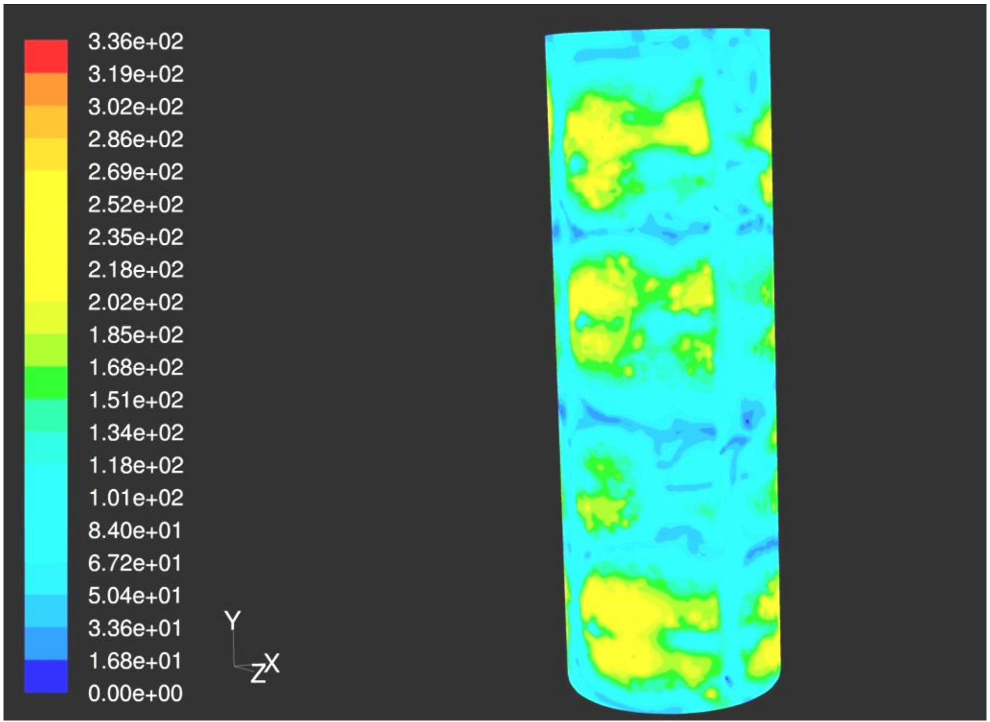

Figure 14: Graphical representation of y^+ values around the walls of the stirred tank.

To have a moving boundary in a CFD calculation FLUENT uses two types of meshes to simulate movement: the “Rotating Reference Frame” and the “Moving Mesh” formulations. The rotating reference frame model uses a section of the fluid that is rotating to simulate the impeller moving through the fluid. Instead of the impeller actually moving, there is a small volume of fluid located just around the impeller labeled as a moving reference frame (MRF). When the fluid within the MRF comes in contact with a surface it acts as if it were moving, while the other nodes within the MRF do not. The fluid velocities within that rotating reference frame are continually transformed according to the impact of the impeller and a solution is converged upon. The moving mesh technique is a little more complicated. It uses the FLUENT solver to move boundaries and/or objects and to adjust the mesh accordingly [38]. This does seem to give more accurate results in certain cases; however, the computation time is exponentially increased, and the solver becomes unstable when using this method. For this project the rotating reference frame was chosen for two reasons. First, it is generally accepted as accurate by those who do research in the fermentor/stirred-tank mixing community [24, 25, 26, 27, 39]. Secondly, it has saved possibly hundreds of hours of computation time.

CFD Results Obtained

For each tank configuration presented in section 4.1, two outputs were calculated. First, the steady-state flow field was calculated and visually displayed to identify “dead zones” where the fluid was not moving or mixing very well. These pictures of the flow field gave information on how each impeller moves fluid through the tank. This aided in determining the effectiveness of different impellers in their mixing capability.

The second output from the CFD is a mixing time for each configuration. After the steady-state formulation was calculated, the simulation was changed to a transient formation and a tracer fluid was introduced into the tank. The volume fraction of tracer fluid was monitored at several locations in the tank, according to Figure 15, and the mixing time was calculated as the time when 90% of homogeneity was reached. A contour plot of mass fraction of tracer fluid is shown at the mixing time of the four-Rushton configuration in Figure 16. These mixing times were compared with the experimental k_La data to explore the possibility of a correlation between the two. Several configurations of tanks were then modeled that were not experimentally tested in order to give a more complete test matrix of tank configurations.

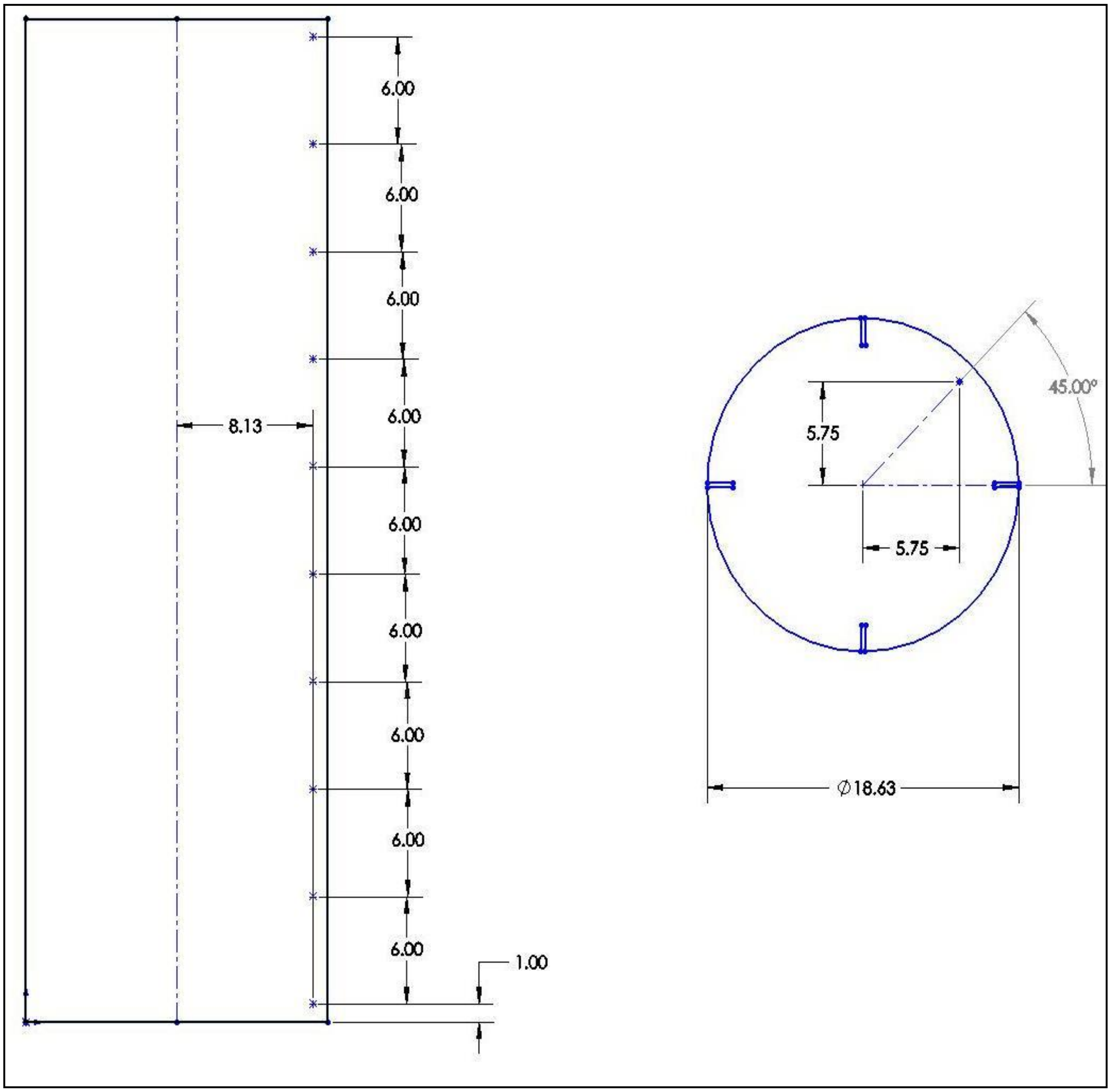

Figure 15: Schematic of tracer fluid probe locations used in the numerical mixing time studies.

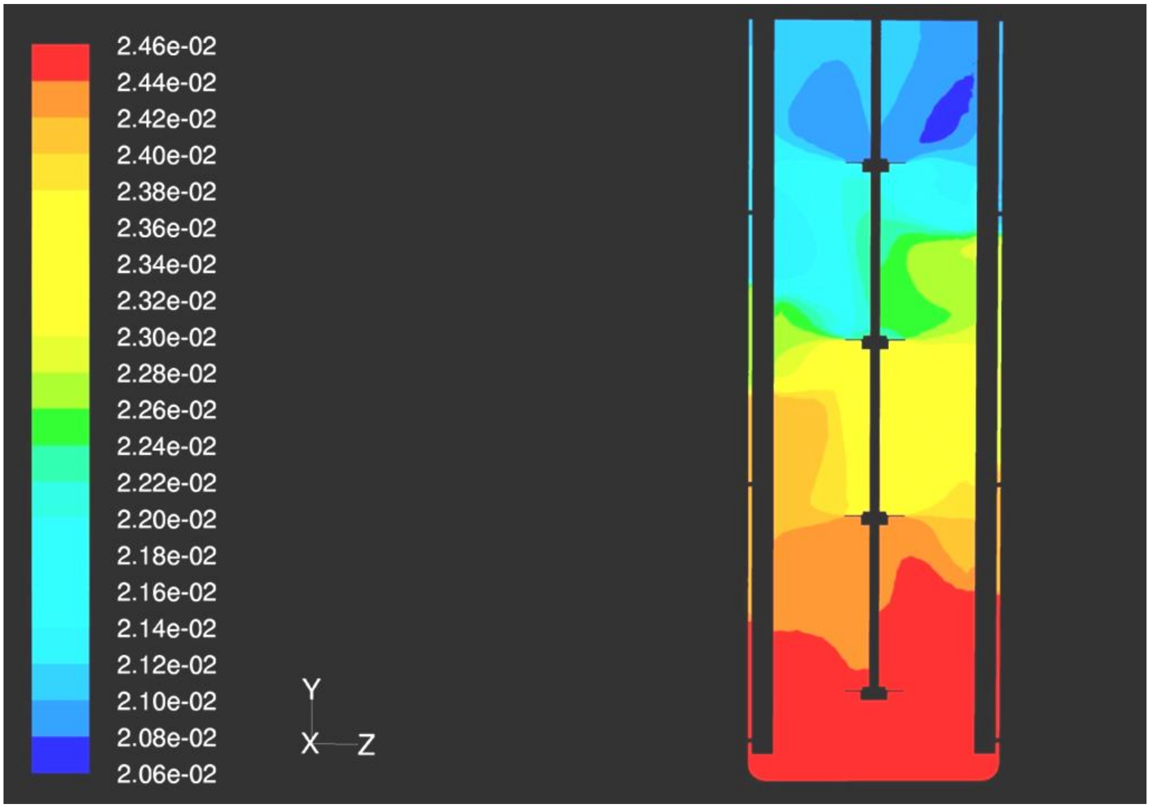

Figure 16: Contour plot of the mass fraction of tracer fluid for the four-Rushton impeller configuration.

Correction for Probe Response Time

An accurate probe response time correction must account for all time constants in the probe. A typical galvanic dissolved oxygen probe consists of a gas-permeable membrane and an electrolyte fluid that leads to an anode and cathode, which measure the resistance in the electrolyte fluid. Two time constants should be used to represent both the time required for the oxygen to dissolve through the gas-permeable membrane, and to dissolve through the electrolyte fluid. Although the first-order correction approach is widely used [12, 35, 39, 40] for probe time response correction, it does not account for both time constants. A correction model which includes both time constants is needed for accurate k_La determination.

In order to correct for a slow probe response time, a dissolved oxygen probe system can be compared to a spring, mass, damper system. Newton's second law can be used to describe a single degree of freedom spring mass damper system as follows:

$$\frac{1}{g_c}\left[m\left(\frac{d^2s}{dt^2}\right)\right]+\zeta_d\left(\frac{ds}{dt}\right)+ks=F(t) \qquad (16)$$

Even though a dissolved oxygen probe does not look or work the same as a spring-mass-damper system, the responses of the two systems are identical [24]. Equation (16) can be further simplified by using a time constant, τ. The time constant represents the displacement (s) through a medium. The equation for the time constant is given below:

$$\tau = 2m/\zeta_d g_c \qquad (17)$$

This comparison to a spring, mass, damper system will be referred to throughout the rest of this paper as the second-order model.

The second-order model described can be applied to systems containing two time constants. Beckwith et al. [24] apply Equations (16) and (17) to a temperature probe with two time constants. The temperature probe, in this case, has a jacket around it. The two time constants represent the time it takes the temperature to diffuse through the jacket and through the probe. The two time constants for a typical galvanic dissolved oxygen sensor could represent the time required for the oxygen to dissolve through the gas-permeable membrane and through the electrolyte fluid. Applying the equation given by Beckwith to a dissolved oxygen probe yields the equation given below:

$$\tau_1\tau_2\frac{d^2C_m}{dt^2}+(\tau_1+\tau_2)\frac{dC_m}{dt}+C_m=C \tag{18}$$

Notice that if either of the time constants were zero, the equation would revert to a first-order time response model. Because the second-order model for probe time response, as presented in Equation (18), accounts for both sources of lag time, it is theoretically more accurate than the traditional first-order model.

To use the second-order model for probe response correction, the two time constants must be determined. An artificial step function in dissolved oxygen can be created to determine the time constants in Equation (18). To achieve this, the response of the dissolved oxygen probes can be fit to the general solution for a step response.

$$\frac{C_L-C_m}{C_L-C_o}=\left(\frac{\zeta}{\zeta-1}\right)e^{-t/\zeta\tau_2}-\left(\frac{1}{\zeta-1}\right)e^{-t/\tau_2} \tag{19}$$

It should be noted that this general solution is for a step response; if the dissolved oxygen of the surrounding medium is changing, this solution becomes invalid and one must revert to Equation (18) where C_L is the forcing function. The use of a step function leads to the determination of the two time constants needed to correct for probe response time.

Once the time constants are known, the derivatives from Equation (18) must be determined. For the case of fermentors, the forcing function is not known and the solution must be computed by approximating the differentials in Equation (18). Numerical approximations of the derivatives can be used, as outlined by Chapra and Canale [25].

$$f'(x_i)=\frac{f(x_{i+1})-f(x_{i-1})}{2h} \tag{20}$$

$$f''(x_i) = \frac{f(x_{i+1}) - 2f(x_i) + f(x_{i-1})}{h^2} \tag{21}$$

Before data correction can be applied to dissolved oxygen data, the time constants for the probe must be determined. To accomplish this, the probes were subjected to a dissolved oxygen step response. Each probe was allowed to reach equilibrium in a beaker containing water with 0% oxygen-saturation. Next the probe was immediately transferred to a beaker containing water with 100% oxygen-saturation. The measured values of the probe, which represent the probe's response to the oxygen step function, were recorded electronically. This was repeated several times for each probe. Each recorded data set was fit to the general solution for a step response shown in Equation (19). This was accomplished by writing a program that used a guess-and-check sub-routine to find the values of the time constants. The time constants of all the probes were then averaged to give approximate time constants for all the probes. For the second-order model, the time constants are 1.582 and 23.748 seconds for τ_1 and τ_2, respectively. These newly acquired time constants can be used for probe response correction.

To examine the validity of the second-order probe response correction method, the two time constant correction model was applied to data from the oxygen step function. Examining the corrected response and how closely it mimics a step response shows the effectiveness of the correction. The low error produced by this process validates the use of such correction methods on oxygen mass transfer data.

Since the use of a second-order model was now validated, the effective range of the model was determined. To accomplish this, three separate oxygen mass transfer scenarios were examined. Based on the findings of Phillichi and Stenstrom [20], it was expected that the error in k_La estimation would increase as the value of true k_La increased. Three separate oxygen mass transfer scenarios were examined where low, medium, and high oxygen mass transfer coefficients were expected. These differences in k_La were expected based on differences in mixing speed and gas flow rate. The low, medium, and high tests were performed according to Table 4. The oxygen mass transfer testing was performed with the experimental setup described in section 4.1 of this thesis.

Correction for Transient Volume Rise

To explain the volume rise in an STR an analytical approach was used to identify how the bubbles act throughout the tank, and how those bubbles affect the dissolved oxygen measurement. The derivation also shows how to correct for dissolved oxygen data obtained during a test where a transient volume rise occurs. This analytical derivation and the ensuing correction are found in the results section of this report.

Dimensionless Correlations

In their paper on gas/liquid mass transfer in stirred vessels, Schlüter and Deckwer

Table 4: Impeller Speeds and Gas Flow Rates Used for the Low, Medium, and High k_La Values for Testing

Range of k_La expected	Impeller Speed (rpm)	Gas Flow Rate (lpm)
Low	250	140
Medium	300	170
High	450	170

[26] propose that k_La is not dependent upon geometric constraints, but rather on specific power input and gas flow rate. As a nondimensional approach to solving for k_La they propose the following equation:

$$k_L a \left(\frac{\nu}{g^2}\right)^{1/3} = C \left[\frac{P/V}{\rho(\nu g^4)^{1/3}}\right]^a \left[\frac{q}{V}\left(\frac{\nu}{g^2}\right)^{1/3}\right]^b \tag{22}$$

The constants C, a, and b in Equation (22) are solved for different tank geometries. Schlüter and Deckwer determine these constants for two tank configurations. One tank is agitated with 3 Rushton impellers, while the other is agitated with 4 Intermig impellers [26]. The results are tabulated in table Table 5.

Schlüter and Deckwer report that these numbers are for a stirred vessel with a height to diameter ratio of 2:1, a power range of $0.5 \leq P/V \leq 16$ kW/m^3 and a flow rate range of $0.0038 \leq q/V \leq 0.027$ s^{-1}[26]. They do not, however, report on how changing the geometry of the tank affects the constants of Equation (22). Even though the constants for this equation have not been determined for all tank or impeller types, this is the most recently published dimensionless correlation for stirred tank fermentors.

Nishikawa et al. [27] report that a similar correlation can be derived using the geometries of the tank and impellers, the physical properties of the liquid and the power input according to the following equation:

$$\frac{k_L a \cdot d_t}{D_L} = 0.368\left(\frac{\rho N {d_i}^2}{\mu}\right)^{1.38}\left(\frac{\mu}{\rho D_L}\right)^{0.5}\left(\frac{\mu V_s}{\sigma}\right)^{0.5}\left(\frac{N^2 d_i}{g}\right)^{0.367}\left(\frac{N d_i}{V_s}\right)^{0.167}\left(\frac{d_i}{d_t}\right)^{0.25}\left(\frac{P}{\rho N^3 {d_i}^5}\right)^{0.75} \tag{23}$$

Nishikawa however, does not report over which ranges of impeller speeds and gas flow rates this equation is valid. Equation (23), unlike Equation (22), does allow

Table 5: Constants Used for Equation (22)

	C	a	b
3-Rushton	7.94×10^{-4}	0.62	0.23
4-Intermig	5.89×10^{-4}	0.62	0.19

compensation for different geometries and thus has the possibility of not having to use different coefficients for different tank and impeller geometries.

The experimental data found earlier in this study was correlated to Equations (22) and (23) to determine how accurately the Schluter and Nishikawa correlations predict k_La. To determine the power delivered to the fluid for each of these equations the commonly used power number equation was used.

$$P = N_P n \rho N^3 {d_i}^5 \tag{24}$$

In this equation N_P is the empirically obtained power number for the impellers as proposed by Post and by Vasconselos et al. [28, 29]. Since there are several varying methods for determining the gassed power and Equation (24) is commonly used, the un-gassed power consumption was used for this study. Power delivered to the fluid and air sparged into the tank was varied to explore how each of these parameters affects the mass transfer capability of the tank. Power delivered to the fluid for this study ranged from 6.6W to 253.2W, and air sparged into the tank ranged from 2.33 m^3/s to 3.33 m^3/s.

New correlations were developed by fitting the experimental results of k_La measurement, as outlined in Table 1, to the Schluter and Nishikawa equations and changing the equations' coefficients. The coefficient values which produced the least error when compared to the actual experimental data were selected for use in the new correlation.

CHAPTER 6

RESULTS AND DISCUSSION

Probe Response Correction

Before a correction can be applied to dissolved oxygen data, the time constants for the probe must be determined. To accomplish this, the probes were subjected to a dissolved oxygen step response. Each probe was allowed to reach equilibrium in a beaker containing water with 0% oxygen-saturation. Next the probe was immediately transferred to a beaker containing water with 100% oxygen-saturation. The measured values of the probe, which represent the probe's response to the oxygen step function, were recorded electronically. This was repeated several times for each probe. Each recorded data set was fit to the general solution for a step response shown in Equation (19). This was accomplished by writing a program that used a guess-and-check sub-routine to find the values of the time constants. The time constants of all the probes were then averaged to give an approximation of the time constants. For the second-order model, the time constants are 1.582 and 23.748 seconds for τ_1 and τ_2, respectively. These time constants can be used for probe response correction.

To examine the validity of the second-order probe response correction method, the two time constant correction model was applied to data from the oxygen step function. Examining the corrected response and how closely it mimics a step response shows the effectiveness of the correction. The results of applying the step function to the probes with the ensuing correction are shown in Figure 17. The average error between the step function and the corrected step response was found to be 4.05%. As shown in the figure, the measured values slowly rise to saturation due to the time response of the probe. The corrected values, however, rise suddenly at the beginning of the experiment and are maintained at saturation. This sudden rise, which closely matches the step response, suggests that the second-order time response model used to correct the data is satisfactory. The small "bumps" in the corrected values between the 50 and 60 second marks are most likely due to minute errors in the experimental data that are exaggerated when performing the numerical differentiations.

Since the use of a second-order model was now validated, the effective range of the model was determined. To accomplish this, three separate oxygen mass transfer scenarios were examined. Based on the findings of Phillichi and Stenstrom [20], it was expected that the error in k_La estimation would increase as the value of true k_La

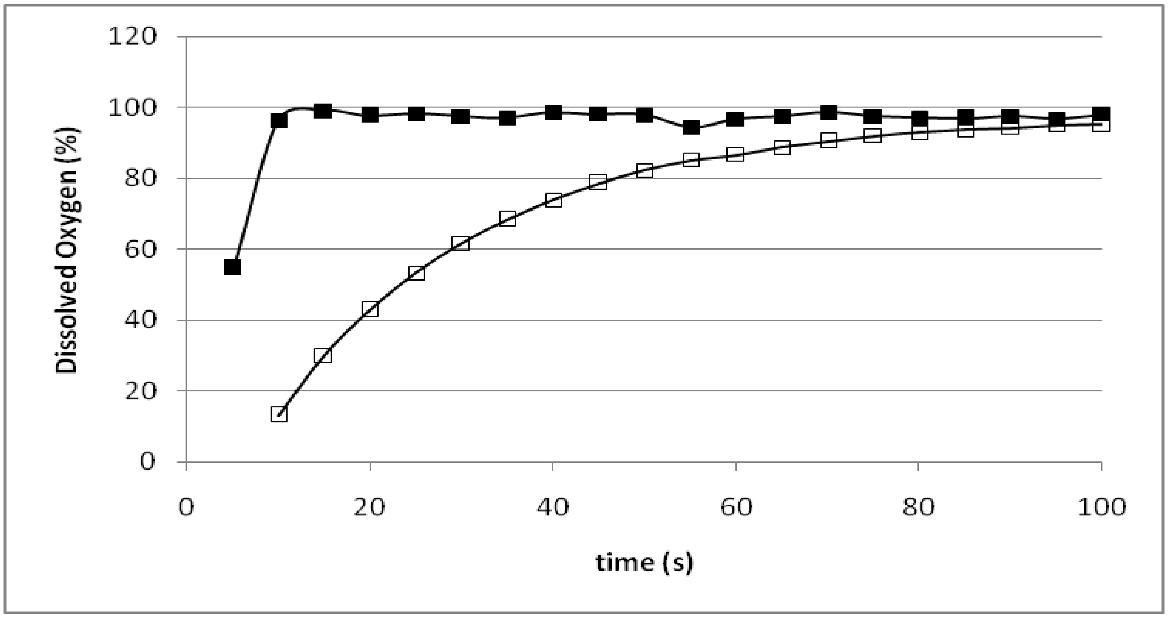

Figure 17: Graph of dissolved oxygen probe response to a step function. The hollow and solid squares represent the measured and corrected values, respectively.

increased. Three separate oxygen mass transfer scenarios were examined where low, medium, and high oxygen mass transfer coefficients were expected. These differences in k_La were expected based on differences in mixing speed and gas flow rate. The low, medium, and high mass transfer rates were performed according to Table 4.

The second-order time response model was used to correct data obtained from the three kLa tests shown in Table 4. The results, shown in Figure 18, indicate that the corrected curves reach saturation much faster than the measured curves. This observation suggests that oxygen mass transfer rates calculated from raw dissolved oxygen measurements are under-estimating the true oxygen mass transfer potential of the system. This assumption was confirmed by calculating the overall oxygen mass transfer coefficient, or kLa, for each curve. These values, as presented in Table 6, also suggest that the percent increase of oxygen mass transfer due to probe response time correction is dependent on the oxygen mass transfer rate itself. That is, the effect of the correction factor on kLa increases as kLa itself increases.

Table 6: k_La Values for Three Different Scenarios That Were Calculated Using Measured and Corrected Data Points

	Low	Medium	High
Measured	93.6	115.2	176.4
Second-Order	234	306	651.6
Difference	150%	165.6%	269.4%

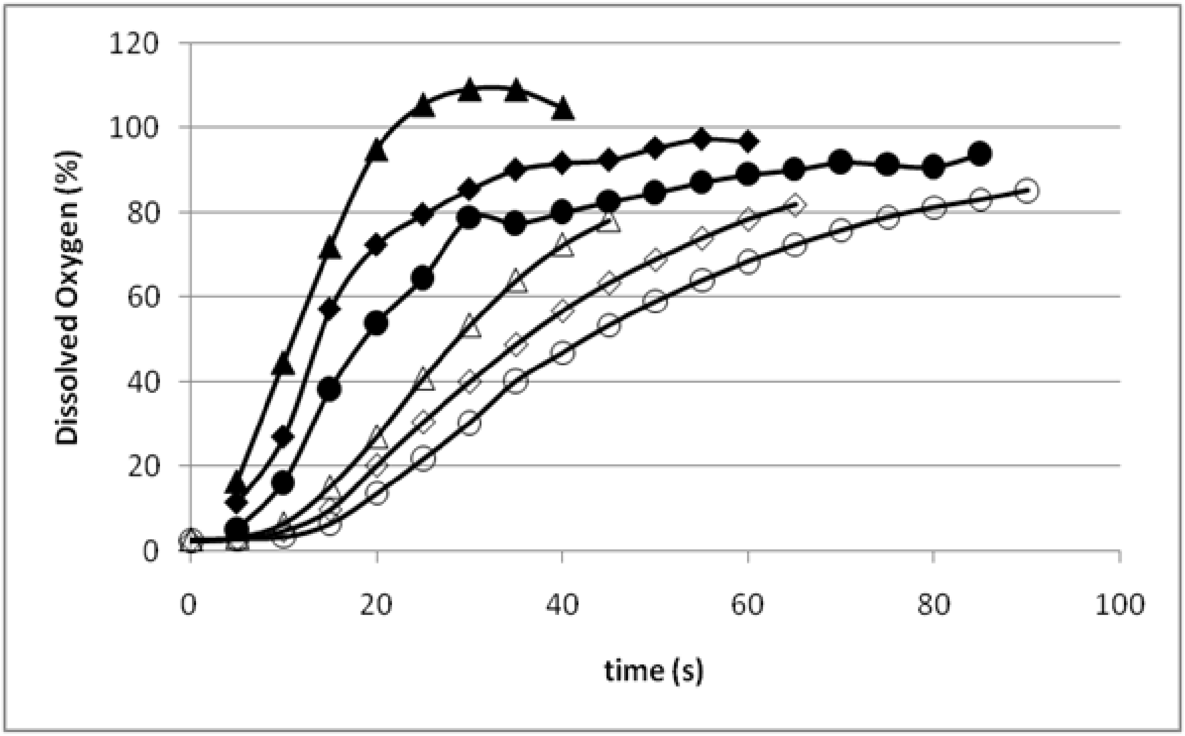

Figure 18: Graph of dissolved oxygen response during three separate oxygen transfer rate determination tests. The graph shows measured and corrected values, represented by hollow and solid markers, respectively. The low, medium, and high tests are represented by circle, diamond, and triangle markers, respectively.

Transient Volume Rise Correction

To explain the volume rise in the reactor two possible models are presented in this study. The first model assumes that the bubbles move as a front up through the tank. The second model assumes that the bubbles are evenly dispersed throughout the tank and the bubble density increases until a steady state is reached at time t_0. These two models are illustrated in Figure 19 and Figure 20, respectively.

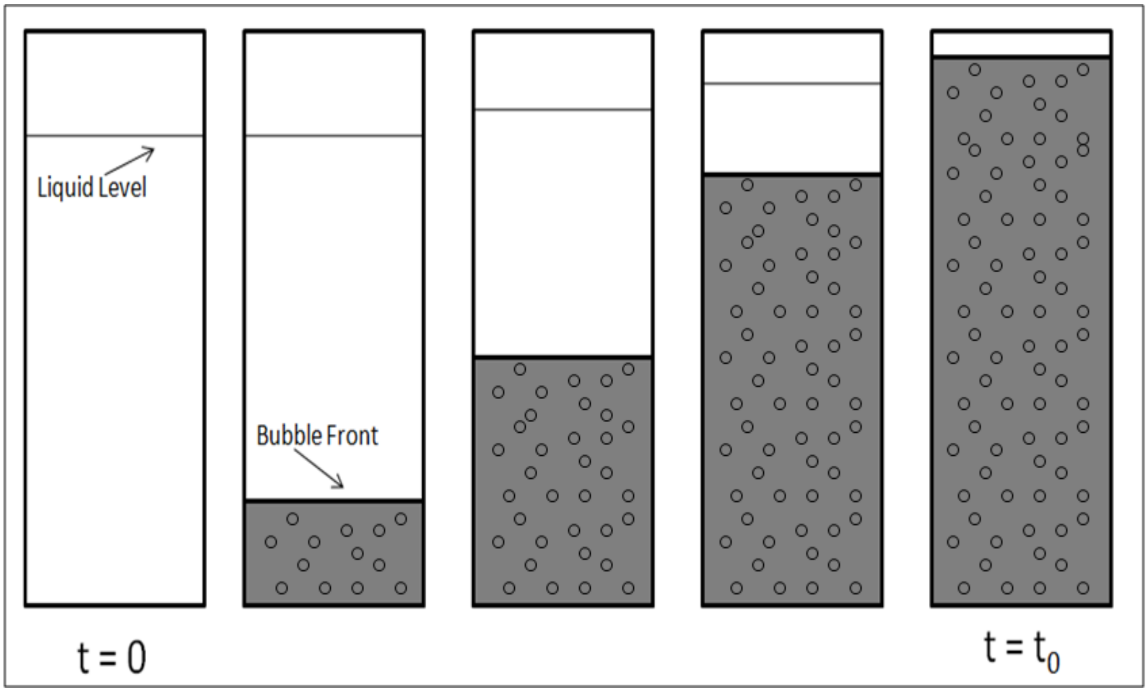

Figure 19: A transient volume rise model in which bubbles travel as a front through the tank until steady-state is reached.

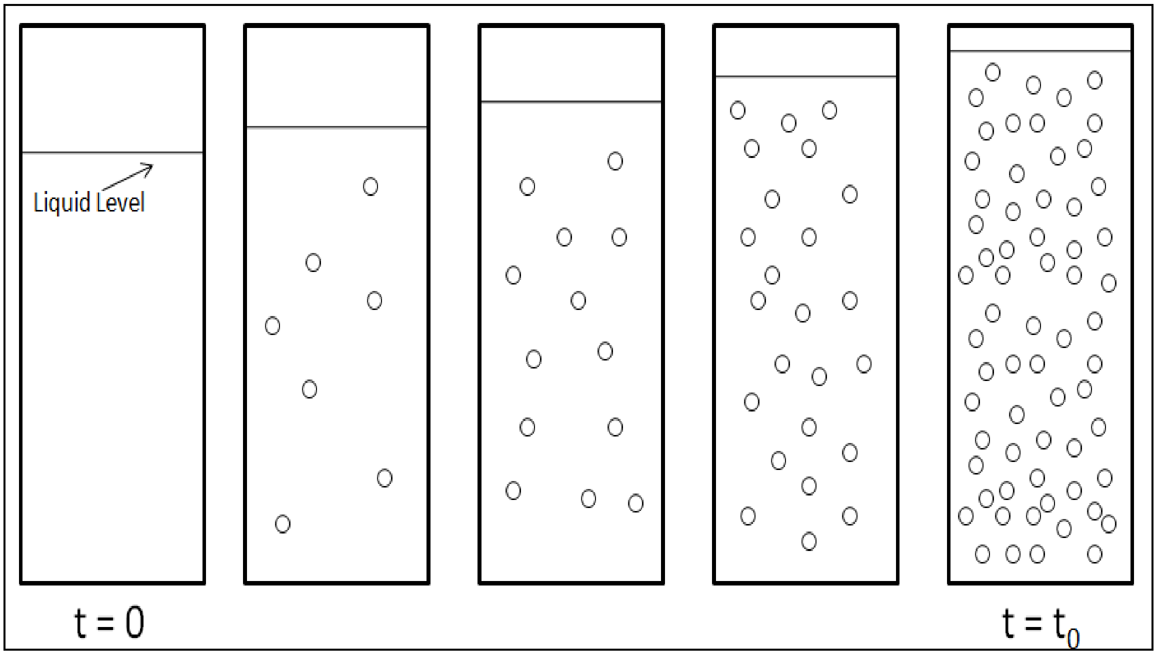

Figure 20: A transient volume rise model in which bubbles are evenly distributed throughout the tank and increase in density until steady-state is reached.

In order to accurately describe these conditions the governing equation for mass transfer was used and analytically solved for each of the transient cases.

$$V(t)\frac{dC}{dt} = h_m * A(t) * [C^* - C(t)] \tag{25}$$

Equation (25) is similar to Equation (10), except that volume and surface area terms are considered unsteady-state values that change with time. The investigation of the two possible transient volume models will increase our understanding of their effect on dissolved oxygen measurement.

The study of the two scenarios gave an understanding of what is taking place in the actual test tank. The resulting analysis of the analytical derivations showed that one equation can be used to model both scenarios. It also revealed a manner in which corrections could be made to existing k_La data.

The first scenario, presented in Figure 19, allows us to assume that the bubbles travel as a front through the tank. Following this assumption, *V(t)* in Equation (25) is the volume of liquid that contains bubbles, *A(t)* is the total surface area of all the bubbles, and h_m is the mass convection coefficient. A volumetric mass convection coefficient can then be defined as:

$$k_L = \frac{h_m}{V(t)} \tag{26}$$

Next, α and β are introduced to describe the volume and surface area increase.

$$V(t) = \alpha * t \qquad t < t_0 \tag{27}$$

$$V(t) = V_0 \qquad t > t_0 \tag{28}$$

$$A(t) = \beta * t \qquad t < t_0 \tag{29}$$

$$A(t) = A_0 \qquad t > t_0 \tag{30}$$

Making these substitutions into Equation (25) gives the following result:

$$\alpha t \frac{dC}{dt} = h_m \beta t [C^* - C(t)] \tag{31}$$

After separating variables and integrating,

$$-\ln(C^* - C) = \frac{h_m \beta}{\alpha} t + C_1 \tag{32}$$

When the initial conditions are applied (at t = 0, C = 0),

$$\frac{C}{C^*} = 1 - e^{-\frac{h_m \beta}{\alpha} t} \tag{33}$$

However, Equation (33) only applies when $t < t_0$. When $t > t_0$ the following equation applies.

$$\frac{C}{C^*} = 1 - e^{-\frac{h_m A_0 t_0}{V_0}\left(\frac{t}{t_0} - 1 + \frac{\beta V_0}{\alpha A_0}\right)} \tag{34}$$

In Equation (34) A_0 is the surface area of all the bubbles in the tank at steady-state and V_0 is the volume of the tank at $t = t_0$. Equation (33), which describes the first model, is valid before steady-state occurs and will be compared to a similar equation for the second model.

The second model assumes that the bubbles are spread evenly throughout the tank. As time progresses, the bubbles gradually become denser until the amount of air leaving the tank equals the amount of air entering the tank. The assumption in this model indicates that the volume change is negligible and thus V_0 is used instead of $V(t)$. The same derivation procedure as in the first model was used to develop Equations (35) and (36).

$$\frac{C}{C^*} = 1 - e^{-\frac{h_m \beta}{V_0} t^2} \qquad t < t_0 \tag{35}$$

$$\frac{C}{C^*} = 1 - e^{-\frac{h_m A_0}{V_0} t} \qquad t > t_0 \tag{36}$$

Note that Equation (35) is the same as Equation (33) if you make a substitution for α according to Equation (27).

To analyze the two transient models, they must be compared to the steady-state model. The steady-state model represents the hypothetical response if there were no transient volume rise. This solution is given by the following:

$$\frac{C}{C^*} = 1 - e^{-\frac{h_m A_0}{V_0} t} \tag{37}$$

To study the effect of transient volume rise on k_La measurement, Equations (33) and (35) were compared to Equation (37). This was done by graphing Equation (37) (Steady-State DO concentration) against Equations (33) and (35) (Transient DO concentration) for several values of α and β. The plots were used to study the effects of changing α and β. These plots were then used to calculate the expected k_La for both scenarios (steady-state and transient). Upon inspection of the plots created, it was decided that the effect the transient period had on k_La calculation was not due to changes in α or β. The effect, rather, was based on how many data points used to calculate k_La fell within the transient period ($0 < t < t_0$). The plots were compared for differing values of α and β to show a lack of correlation between these variables and the effect on k_La

computation. Regression curves were computed to explain how the k_La calculation was affected.

To model the data the geometry of the reactor described in section 4.1 was assumed. The transient increase was assumed to be between 18 and 45 liters rise in volume over a period of 8 to 10 seconds, which was observed during k_La testing. The average bubble size was assumed to be between 1 and 5 mm. Using these numbers α is assumed to have a range of: $0.29 < \alpha < 0.42$ while β is assumed to have a range of: $1.0 < \beta < 1900$. For constant β, α showed a 40% increase in calculated k_La over the range: $0.29 < \alpha < 0.42$. For constant α however, β showed an 1800% increase in k_La over the range: $100 < \beta < 1900$. This shows that for a constant volume of air, if the bubble size becomes smaller (i.e. more surface area) the k_La will increase dramatically. However, an increase in air volume will not cause so great a change in k_La.

The models generated from differing α and β indicate that the increase in k_La measured from the transient data is dependent on how many data points fall within the transient time period. This is shown in Figure 21, where the following definitions are used:

$$P_k = \frac{k_La_t - k_La_{ss}}{k_La_{ss}} \tag{38}$$

$$P_{dp} = \frac{\#\text{ of data points within } t_{trans}}{\#\text{ of data points used for linear interpolation}} \tag{39}$$

In these equations k_La_t is the k_La measured from the transient model and k_La_{ss} is the k_La measured from the steady-state model. Equation (40) is the polynomial fit to the curve shown in Figure 21.

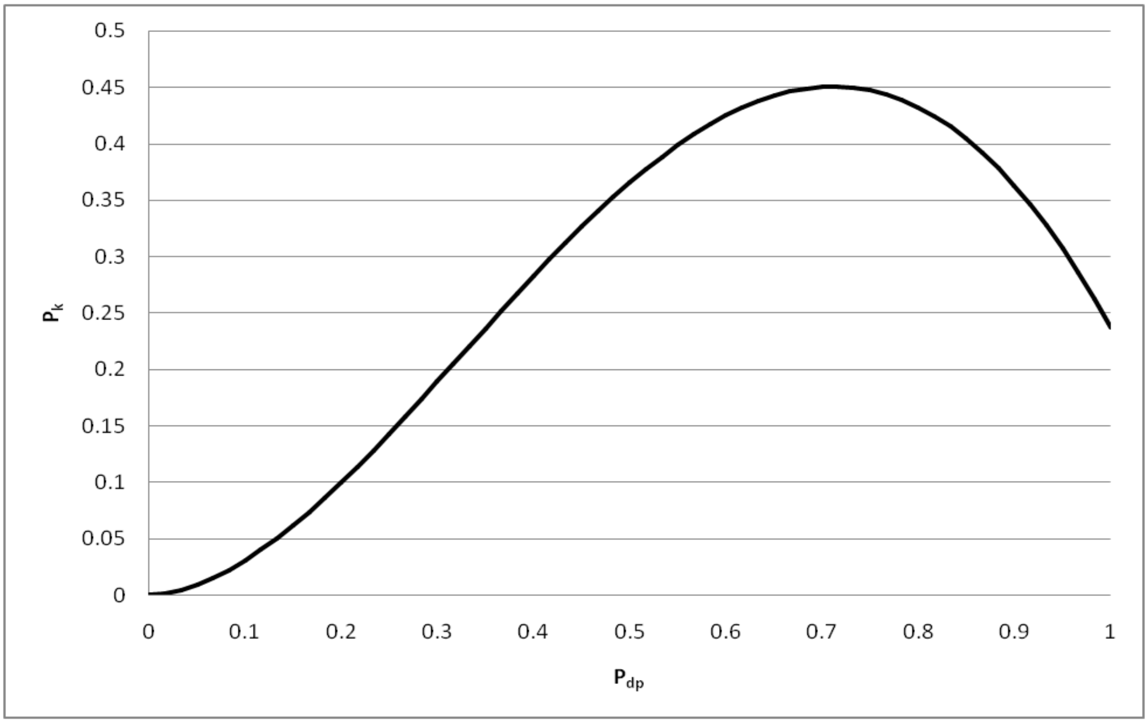

Figure 21: Increase of k_La versus number of data points used in linear interpolation.

$$P_k = .7502P_{dp}^{\ 4} - 3.4760P_{dp}^{\ 3} + 2.9137P_{dp}^{\ 2} + .0495P_{dp} \tag{40}$$

The peak in this curve is caused by an interesting phenomenon. The slope of the linearized points changes as more and more erroneous points are used in the linearization. However, as the number of points gets larger, the slope of the linearized points gets closer and closer to the slope of that of a line with no erroneous points. This is shown in Figure 22.

When using the unsteady-state method, calculating k_La becomes more accurate when more data points are used in the line fit. By assuming the data is continuous and ranges from 0% to 95% oxygen saturation, a correlation can be made to show how k_La is affected by this transient period. A new variable, t_{95}, is defined as the time required to reach 95% oxygen saturation.

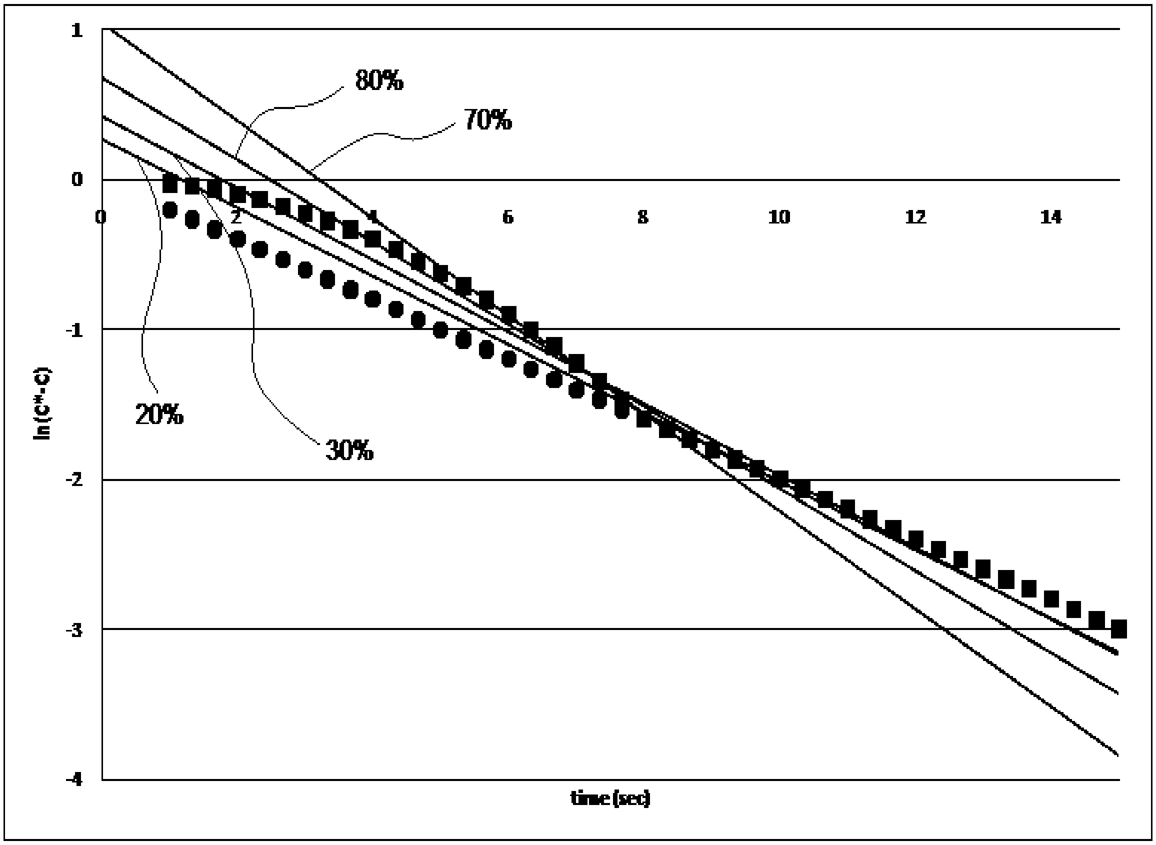

Figure 22: Graph of simulated data points for a $k_L a$ test. The square points represent data from a test with an 8-second transient period. The circles represent data from a test with no transient period. The solid lines show line fits using 20%, 30%, 70%, and 80% of the transient points in the line fit.

The mass transfer coefficient can be substituted into Equation (37) to yield the following:

$$\frac{C}{C^*} = 1 - e^{-k_L a t} \tag{41}$$

The final conditions, t=t_{95} and $\frac{C}{C^*} = .95$, can be applied to get Equation (42).

$$t_{95} = \frac{-\ln(.05)}{k_L a} \tag{42}$$

Substituting Equation (42) into Equation (39) gives an equation for the percent of time contained within the transient period.

$$P_{dp} = \frac{t_{trans}}{t_{95}} = \frac{t_{trans}\, k_L a}{-\ln(.05)} \tag{43}$$

In this equation t_{trans} is the time of the transient period. As shown from Equation (43) the time of the transition period can have a great affect on how much the data varies from the steady-state model.

As shown in Figure 23 the true value of k_La and how many data points are used to make that calculation predict the percent error. The error in calculated k_La can range from 0% to 43% if a transient volume increase is involved. The transient volume rise correction is applicable to any k_La measurement technique that involves a volume rise during data collection due to increased suspended gas bubbles.

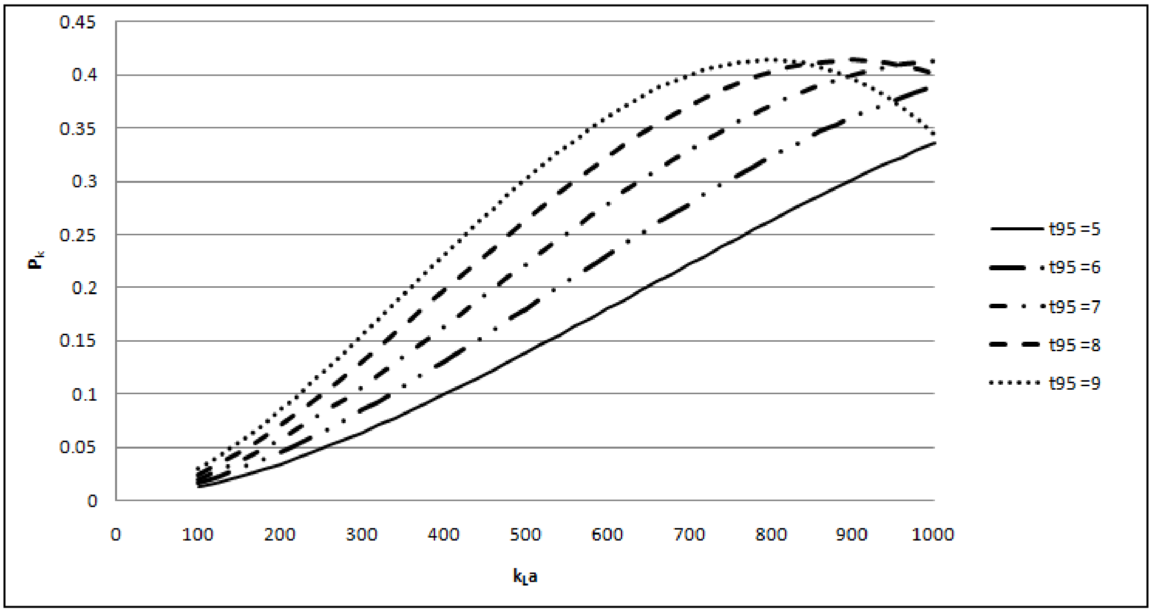

Figure 23: Percent increase versus actual k_La for different values of k_La and t_{95}.

Experimental Testing of k_La and How it Correlates to Mixing Time

The experimental testing, outlined in Table 1 and Table 2, was performed at two air flow rates: 140 and 170 liters per minute. Each test gave an average k_La value for the tank and several of the tests were repeated to give more accurate results. The results obtained from this testing, along with the standard deviations and number of tests performed, are outlined in Table 7. The standard deviation was calculated as the standard deviation found between the repeated tests performed.

Table 7: Average k_La Values with Standard Deviations and Number of Tests Performed

Impeller Configuration	Impeller Size (in)	Baffle Type	Number of Tests Performed	k_La			
				140 lpm	St. Dev.	170 lpm	St. Dev.
He3	6.0	flat	1	239	--	329	--
He3	6.0						
Rushton	6.0						
He3	6.0	flat	1	368	--	430	--
He3	6.0						
Smith	6.25						
A320	6.0	flat	1	285	--	354	--
A320	6.0						
Rushton	6.0						
A320	6.0	flat	1	511	--	367	--
A320	6.0						
Smith	6.25						
Rushton	6.0	flat	3	362	44.2	415	63.2
Rushton	6.0						
Rushton	6.0						
Rushton	6.0						
Rushton	6.0	film	6	608	127	786	87.0
Rushton	6.0						
Rushton	6.0						
Rushton	6.0						

From this data it is hard to tell which of the different geometries creates better conditions for mass transfer. The A320-A320-Smith configuration, for example, gives a very good k_La of 511 at the lower gas flow rate, but a rather average k_La of 367 for the higher gas flow rate. Comparing the three-impeller configurations that use the same radial flow impeller gives us better understanding of the difference between the A320 and He3 impellers. At the lower air flow rate the A320-A320-Rushton and He3-He3-Rushton configurations give k_La values of 285 and 239, respectively. At the higher gas flow rate they give values of 354 and 329, respectively. Since these values do not show significant differences from each other, we can assume that neither the He3 nor the A320 impeller has an advantage over the other one. When we compare the A320-A320-Smith and He3-He3-Smith configurations we notice that one performs better at the lower gas flow rate and one performs better at the higher gas flow rate. This gives us no insight into whether or not there is a significant difference in performance between the A320 and He3 impellers. The configuration that does give a significant difference at both air flow rates is the four-Rushton configuration with film-covered baffles.

To gain more insight on these and other configurations numerical studies were used to calculate mixing times. The mixing times are outlined in Table 8 and Table 9.

Some research shows a correlation between mixing time and mass transfer in STRs. Yu et al. [28] show that 3D numerical models can predict mixing times that directly correlate to the mass transfer coefficient in mammalian cell cultures. However, these studies only correlate different mixing speeds and gas flow rates for one specific tank. They do not include different types of impellers, baffles, or tank sizes. In addition,

Table 8: Mixing Times for the Three-Impeller Configurations

Impeller Configuration	Impeller Diameter (in)	Baffle Type	Mixing Time (sec)
He3 He3 Rushton	6.0 6.0 6.0	Flat	16.0
He3 He3 Smith	6.0 6.0 6.25	Flat	15.8
He3 He3 Smith	6.0 6.0 6.25	1.5” Semi-Circle	18.3
A320 A320 Rushton	6.0 6.0 6.0	Flat	11.2
A320 A320 Smith	6.0 6.0 6.25	Flat	10.5
Rushton Rushton Rushton	6.0 6.0 6.0	Flat	7.9
Rushton Rushton Rushton	6.0 6.0 6.0	1.5” Semi-Circle	5.5
Rushton Rushton Rushton	6.0 6.0 6.0	.75” Semi-Circle	6.9

Hadjiev, Sabiri and Zanati suggest that when gas flow rates are high the mixing times can increase, or decrease due to interaction between the bubbles and the impellers [29].

The mixing times obtained in this study were compared to the experimental k_La values to examine the possibility of a correlation. The following figures plot the k_La of each tank configuration versus the mixing time at the two flow rates. In these figures the mixing times of 10.5, 11.2, 15.8, and 16.0 seconds correspond to only one experimental data point. However, the mixing times of 6.8 and 8.3 seconds correspond to multiple experimental data points.

Table 9: Mixing Times for the Four-Impeller Configurations

Impeller Configuration	Impeller Diameter (in)	Baffle Type	Mixing Time (sec)
Rushton	6.0	Flat	6.8
Rushton	6.0		
Rushton	6.0		
Rushton	6.0		
Rushton	6.0	Film-Covered	8.3
Rushton	6.0		
Rushton	6.0		
Rushton	6.0		
Smith	6.25	Flat	11.6
Smith	6.25		
Smith	6.25		
Smith	6.25		
Smith	6.25	1.5" Semi-Circle	6.6
Smith	6.25		
Smith	6.25		
Smith	6.25		
He3	6.0	Flat	9.9
Rushton	6.0		
Rushton	6.0		
Rushton	6.0		
He3	6.0	Flat	15.8
He3	6.0		
Rushton	6.0		
Rushton	6.0		
He3	6.0	Flat	10.5
Smith	6.25		
Smith	6.25		
Smith	6.25		
He3	6.0	Flat	12.1
He3	6.0		
Smith	6.25		
Smith	6.25		

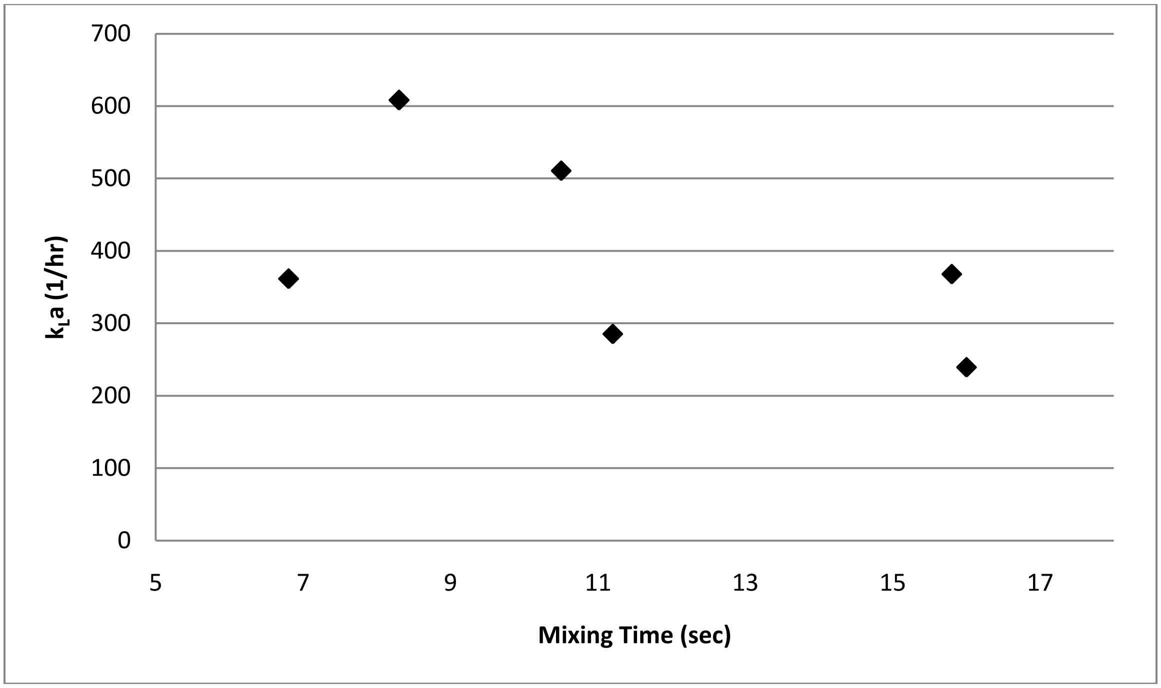

Figure 24: k_La versus mixing time for data obtained at a gas flow rate of 140 lpm.

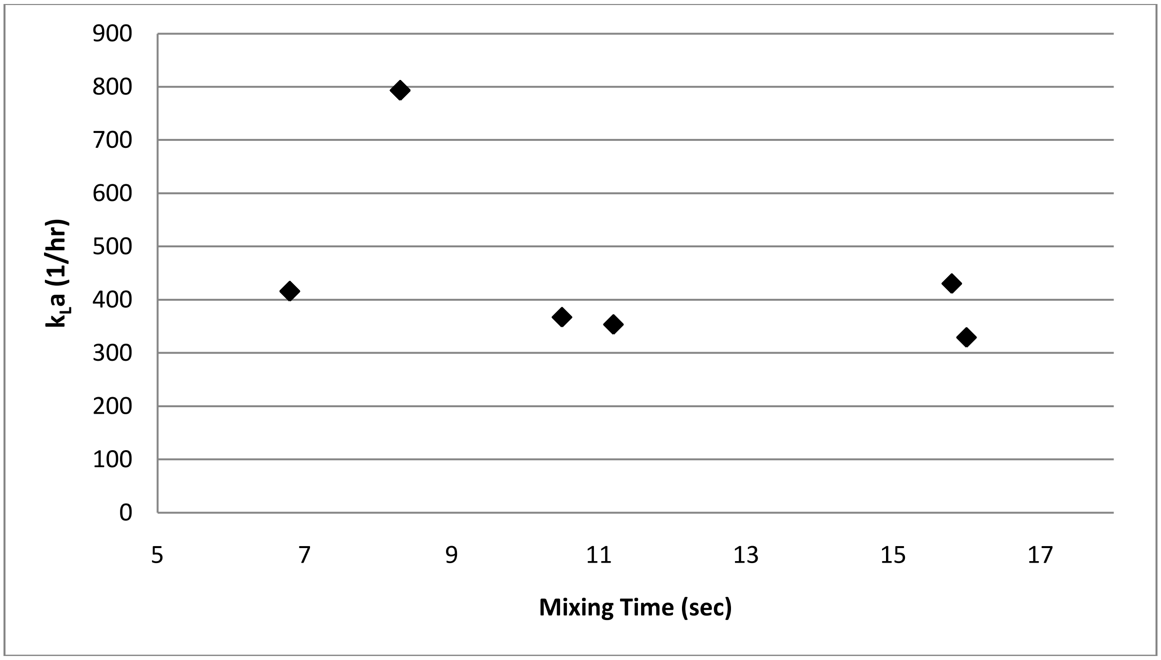

Figure 25: k_La versus mixing time for data obtained at a gas flow rate of 170 lpm.

As seen in these figures the mixing times do not correlate to the experimentally determined $k_L a$ values. Due to this lack of correlation, gas flow rates of 25 and 40 liters per minute were tested for four additional tank configurations. These additional tests are outlined in Table 10 and plotted in Figure 26 and Figure 27.

Figure 26 and Figure 27 show that a correlation between mixing time and $k_L a$ might be possible. However, these systems are very complex and have several factors that affect mixing time and $k_L a$. Reducing these correlations to just two variables ($k_L a$ and mixing time) is likely oversimplifying the phenomena that are occurring in a stirred tank.

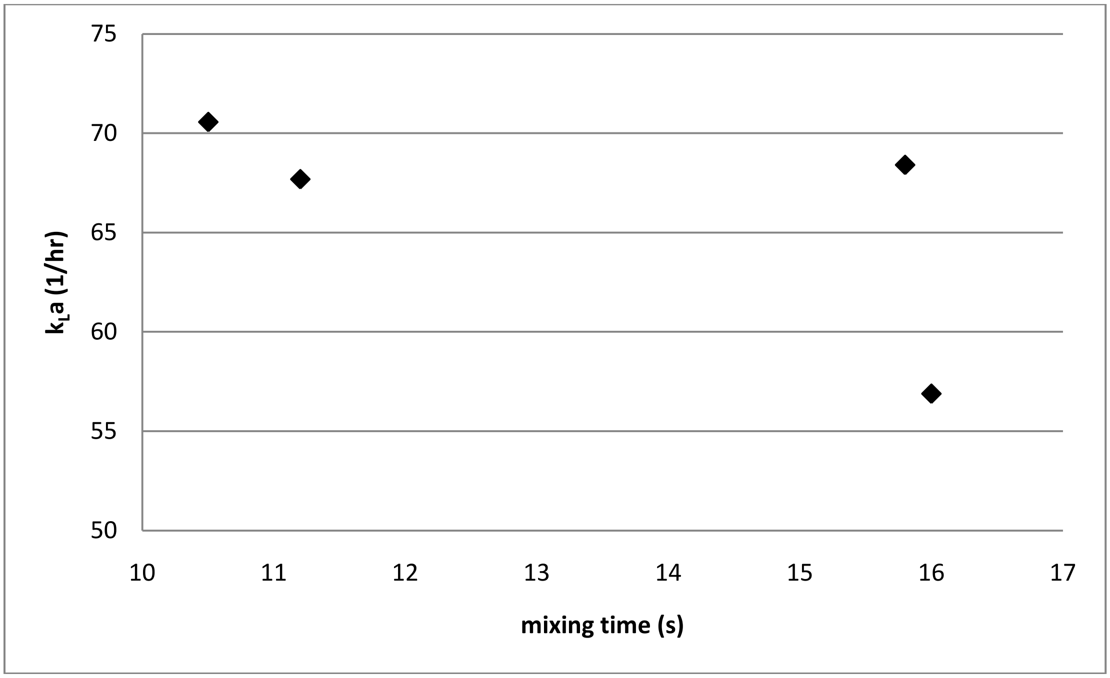

Figure 26: $k_L a$ versus mixing time for data obtained at a gas flow rate of 25 lpm.

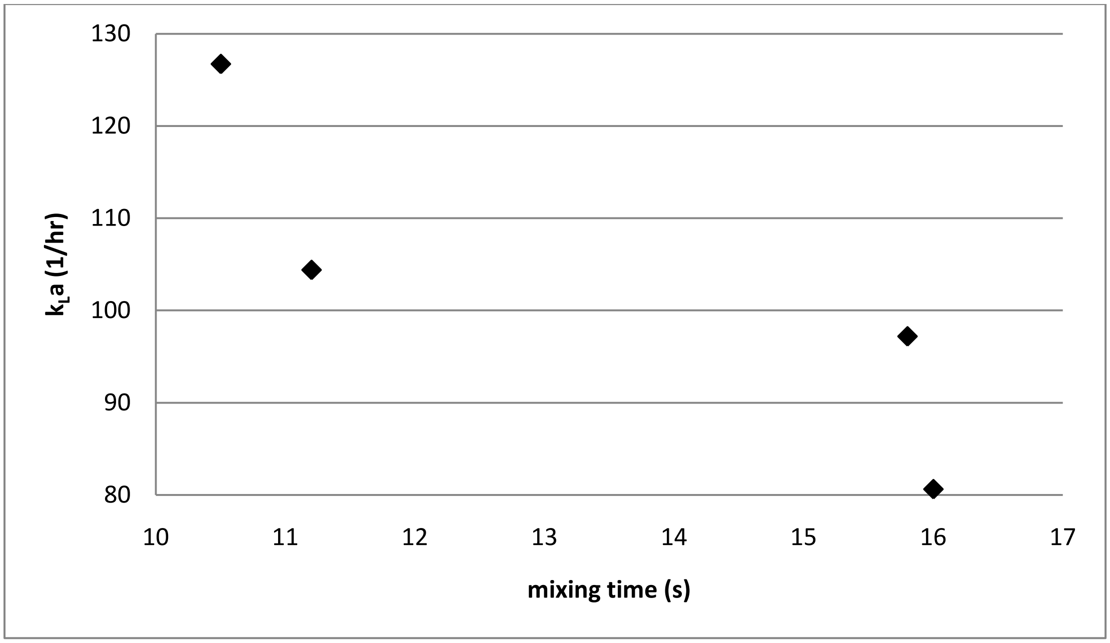

Figure 27: k_La versus mixing time for data obtained at a gas flow rate of 40 lpm.

Table 10: Additional k_La Testing Performed at Gas Flow Rates of 25 and 40 Liters per Minute

Impeller Configuration	Baffle Type	Mixing Time (s)	k_La	
			25 lpm	40 lpm
He3 He3 Rushton	Flat	16.0	56.8	80.6
He3 He3 Smith	Flat	15.8	68.4	97.2
A320 A320 Rushton	Flat	11.2	67.7	104
A320 A320 Smith	Flat	10.5	70.6	127

CFD Results and Mixing Capabilities

The CFD results calculated in this study can be used to give a better understanding of mixing in stirred tanks, and how certain aspects of the tank produce better mixing. In Figure 28 and Figure 29 we see the middle and lower impellers of two tank configurations, one using A320 impellers and one using He3 impellers. These pictures are a slice of the mid-plane of the tank and the arrows represent the direction of flow. The different colors of arrows represent faster moving fluid, where the length of the arrows represents the direction of the fluid moving at that point. Where the arrows

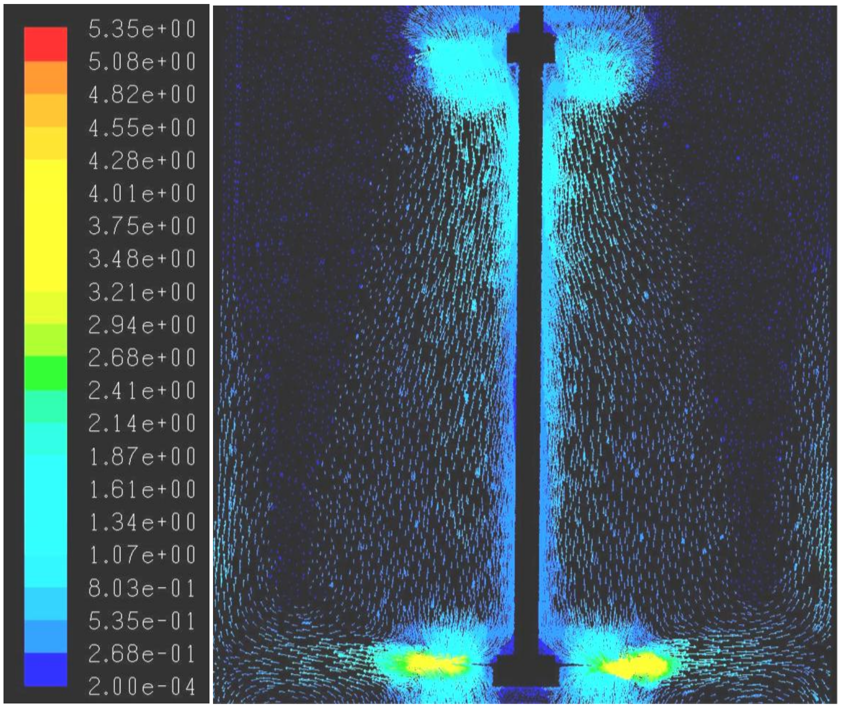

Figure 28: Flow visualization of middle and lower impellers of the He3-He3-Rushton tank configuration.

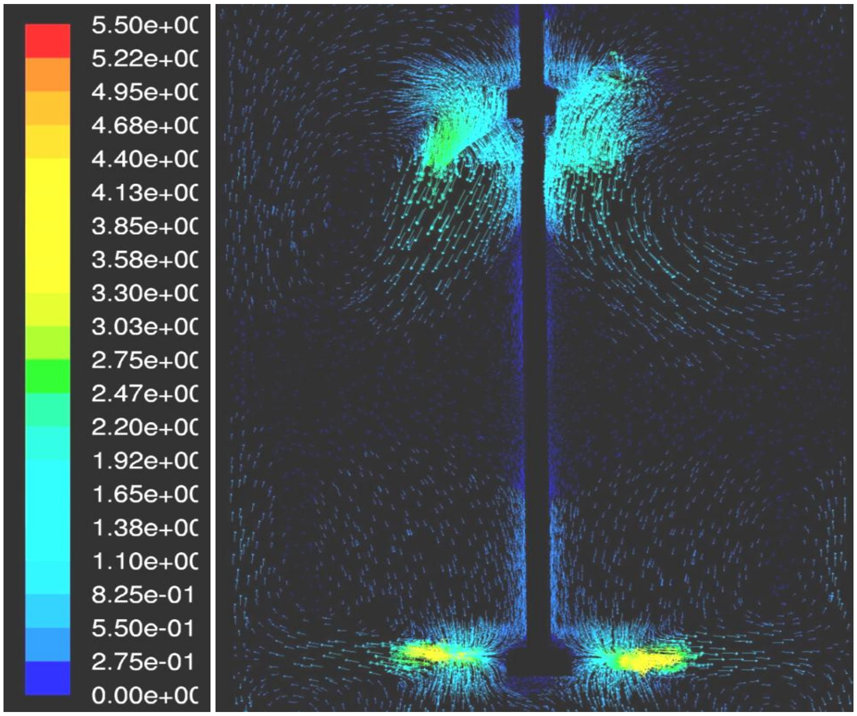

Figure 29: Flow visualization of middle and lower impellers of the A320-A320-Rushton tank configuration.

are longer, the fluid is moving more in line with the mid-plane of the tank; where the arrows are shorter they are moving more perpendicular to the mid-plane of the tank.

From these we can see that the He3 impeller acts as more of an axial flow impeller than the A320, and thus creates more fluid interaction with the Rushton impeller. However, the A320 impeller, which acts more like a mixed flow impeller, creates eddies with the side wall of the tank. These eddies have higher fluid velocities than those produced by the He3 impeller. These eddies also likely produce better side-to-side mixing of the tank, while the interaction between the He3 and Rushton impellers likely produce better top-to-bottom mixing. These same interactions are noted when the Rushton is replaced with the Smith impeller. In addition, where A320 impellers are used mixing times are better than those where He3 impellers are used. In these figures it is also noteworthy to mention the “dead” zones that occur half way between the impellers. The fluid coming off the impellers looses momentum and comes to almost a complete stop in the very dark areas of the visualizations.

When the three and four-Rushton impeller configurations are compared with one another it is expected that the latter will perform better. In Figure 30 we see that in the three-Rushton configuration the flow from one impeller does not interact with the other creating a dead zone between the two. In the four-Rushton configuration (Figure 31) we do not see the dead zone as before. In fact, in this configuration we see that the fluid coming off one impeller creates eddies through the interaction with the fluid coming off the other impeller. When comparing the mixing times between the three and four-impeller models we note that, on average, the four-impeller models perform better. However, the three-Rushton impeller configurations seem to perform only slightly worse than the four-impeller configurations.

The baffles used in these calculations were studied to see how much disruption of flow they created. In Figure 32, Figure 33 and Figure 34 cross sections of the stirred tank are shown to see this flow disruption. The cross-sections pictured are taken at mid-distance between the middle and upper impeller in the three-Rushton tank.

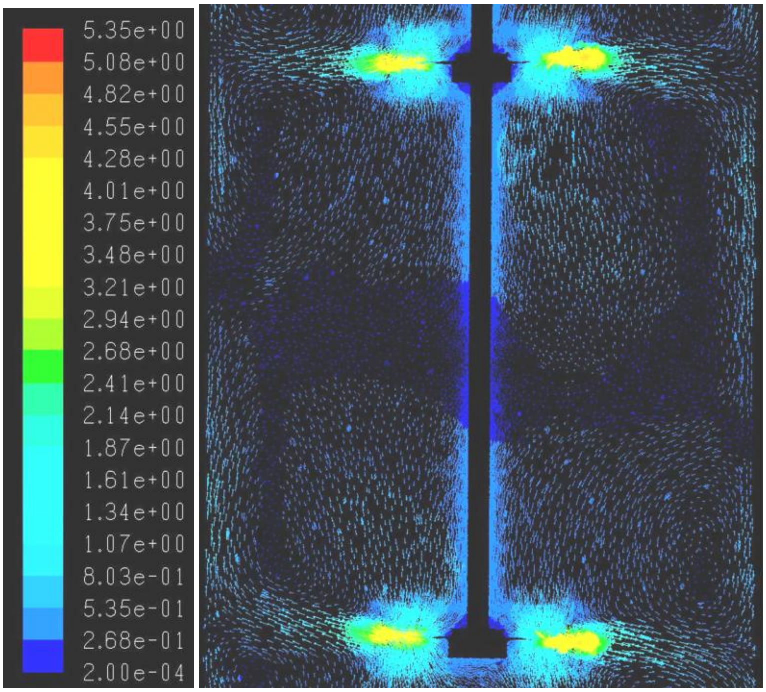

Figure 30: Flow visualization of middle and lower impellers of the Three-Rushton tank configuration.

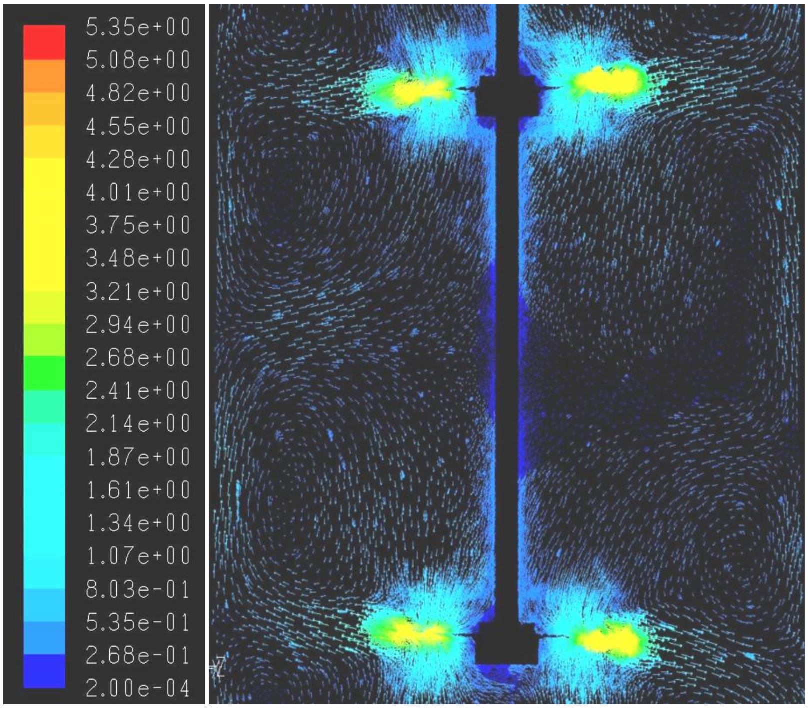

Figure 31: Flow visualization of middle and lower impellers of the Four-Rushton tank configuration.

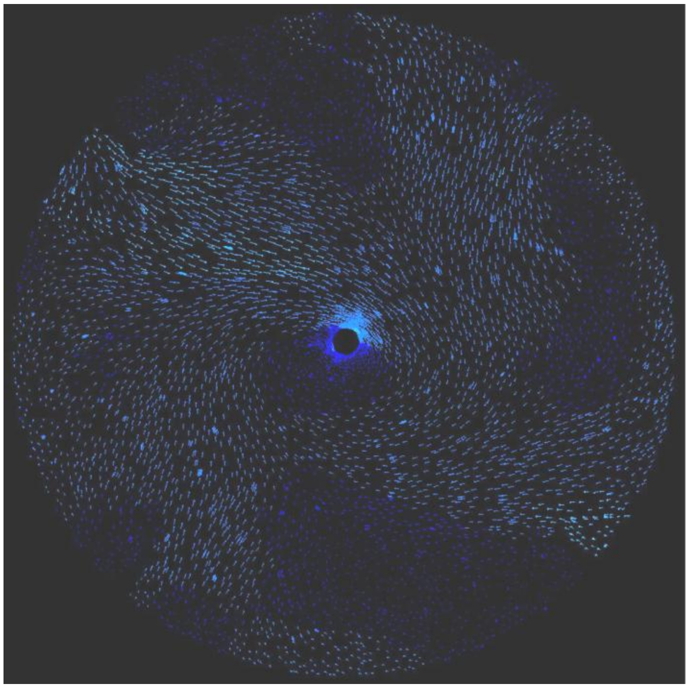

Figure 32: Flow visualization of a cross section of the Three-Rushton tank with flat baffles.

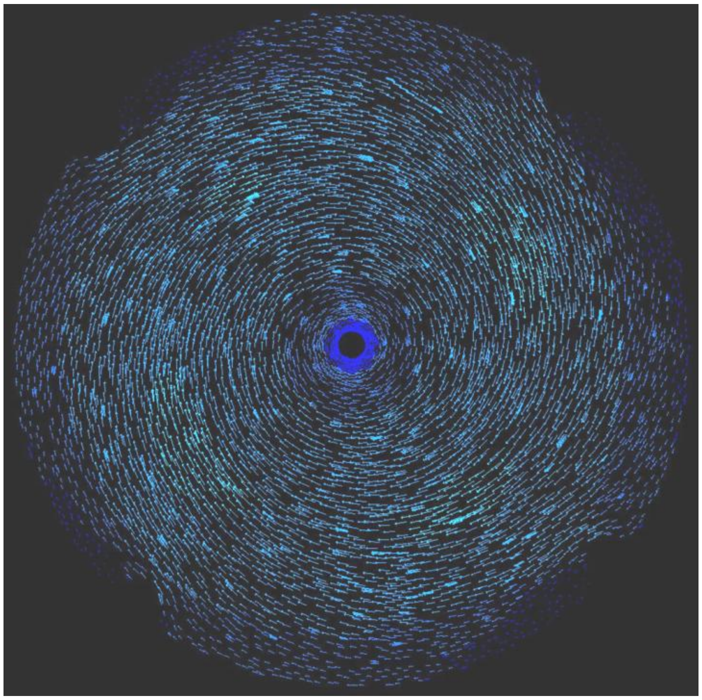

Figure 33: Flow visualization of a cross section of the Three-Rushton tank with .75” round baffles.

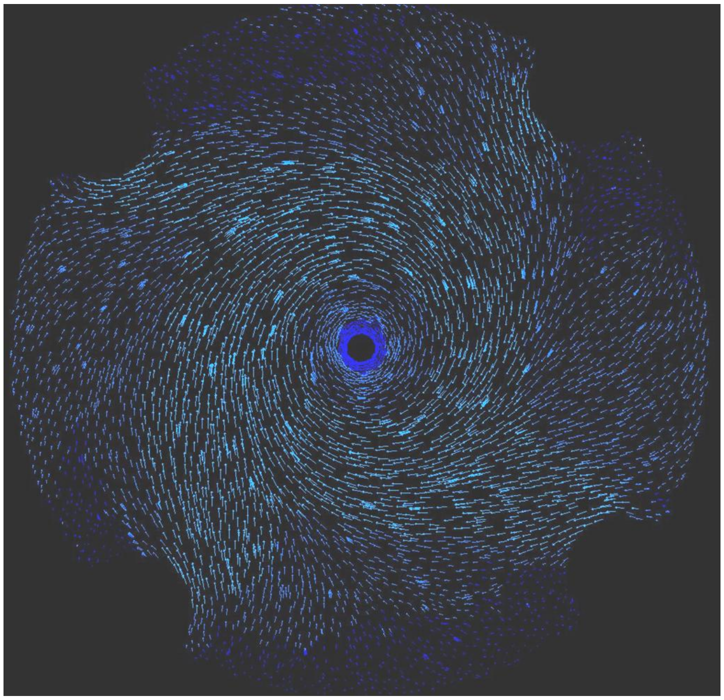

Figure 34: Flow visualization of a cross section of the Three-Rushton tank with 1.5” round baffles.

From these figures we see that both the large and small round baffles create higher fluid velocities in the tank. However, for the small round baffles almost all of the fluid in the tank is moving in a uniform circular motion. These circular streamlines indicate a lack of mixing in the radial direction. The large round baffles create more disruption than the smaller ones. Although, these still have some of the uniform motion near the center of the tank, which could create similar circular streamlines. The mixing times suggest that the large round baffles have comparable or even better mixing capability than the flat baffles. Nevertheless, the mixing times are too close to differentiate between the two. As seen in Figure 35, the film-covered baffles disrupt the flow just as much as the flat baffles, and the mixing times suggest they are comparable as well.

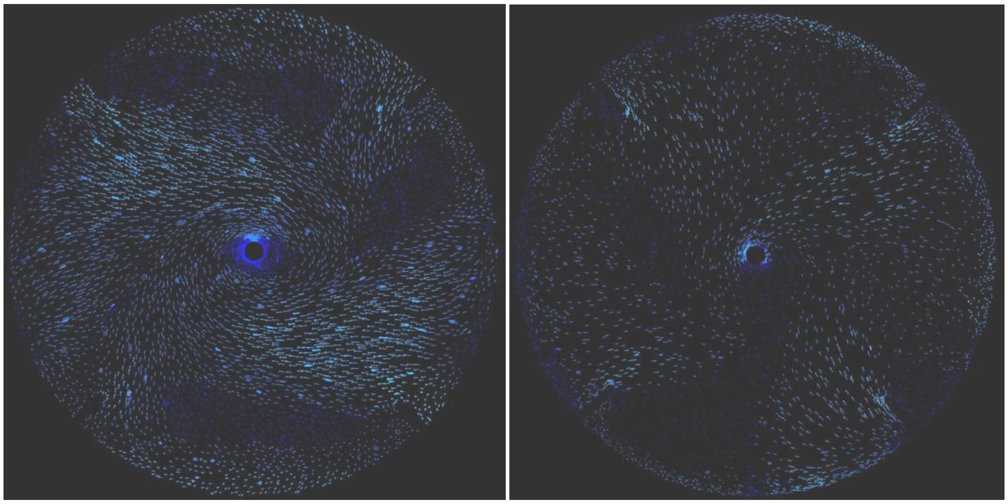

Figure 35: Flow visualizations of cross sections of the Four-Rushton tank with flat (left) and film-covered (right) baffles.

From the preceding results we can conclude that there are differences in the impellers and baffles. The mixing times predict that, in this size of tank, the A320 impellers perform better than the He3 impellers. The results also show a difference seem to have similar results, all of which provide better disruption than the small round baffles. For a complete listing of the CFD results obtained see Appendix B.

Dimensionless Number Correlation

In order to study the dimensionless correlations presented by Schluter and Nishikawa, the experimental results from the stirred tank reactor were plotted against Equations (22) and (23). These plots, as shown in Figure 36 and Figure 37, show two things. First, neither the Schluter nor the Nishikawa equations accurately models the data. Second, there is a great distinction between Rushton impeller data and the cases

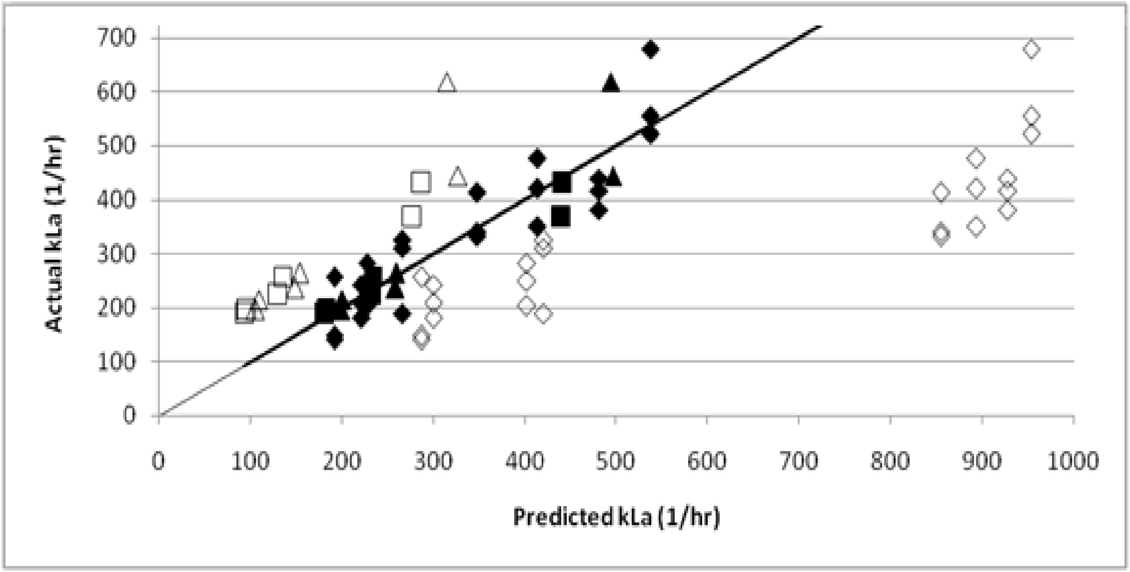

Figure 36: Plot of experimental data using the original (Eqn. 22) and modified Schluter equation. The hollow and solid markers represent the original and modified correlations, respectively. The diamond, square, and triangle markers represent the four-Rushton, two-HE3-one-Smith, and two-A320-one-Smith configurations, respectively. (The line shows a 1:1 comparison of the experimental and predicted values)

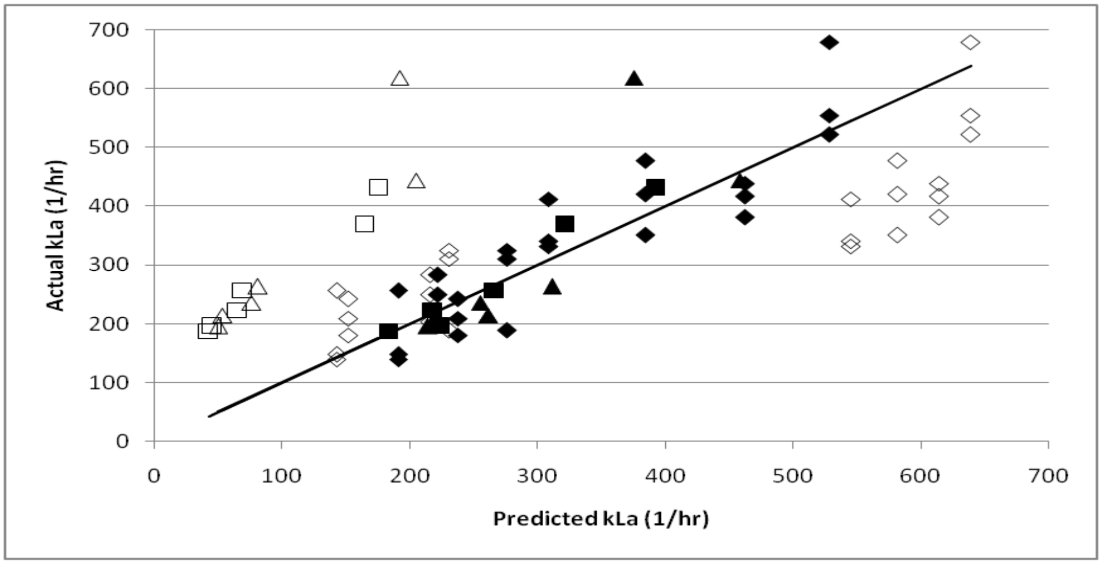

Figure 37: Plot of experimental data using the original (Eqn. 23) and modified Nishikawa equations. The hollow and solid markers represent the original and modified correlations, respectively. The diamond, square, and triangle markers represent the four-Rushton, two-HE3-one-Smith, and two-A320-one-Smith configurations, respectively. (The line shows a 1:1 comparison of the experimental and predicted values)

where axial flow impellers are used. The Schluter equation over predicts k_La for the Rushtons, but under predicts k_La for the cases with axial flow impellers. The Nishikawa equation follows a similar pattern by over predicting k_La for the Rushtons, for high k_La values, and under predicting k_La for the other two cases. However, the Nishikawa equation seems to also under predict k_La for cases of reduced mass transfer. These errors in prediction may be due to the use of un-corrected values in the development of the correlation.

The average error in the prediction of k_La for each correlation was evaluated. The results, as shown in Table 11, indicate that the modified Schluter equation is the most accurate tool for predicting k_La. The modified Schluter equation is based on Equation (22); however, different values of *C*, *a*, and *b* are used, as outlined in Table 12. The constants were calculated by fitting Equation (22) to the corrected experimental data. An example of how this correlation can be used to predict k_La is shown in Figure 38. The correlation can be useful in determining which operating conditions or impeller configurations are needed to obtain a desired k_La.

Table 11: Percent Error in k_La Prediction for Various Correlations

	Schluter		Nishikawa	
	Original	Modified	Original	Modified
Four Rushtons	86.5	15.7	30.2	16.6
Two HE3, One Smith	41.5	7.7	68.7	7.3
Two A320, One Smith	41.6	8.7	68.2	16.7
Average	56.5	10.7	55.7	13.5

Table 12: Constants Obtained for Equation (22) by the Use of Corrected Experimental Values

	C	a	b
4-Rushton	0.9953	0.4468	1.072
Smith, 2-Axial	1.74×10^{-4}	0.6479	2.35×10^{-2}

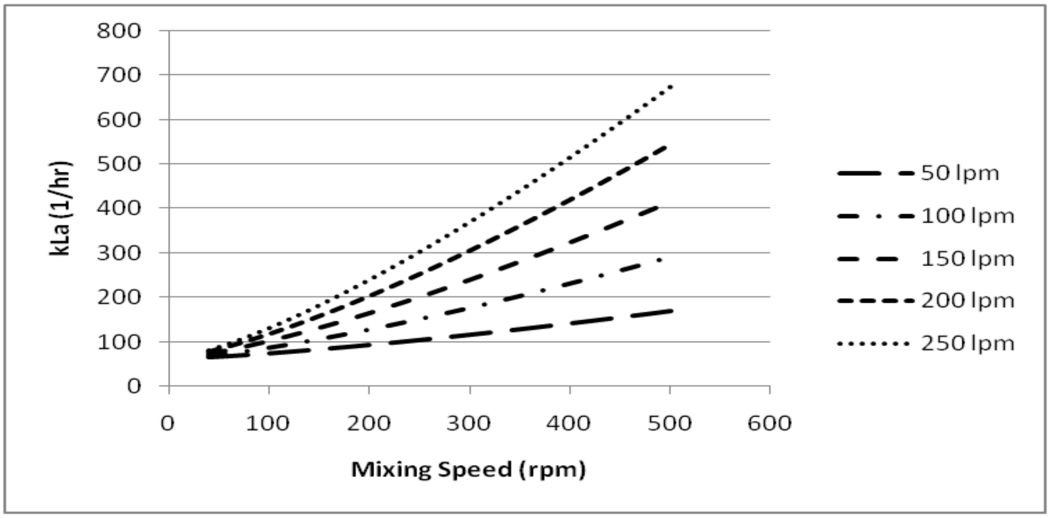

Figure 38: Plot of predicted oxygen mass transfer rates in a 250 L fermentation vessel with four Rushton impellers at different mixing speeds and gas flow rates.

Error Analysis and Uncertainty Range

In order to calculate the uncertainty of these calculations first the uncertainties of the individual components need to be known. The uncertainties of the time constants were calculated from the standard deviations observed in the experiments conducted. Since the probes were calibrated before each experiment, the precision uncertainty on the percent oxygen readings was neglected in the calculation. However, the bias uncertainty is given as 0.3% of readout. Since k_La is usually calculated between 20% and 75% dissolved oxygen, the average uncertainty equates to .1425%. The uncertainties for the two time constants were calculated from a standard T distribution using a 95%

confidence. The uncertainty of the first time constant (τ_1) is .35998 seconds and the uncertainty of the second time constant (τ_2) is .7988 seconds. To calculate the uncertainty of a single corrected data point Equation (19) (represented as "*y*") is used to propagate the uncertainty according to the following equation.

$$U_{cdp} = \sqrt{\left(\frac{\partial y}{\partial \tau_1} U_{\tau_1}\right)^2 + \left(\frac{\partial y}{\partial \tau_2} U_{\tau_2}\right)^2 + \left(\frac{\partial y}{\partial C} U_{C_b}\right)^2} \tag{44}$$

According to Equation (44) the uncertainty of a single corrected data point is .952% dissolved oxygen. From this, an uncertainty on the slope of the linearized data points can be calculated. Bevington and Robinson [30] derive a measure of the uncertainty of the slope of a least-squares fit to a straight line according to the following equation.

$$U_{slope} = N_{dp} \frac{{U_{cdp}}^2}{\left(N_{dp} \sum {x_i}^2 - (\sum x_i)^2\right)} \tag{45}$$

Using these equations, the bias uncertainty of a k_La measurement of 786 is 65.3 hr^{-1}. The precision uncertainty, calculated using a standard T distribution with a 95% confidence, is 71.6 hr^{-1}. Taking into account these two uncertainties, the uncertainty on a k_La measurement of 786 hr^{-1} is 96.9 hr^{-1}.

This means that if an experimenter calculated a k_La of 175 hr^{-1} without using any corrections, then correcting for the time response of the probes would give a value of 985 hr^{-1}. After correcting for the transient time period (assuming 8 seconds for the transient period) the k_La would then be 805 hr^{-1} +/- 96.9 hr^{-1}.

CHAPTER 7

CONCLUSIONS

The second-order probe response model is an effective tool in correcting for a slow response time in dissolved oxygen sensors. Using this technique, any dissolved oxygen measurement can be corrected, as long as the time response of the probes is known. This technique can be applied to probes that have both slow and fast time responses, although, for a probe with a fast time response, the correction might be negligible.

The method developed to account for a transient volume rise gives a correction for k_La values that have been affected by the volume rise. The method shows that the distortion in calculated k_La is due to the number of data points used in the calculation that fall within the transient time period according to equation (46).

From the experimental k_La studies we see that for a 250 liter tank with a 3:1 height to diameter ratio, four Rushton impellers used with the film-covered baffles creates the best conditions for mass transfer. The axial flow impellers so not seem to have any advantage, or disadvantage over the radial flow impellers. Numerically calculated mixing times do not correlate with mass transfer for the gas flow rates used by this STR and thus can only be used to give information on mixing.

Numerical studies for this STR give important information on how different baffles and impellers affect the mixing. For the three-impeller configurations the fluid mixing zones do not interact with each other, creating dead zones in the tank. When using the He3 impeller, there is more interaction between fluid zones, but there are still large areas of very slow moving liquid. The four-impeller configurations do not experience these dead zones, and thus produce better mixing conditions. Mixing times calculated from these studies suggest that the 0.75 inch round baffles do not create good disruption in the tank, thus impeding the mixing. However the other three types of baffles all provide very good disruption and mixing, especially when used with radial flow impellers. Future research on this subject would benefit from including experimental k_La studies using all three types of baffles and distinguishing the advantages and disadvantages of each.

Finally, dimensionless correlations present a useful tool for scale-up and design of stirred tank fermentors. However, these models must be developed from data where the probe response time and the transient volume rise have both been accounted for. The correlations that have been developed previous to this work do not accurately model the data. The correlations developed in this study more accurately model the data and are useful for the design of 250 L stirred tank fermentors. However there are limitations to these correlations and they should be tested further when used for other sizes and shapes of tanks.

REFERENCES

[1] Nielsen, J., "Fermentation Monitoring, Design and Optimization," *Encyclopedia of Bioprocess Technology*, John Wiley & Sons, Lyngby, Denmark, 2008.

[2] Chisti, Y., "Solid Substrate Fermentations, Enzyme Production, Food Enrichment," *Encyclopedia of Bioprocess Technology*, John Wiley & Sons, Almeria, Spain, 2008.

[3] Murphy, B. and Walsh, G., *Biopharmaceuticals, an Industrial Perspective*, Springer, 1999.

[4] Thiry, M. and Cingolani, D., "Optimizing scale-up fermentation processes," *Trends in Biotechnology*, vol. 20, no. 3, 2002, pp. 103–105.

[5] Wernersson, E.S., and Trägårdh, C., "Scaling of turbulence characteristics in a turbine-agitated tank in relation to agitation rate," *Journal of Chemical Engineering*, vol. 70, 1998, pp. 37–45.

[6] Oosterhuis, N.M.G., Siebel, M.A., and Mijnbeek, G., *Bioreactor Design and Product Yield*, Butterworth-Heinemann, 1992, pp. 8-47.

[7] Whitman, W.G., "Preliminary Experimental Confirmation of the Two-Film Theory of Gas Absorption," *Chemical and Metallurgical Engineering*, vol. 29, 1923, pp. 146-149.

[8] Gomez, E., and Garcia-Ochoa, F., "Bioreactor Scale-Up and Oxygen Transfer Rate in Microbial Processes: An Overview," *Biotechnology Advances*, vol. 27, 2009, pp. 153-176.

[9] Prasertsan, P., and Bandaiphet, C., "Effect of aeration and agitation rates and scale-up on oxygen transfer coefficient, kLa in exopolysaccharide production from Enterobacter cloacae WD7," *CARBOHYDRATE POLYMERS*, vol. 66, no. 2, 2006, pp. 216-228.

[10] Wilson, J., and Charles, M., "Fermenter Design," *Encyclopedia of Bioprocess Technology*, John Wiley & Sons, 1999, pp. 1157-1189.

[11] Weetman, R.J., "Development of Transitional Flow Mixing Impeller," Proceedings of The 7th European Conference on Mixing, Belgium, 1991.

[12] Cooney, C.L, Demain, A.L., Dunnill, P., Humphrey, A.E., Lilly, M.D., Wang, D.I.C., *Fermentation and Enzyme Technology*, John Wiley & Sons, 1978, pp. 157-192.

[13] Chapman, F.S., Holland, F.A., *Liquid Mixing and Processing in Stirred Tanks*, Reinhold, New York, 1966.

[14] Reeder, M.F., Fasano, J.B., and Myers, K.J., "Optimize Mixing by Using the Proper Baffles," *CEP Magazine*, vol. 98, no. 2, February 2002. [www.cepmagazine.org Accessed August 1, 2008]

[15] Oldshue, J.Y., *Fermentation and Biochemical Engineering Handbook, 2nd Ed*, William Andrew, 1997, pp. 181-241.

[16] Nauman, E.B., *Chemical Reactor Design, Optimization and Scale-Up*, McGraw Hill, New York, 2002.

[17] Kenty, B.M., Li, Z.J., Lee, S.S., and Xing, Z., "Scale-Up Analysis for a CHO Cell Culture Process in Large-Scale Bioreactors," *Biotechnology and Bioengineering*, vol. 103, no. 4, 2009.

[18] Thornton, E.A., Byron, T.D., and Heubner, K.H., *The Finite Element Method for Engineers*, 3rd ed., John Wiley & Sons, 1995.

[19] Montes, F.J., Galan, M.A., and Martin, M., "On the Contribution of the Scales of Mixing to the Oxygen Transfer in Stirred Tanks," *Chemical Engineering Journal*, vol. 145, 2008, pp. 232-241.

[20] Phillichi, T.L., and Stenstrom, M.K., "Effects of Dissolved Oxygen Probe Lag on Oxygen Transfer Parameter Estimation," *Journal of Water Pollution Control Federation*, vol. 61, no. 1, 1989, pp. 83-86.

[21] Yano, H., Yoshinaga, F., and Kouda, T., "Effect of agitator configuration on bacterial cellulose productivity in aerated and agitated culture," *Journal of Fermentation and Bioengineering*, vol. 38, no. 4, 1997, pp. 371–376.

[22] Doran, P.M., *Bioprocess Engineering Principles*, Sagebrush Education Resources, 1995.

[23] Fluent Inc., *Fluent 6.3 User's Guide*, Fluent Inc., 2006.

[24] Beckwith, T.G., Marangoni, R.D., and Lienhard V, J.H., *Mechanical Measurements*, Fifth Edition, Addison-Wesley Publishing Company, Inc., 1993.

[25] Chapra, S.C., and Canale, R.P., *Numerical Methods for Engineers*, Fifth Edition, McGraw Hill Higher Education, 2006.

[26] Deckwer, W.D., and Schluter, V., "Gas/Liquid Mass Transfer in Stirred Vessels," *Chemical Engineering Science*, vol. 47, no. 9-11, 1992, pp. 2357-2362.

[27] Nishikawa, M., Nakamura, M., Yagi, H., and Hashimoto, K., "Gas Absorption in Aerated Mixing Vessels," *Chemical Engineering Journal of Japan*, vol. 14, no. 219, 1981.

[28] Yu, P., Lee, T.S., Zeng, Y., and Low, H.T., "A 3D Analysis of Oxygen Transfer in a Low-Cost Micro Bioreactor for Animal Cell Suspension Culture," *Computer Methods and Programs in Biomedicine*, vol. 85, no. 1, 2007, pp. 59-68.

[29] Hadjiev, D., Sabiri, N.E., and Zanati, A., "Mixing Time in Bioreactors Under Aerated Conditions," *Biochemical Engineering Journal*, vol. 27, 2006, pp. 323-330.

[30] Bevington, P.R., and Robinson, D.K., *Data Reduction and Error Analysis*, 3rd ed., McGraw-Hill, New York, 2003.

[31] Weetman, R.J., Patel, B.R., and Hutchings, B.J., "Computation of Flow Fields in Mixing Tanks with Experimental Verification," *ASME Winter Annual Meeting*, San Francisco, 1989.

[32] Scholl, J., Vicum, L., Mazzotti, M., Brozio, J., and Lindenberg, C., "Experimental Characterization and Multi-Scale Modeling of Mixing in Static Mixers," *Chemical Engineering Science*, vol. 63, 2008, pp. 4135-4149.

[33] Woziwodzki, S., and Broniarz-Press, L., "The Mixing Time of Power-Law Fluids in a Vessel Equipped With Single and Dual Turbine Impellers," *Chemical and Process Engineering*, vol. 29, 2008, pp. 437-452.

[34] Schwarz, M.P., Evans, G.M., and Lane, G.L., "Predicting Gas-Liquid Flow in a Mechanically Stirred Tank," *Applied Mathematical Modeling*, vol. 26, 2002, pp. 223-235.

[35] Sannaes, B.H., Grevskott, S., Svendsen, H.F., and Jakobsen, H.A., "Modeling of Vertical Bubble-Driven Flows," *Ind. Eng. Chem. Res.*, vol. 36, 1997, pp. 4052-4074.

[36] T. Post. Mixing Forum, *Post Mixing Optimization and Solutions*. [http://www.postmixing.com/mixing%20forum/impellers/impellers.htm Accessed May 20, 2009.]

[37] Garćia-Ochoa, F., Gómez-Castro, E., and Santos, V.E., "Oxygen transfer and uptake rates during xanthan gum production," *Enzyme and Microbial Technology*, vol. 27, 2000, pp. 680–690.

[38] Gibbs, P.A., and Seviour, R.J., "Does the agitation rate and/or oxygen saturation influence exopolysaccharide production by Aureobasidium pullulans in batch culture?," *Applied Microbial and Biotechnology*, vol. 46, 1996, pp. 503–510.

[39] Miura, S., Arimura, T., Hoshino, M., Kojima, M., Dwiarti, L., and Okabe, M., "Optimization and scale-up of l-lactic acid fermentation by mutant strain Rhizopus sp. MK-96-1196 in airlift bioreactors," *Journal of Bioscience and Bioengineering*, vol. 96, no. 1, 2003, pp. 65–66.

[40] Montes, F.J., Catalan, J., and Galan, M.A., "Prediction of kLa in yeast broths," *Process Biochemistry*, vol. 34, 1998, pp. 549–555.

[41] Tuffile, C.M., and Pinho, F., "Determination of oxygen transfer coefficients in viscous Streptomycetes fermentations," *Biotechnology and Bioengineering*, vol. 12, 1970, pp. 849–871.

[42] Javed, K.H., Mahmud, T., and Zhu, J.M., "Numerical Simulation of Turbulent Batch Mixing in a Vessel Agitated by a Rushton Turbine," *Chemical Engineering and Processing*, vol. 45, 2006, pp. 99-122, 2006.

[43] Weetman, R.J., "Automated Sliding Mesh CFD Computations for Fluidfoil Impellers," *9th European Conference on Mixing*, Paris, 1997.

[44] Schuster, A., Sefiani, K., and Ponton, J., "Multiphase Mass Transport in Micro/Mini-Channels Microreactor," *Chemical Engineering Research and Design*, vol. 86, 2008, pp. 527-534.

[45] Mueller, J.A., Boyle, W.C., and Lightfoot, E.N., "Effect of Response Time of a Dissolved Oxygen Probe on the Oxygen Uptake Rate," *Applied Microbiology*, vol. 15, no. 3, 1967, pp. 674-676.

[46] Weiland, P., and Onken, U., "Fluid Dynamics and Mass Transfer in an Airlift Fermentor with External Loop," *German Chemical Engineering*, vol. 4, 1981, pp. 42-50.

[47] Vasconselos, J.M.T., Orvalho, S.C.P., Rodrigues, A.M.A.F., and Alves S.S., "Effect of Blade Shape on the Performance of Six-Bladed Disk Turbine Impellers," *Ind. Eng. Chem. Res.*, 2000, pp. 203-213.

APPENDICES

Appendix A: Experimental Results

Table 13: Tabulated Experimental Results

Impeller Configuration	Baffle Type	Impeller Speed (rpm)	k_La (1/hr) (corrected for probe response and transient volume rise)
He3 He3 Rushton	Flat	250	153
		300	208
		450	302
He3 He3 Smith	Flat	250	192
		300	241
		450	399
A320 A320 Rushton	Flat	250	141
		300	281
		450	357
A320 A320 Smith	Flat	250	205
		300	249
		450	531
Rushton Rushton Rushton Rushton	Flat	250	194
		300	258
		450	388
Rushton Rushton Rushton Rushton	Plastic Film	250	262
		300	361
		450	786

Appendix B: CFD Results

This appendix contains flow visualization pictures and mixing times from the CFD models used for this study. Each page contains the information from one of the CFD models including five flow visualization pictures. These pictures are: 1) a color-coded velocity scale of the velocity vectors in the remaining four pictures 2) a view of the y-z plane with y being the vertical direction 3) a view of the x-z plane at the mid-section of the first impeller 4) a view of the x-z plane at a point half way in-between two of the impellers 5) a view of the x-z plane at the mid-section of the upper-most impeller. Examples of the three and four-impeller configurations and where the pictures come from are shown below.

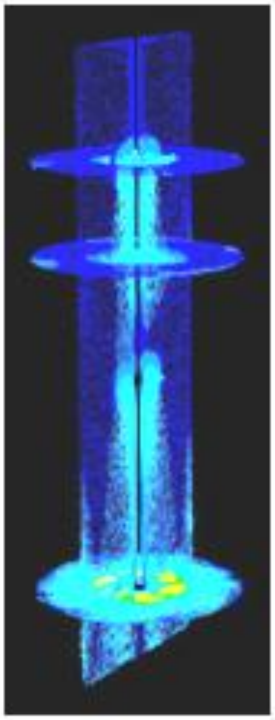

3-Impeller Configuration

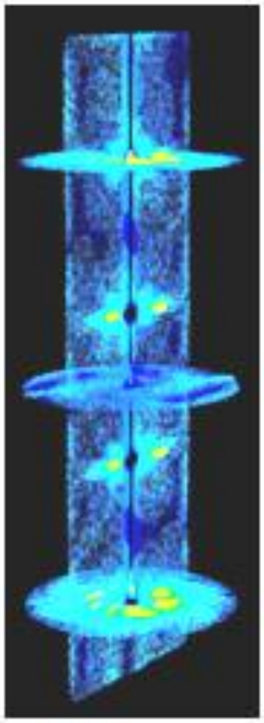

4-Impeller Configuration

Impeller Configuration	Impeller Diameter (in)	Baffle Type	Mixing Time (sec.)
He3	6.0	Flat	16.0
He3	6.0		
Rushton	6.0		

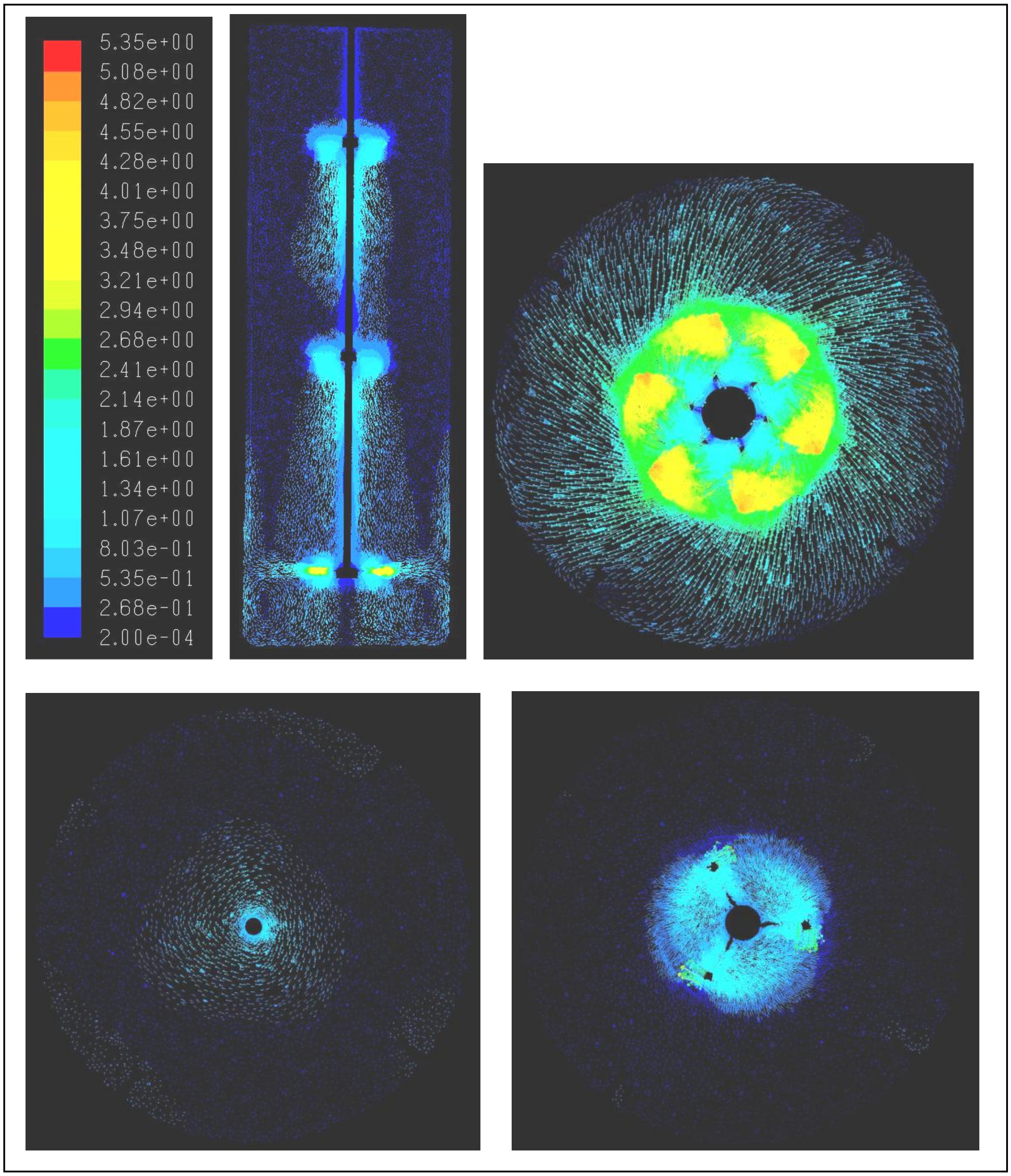

Impeller Configuration	Impeller Diameter (in)	Baffle Type	Mixing Time (sec.)
He3	6.0	Flat	15.8
He3	6.0		
Smith	6.25		

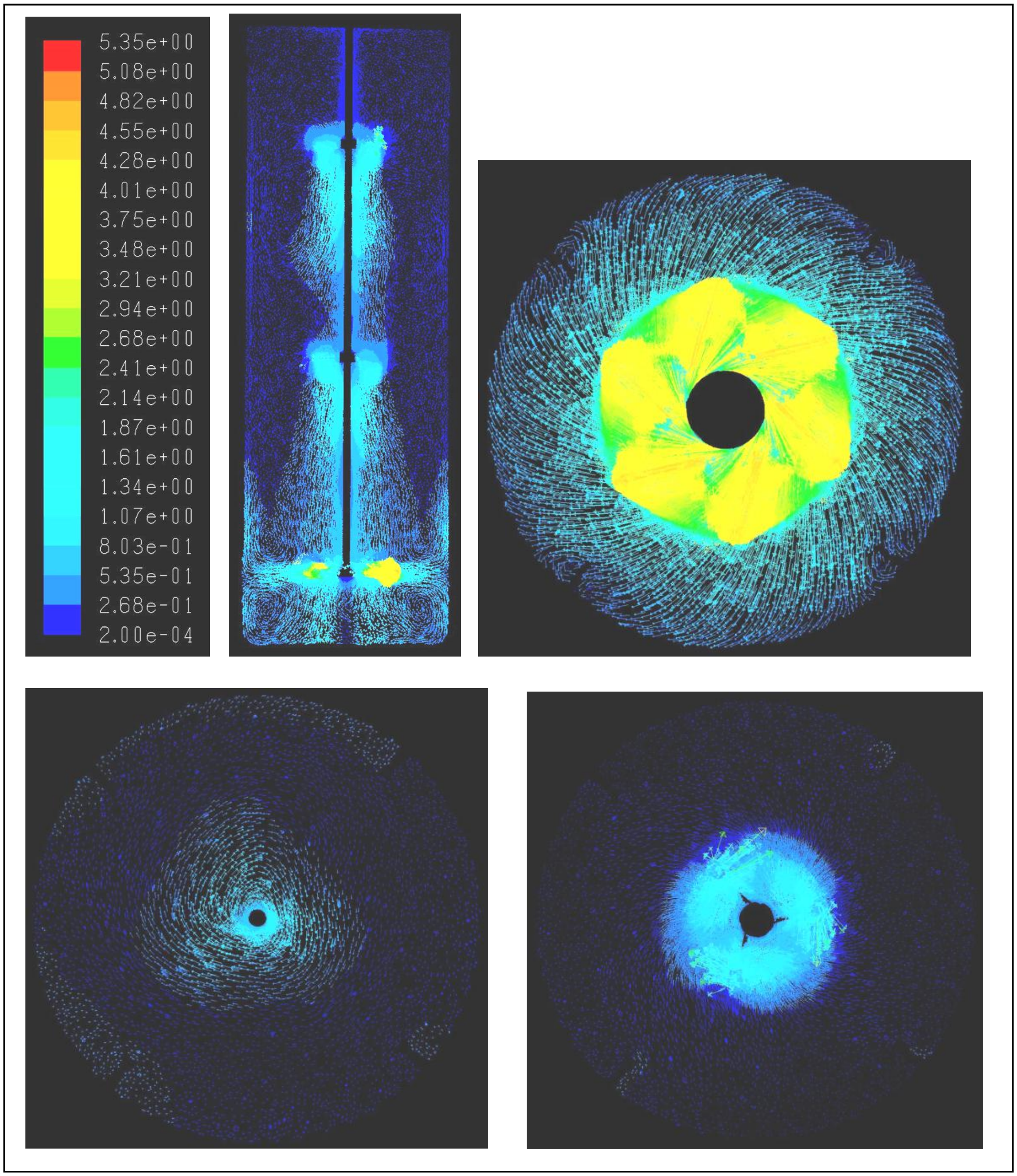

Impeller Configuration	Impeller Diameter (in)	Baffle Type	Mixing Time (sec.)
He3	6.0	1.5” Semi-circle	18.3
He3	6.0		
Smith	6.25		

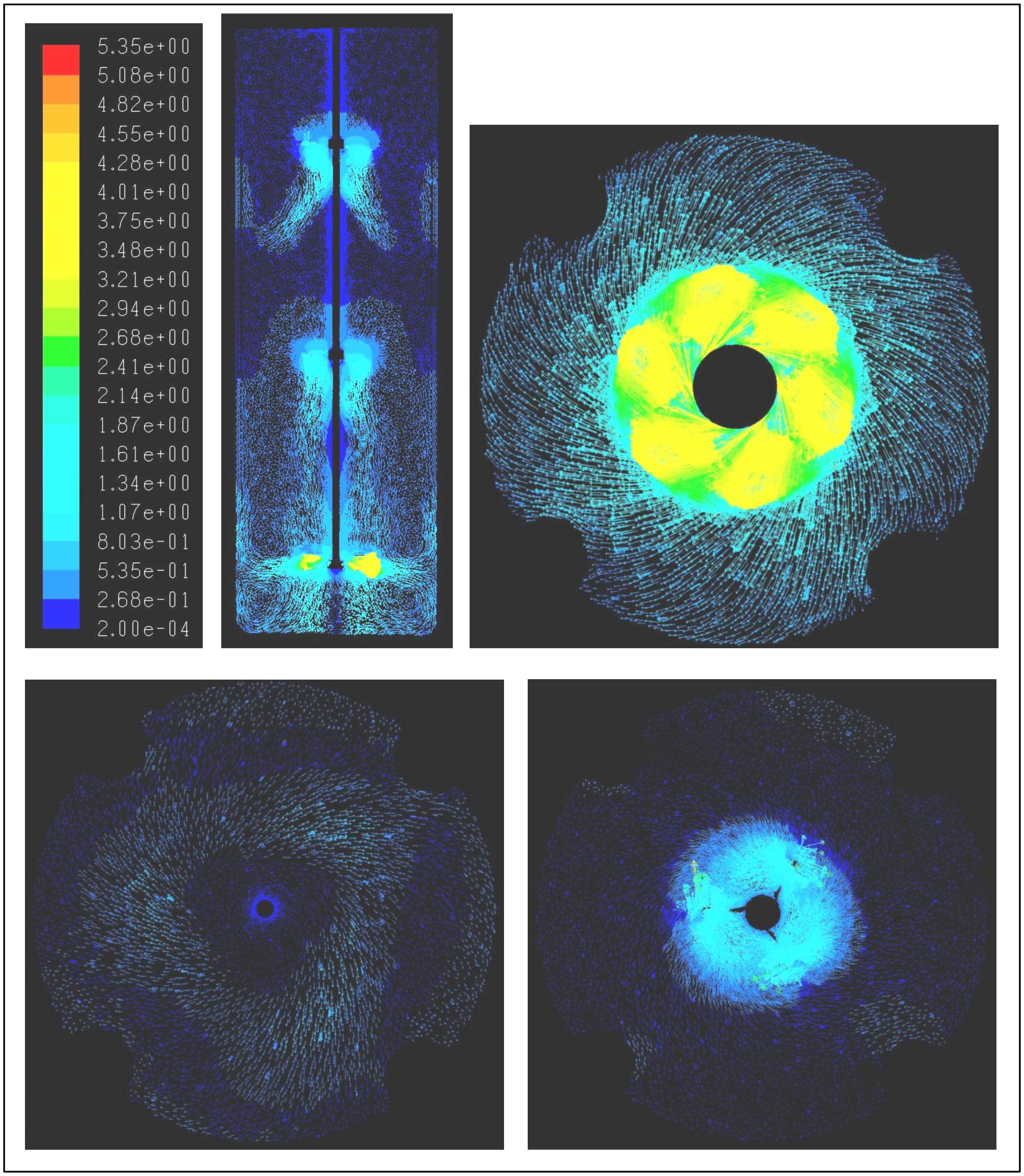

Impeller Configuration	Impeller Diameter (in)	Baffle Type	Mixing Time (sec.)
A320	6.0	Flat	11.2
A320	6.0		
Rushton	6.0		

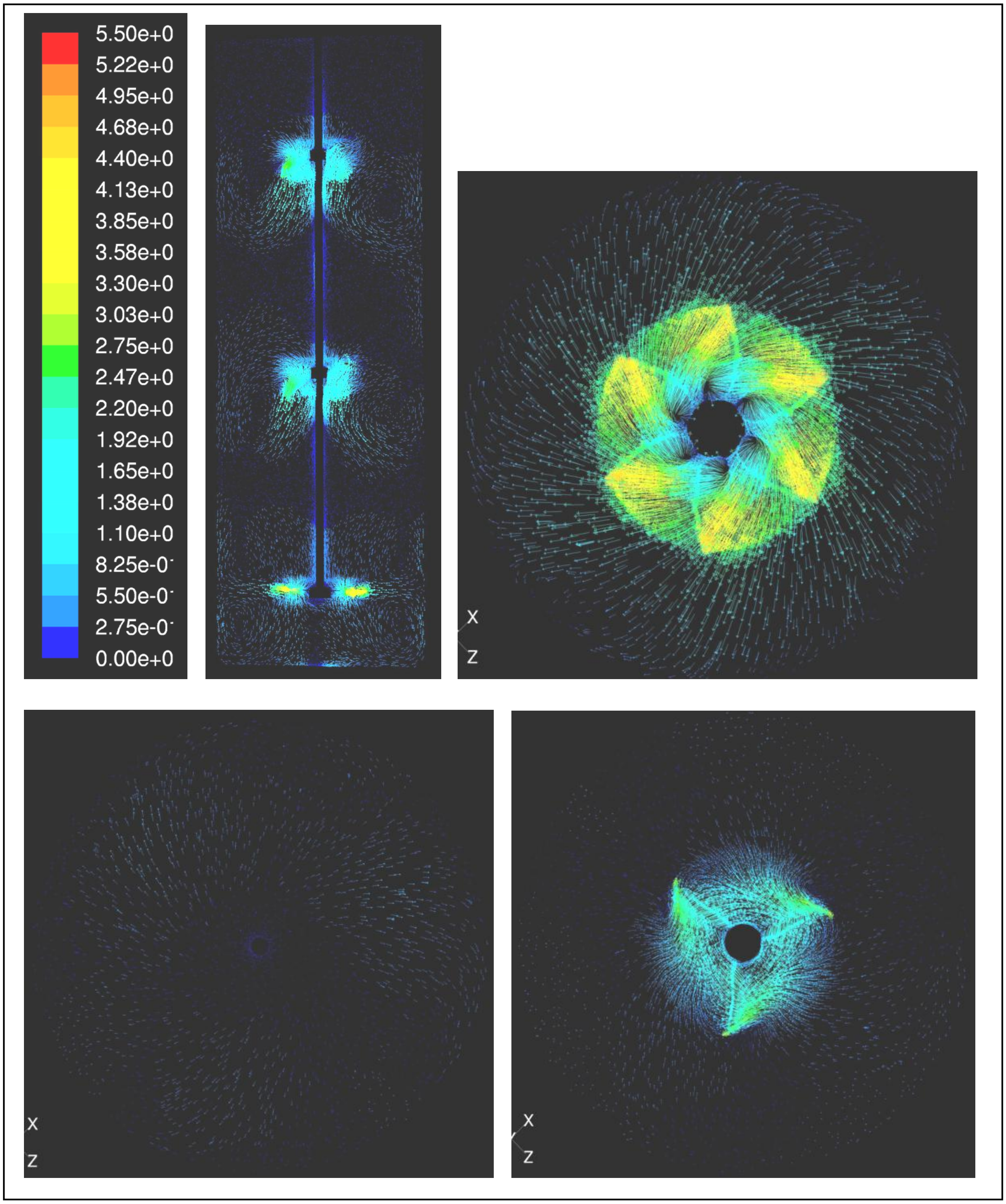

Impeller Configuration	Impeller Diameter (in)	Baffle Type	Mixing Time (sec.)
A320	6.0	Flat	10.5
A320	6.0		
Smith	6.25		

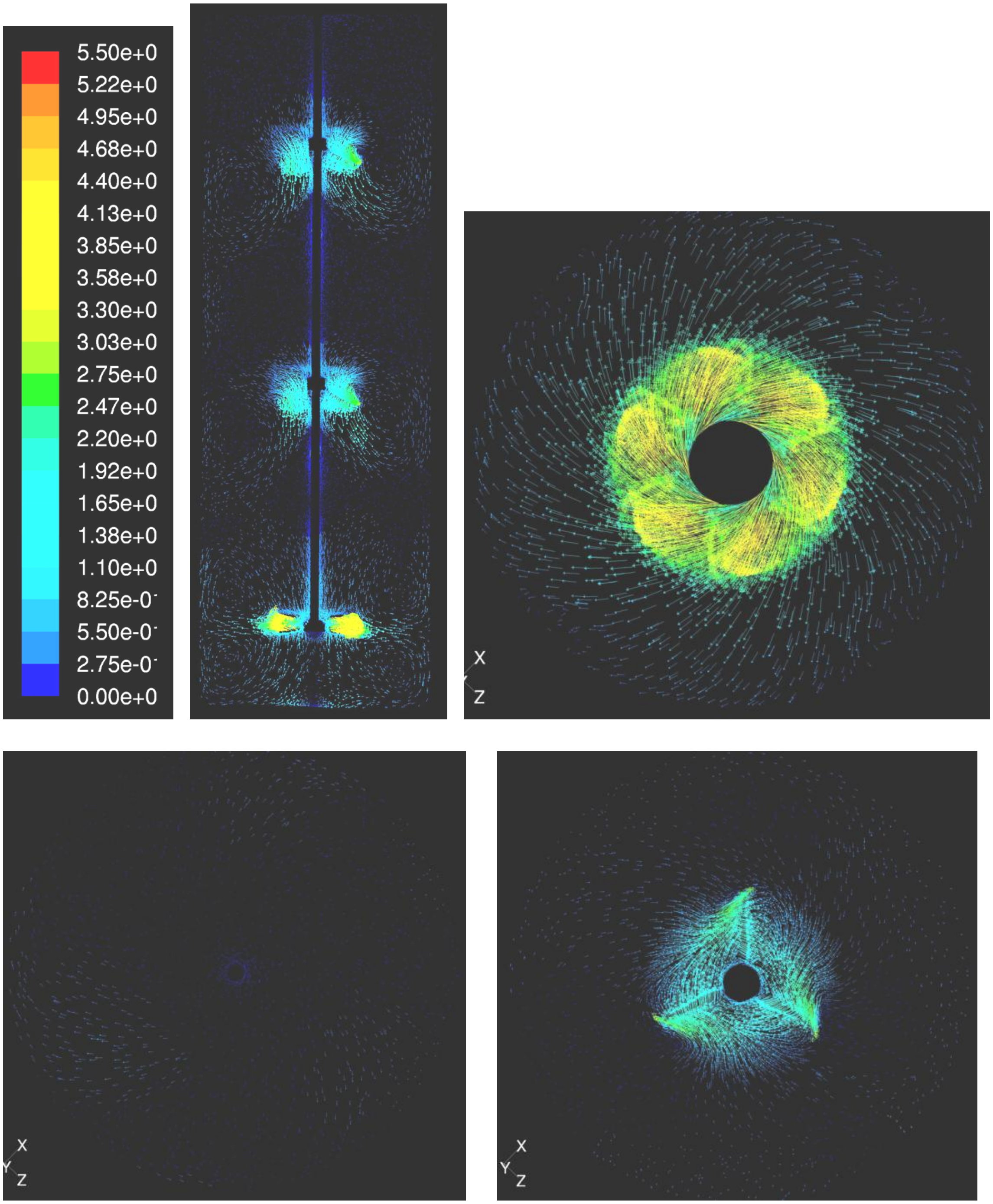

Impeller Configuration	Impeller Diameter (in)	Baffle Type	Mixing Time (sec.)
Rushton	6.0	Flat	7.9
Rushton	6.0		
Rushton	6.0		

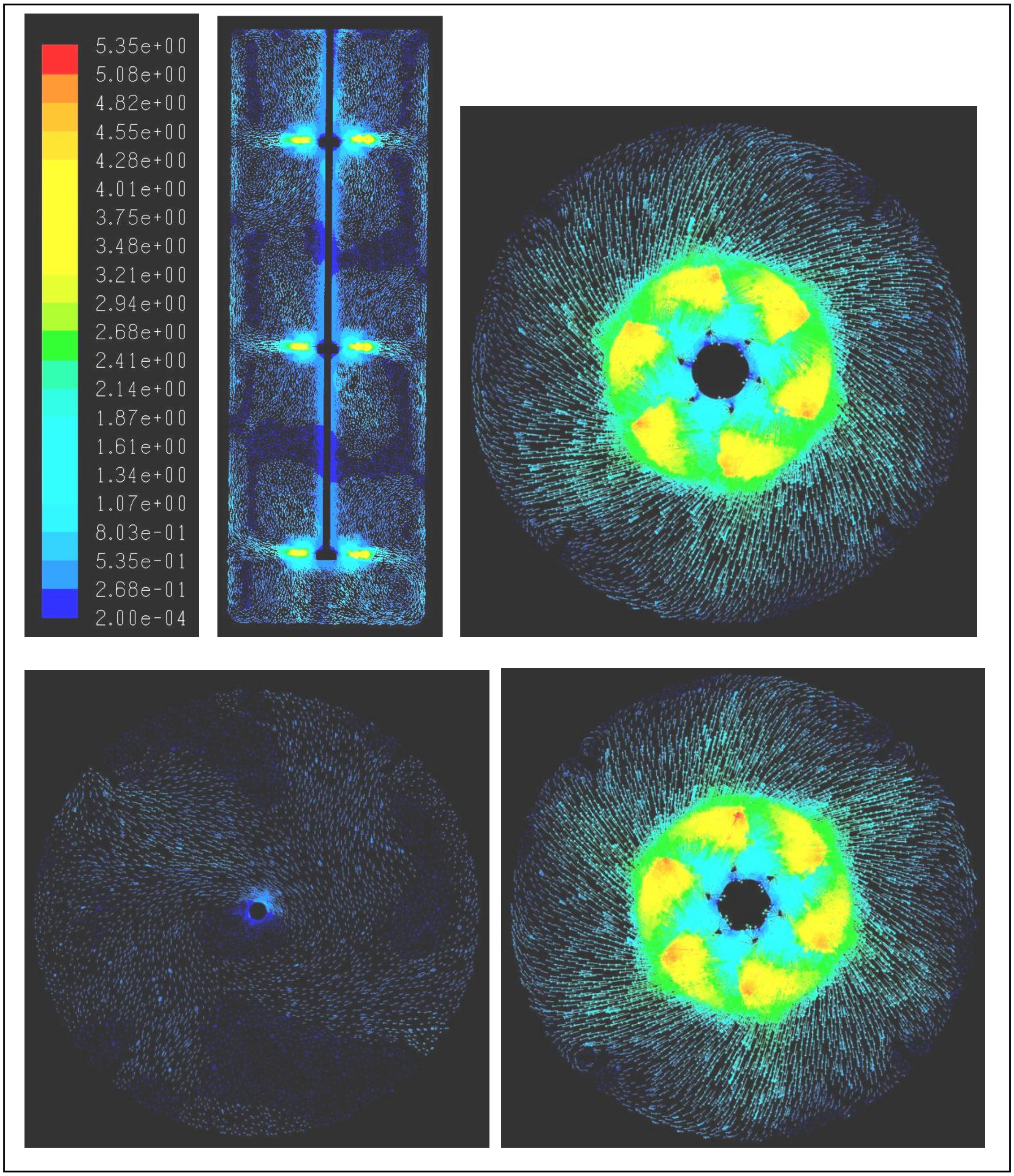

Impeller Configuration	Impeller Diameter (in)	Baffle Type	Mixing Time (sec.)
Rushton	6.0	1.5” Semi-circle	5.5
Rushton	6.0		
Rushton	6.0		

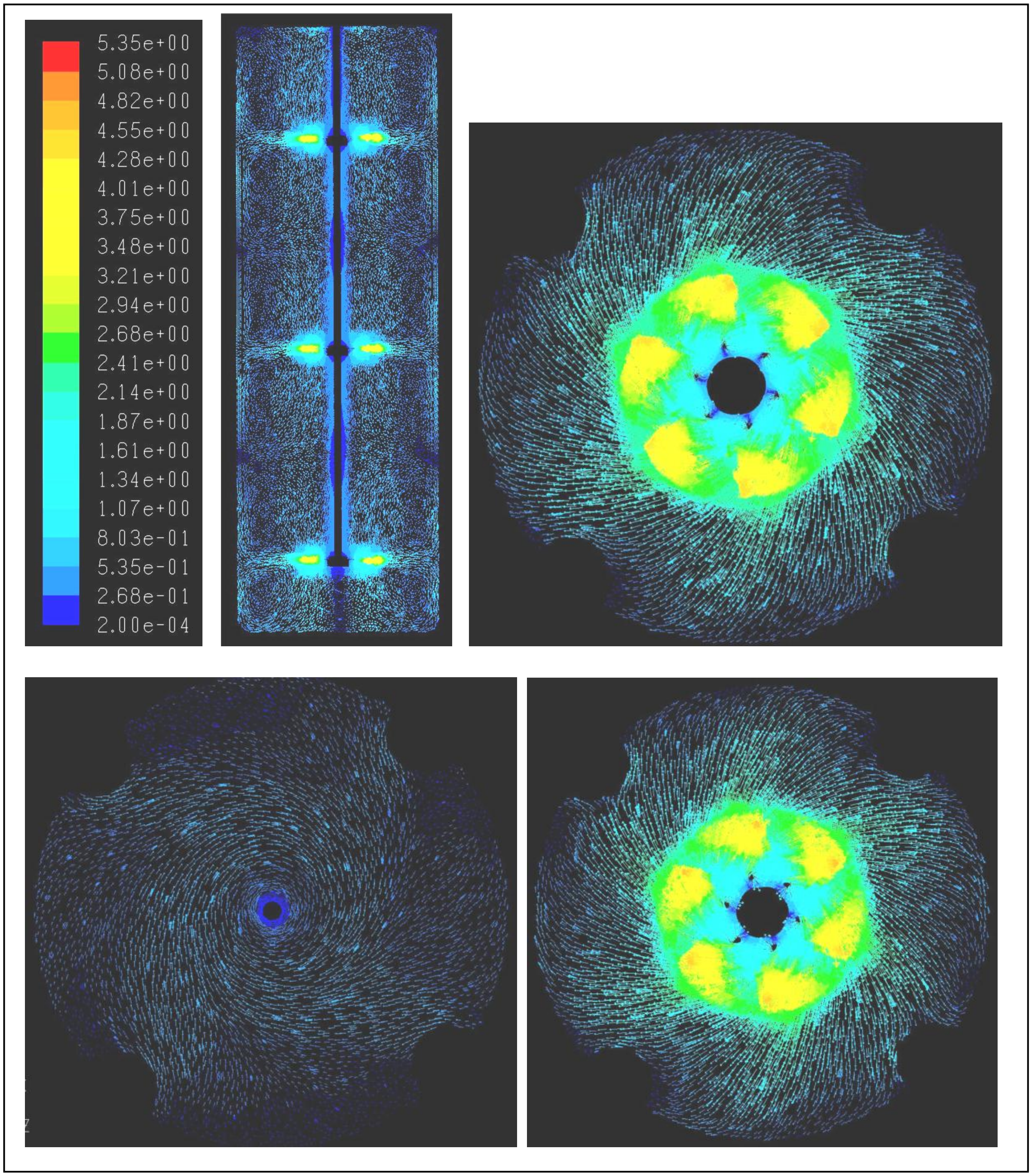

Impeller Configuration	Impeller Diameter (in)	Baffle Type	Mixing Time (sec.)
Rushton	6.0	0.75” Semi-circle	6.9
Rushton	6.0		
Rushton	6.0		

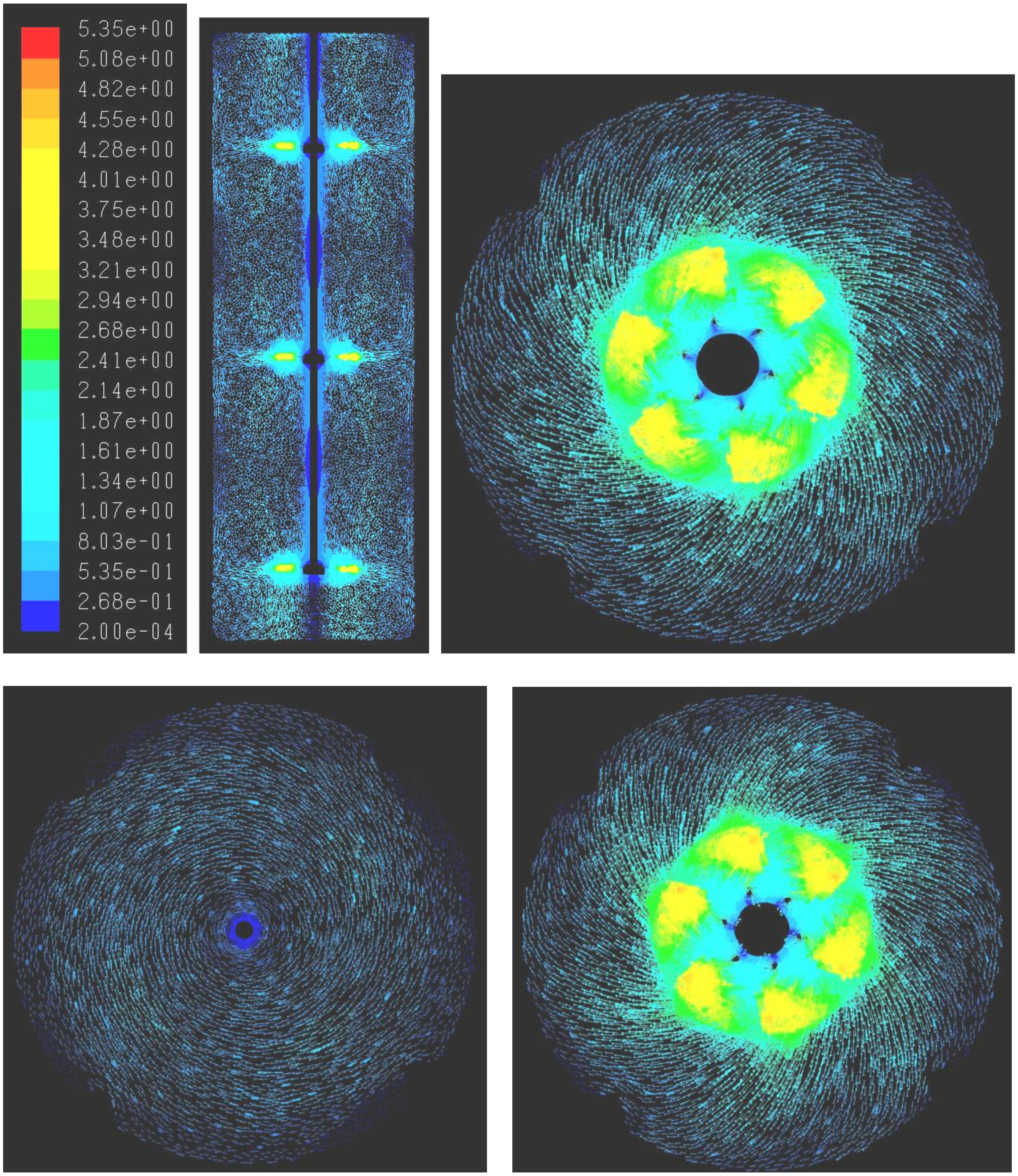

Impeller Configuration	Impeller Diameter (in)	Baffle Type	Mixing Time (sec.)
Rushton	6.0	Flat	6.8
Rushton	6.0		
Rushton	6.0		
Rushton	6.0		

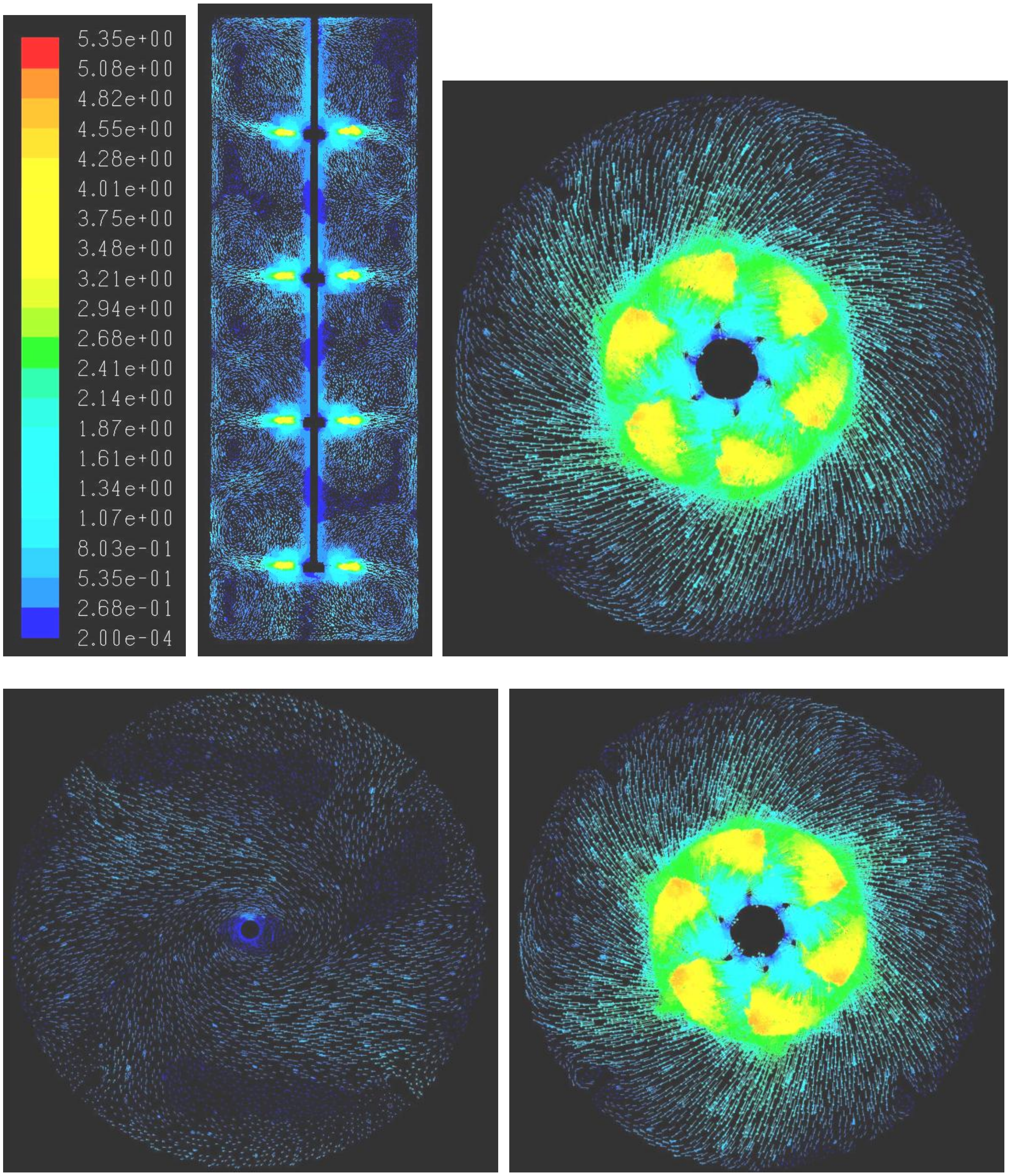

Impeller Configuration	Impeller Diameter (in)	Baffle Type	Mixing Time (sec.)
Rushton	6.0	Plastic Film	8.3
Rushton	6.0		
Rushton	6.0		
Rushton	6.0		

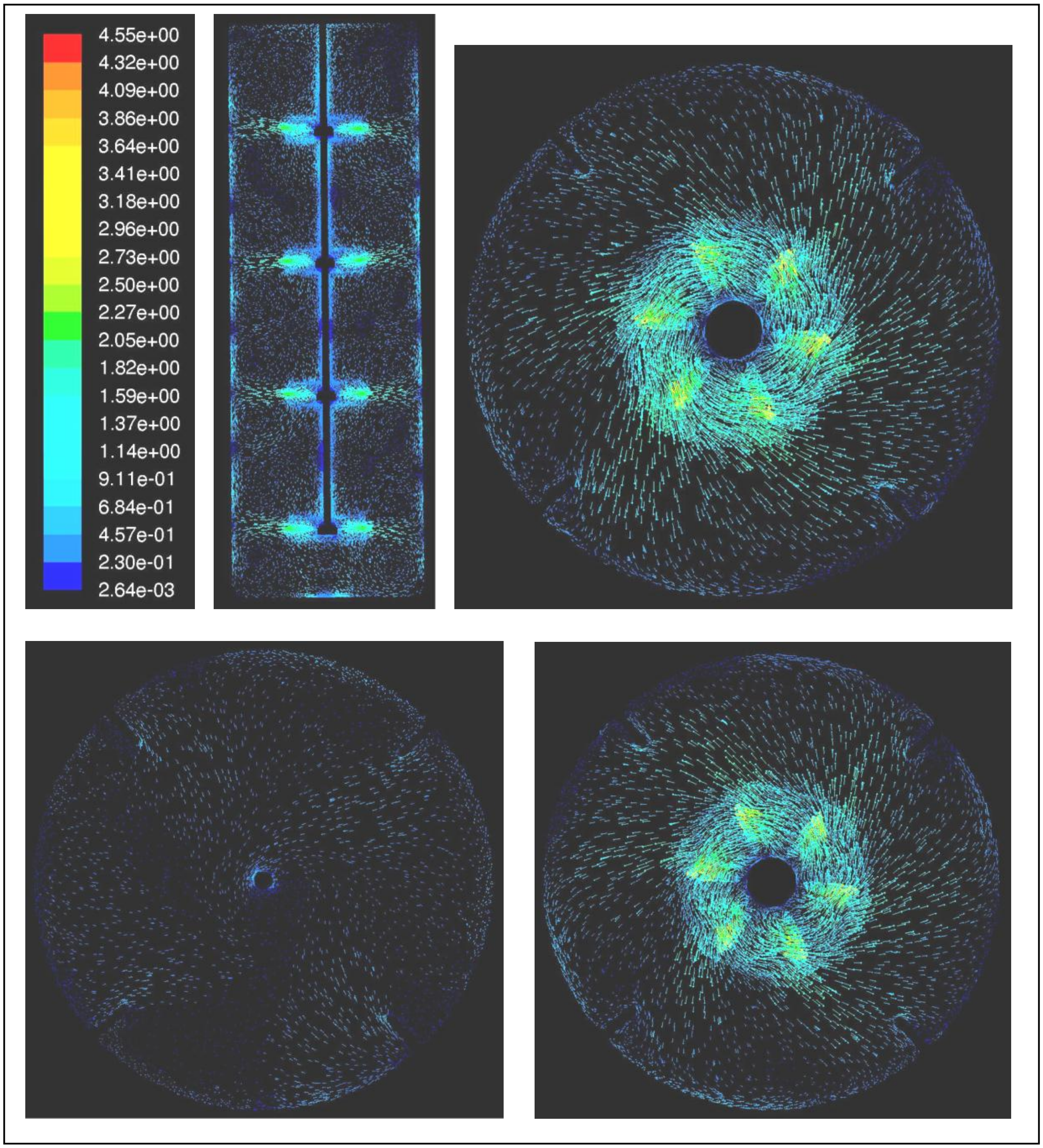

Impeller Configuration	Impeller Diameter (in)	Baffle Type	Mixing Time (sec.)
Smith	6.25	Flat	11.6
Smith	6.25		
Smith	6.25		
Smith	6.25		

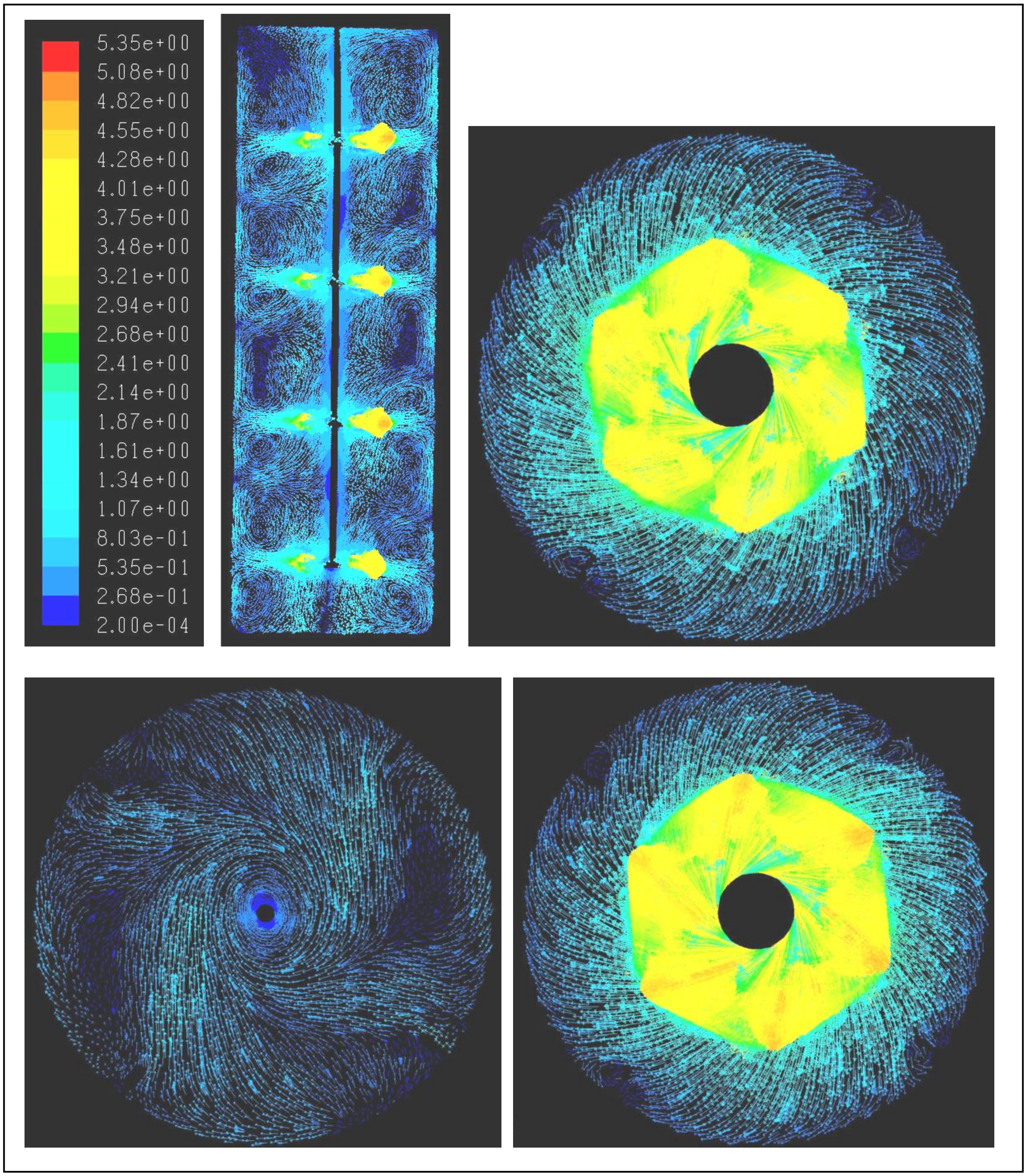

Impeller Configuration	Impeller Diameter (in)	Baffle Type	Mixing Time (sec.)
Smith	6.25	1.5” Semi-circle	6.6
Smith	6.25		
Smith	6.25		
Smith	6.25		

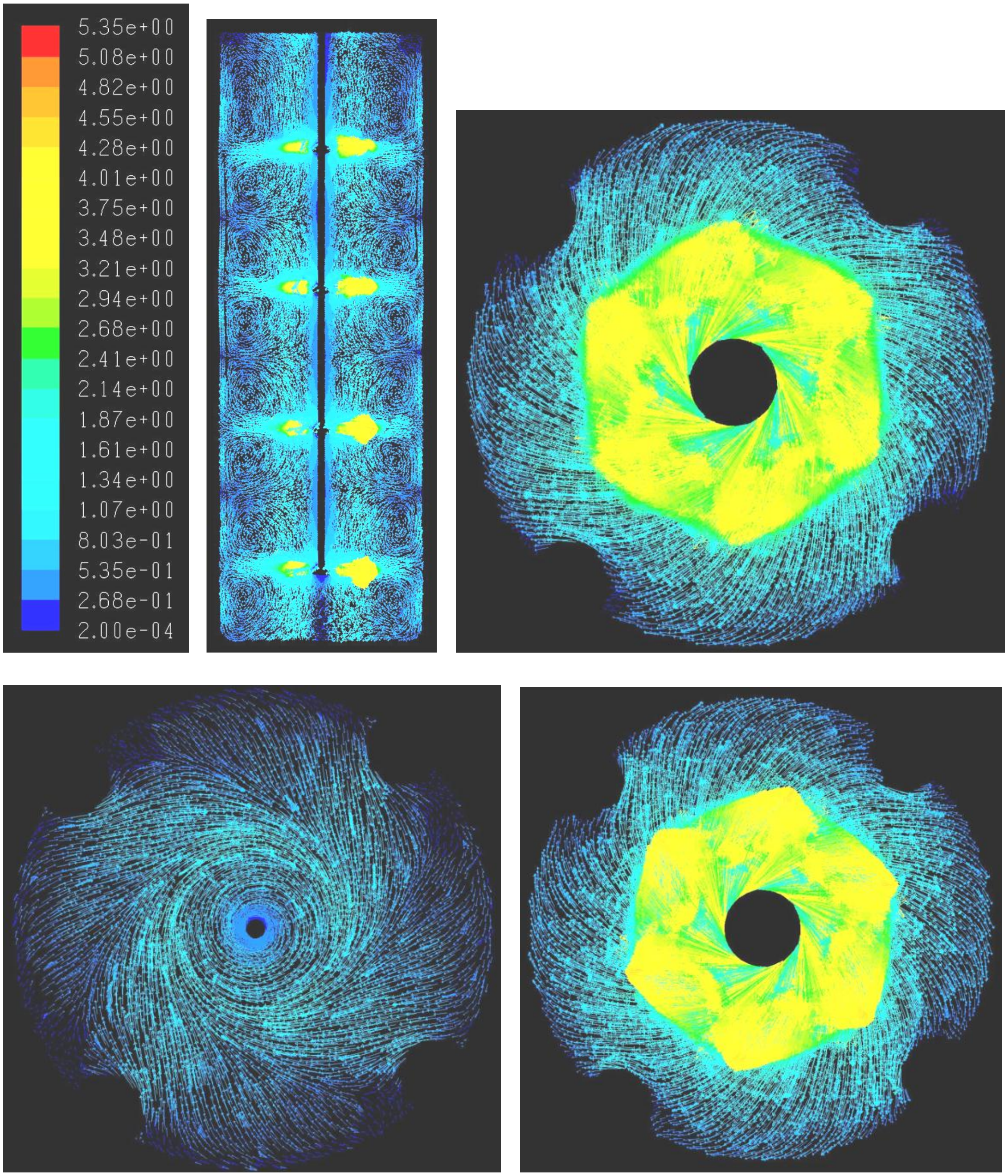

Impeller Configuration	Impeller Diameter (in)	Baffle Type	Mixing Time (sec.)
He3	6.0	Flat	9.9
Rushton	6.0		
Rushton	6.0		
Rushton	6.0		

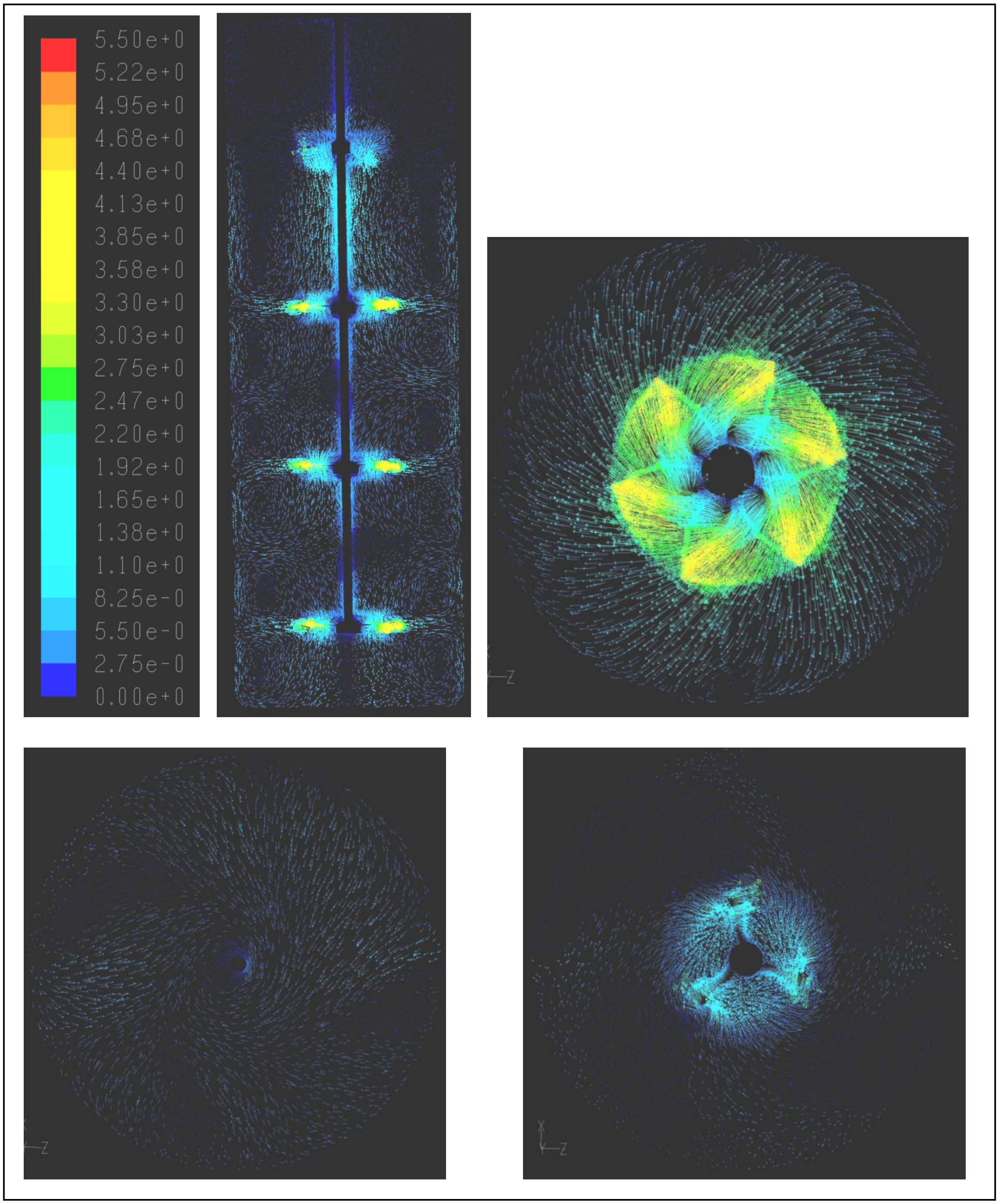

Impeller Configuration	Impeller Diameter (in)	Baffle Type	Mixing Time (sec.)
He3	6.0	Flat	15.8
He3	6.0		
Rushton	6.0		
Rushton	6.0		

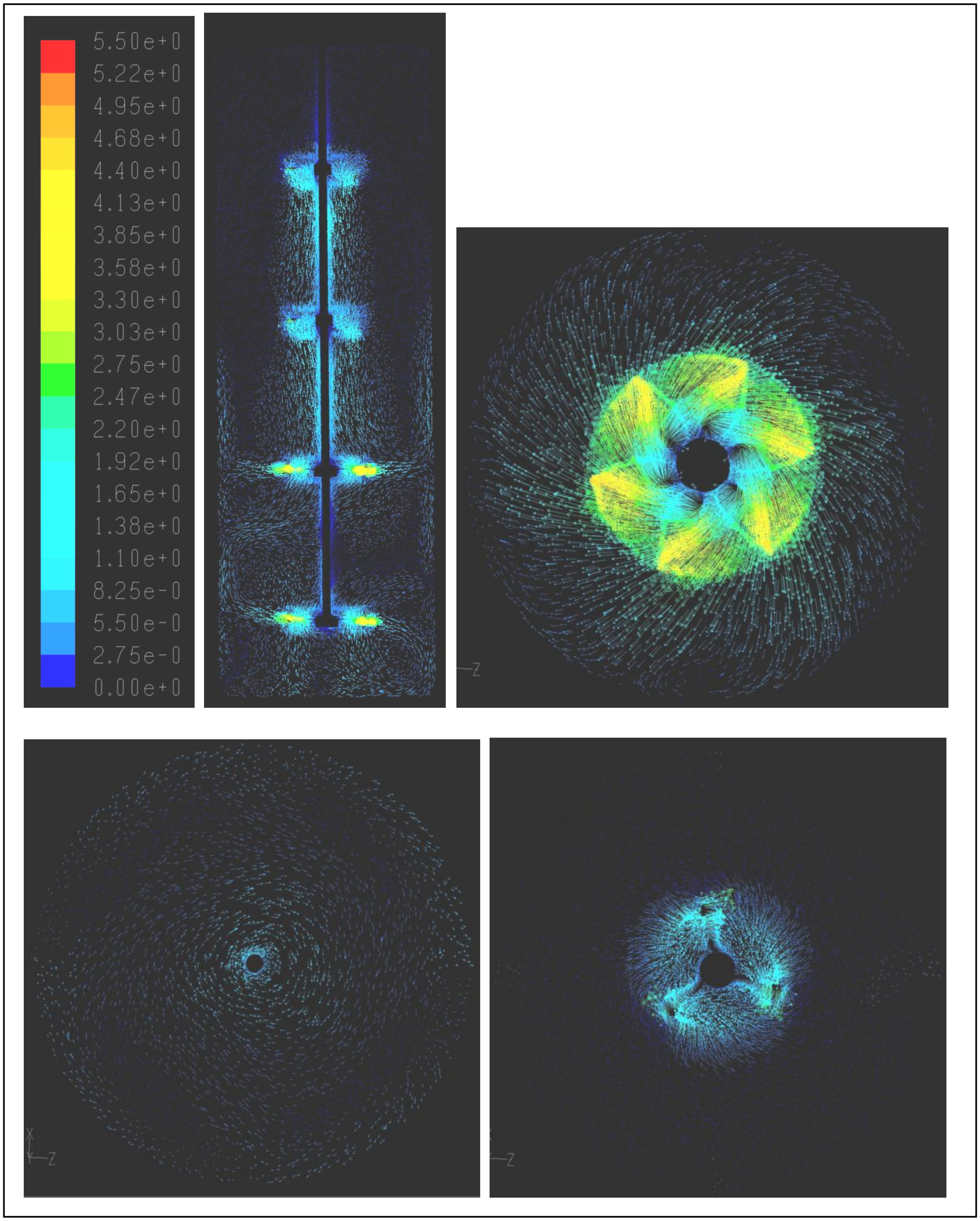

Impeller Configuration	Impeller Diameter (in)	Baffle Type	Mixing Time (sec.)
He3 Smith Smith Smith	6.0 6.25 6.25 6.25	Flat	10.5

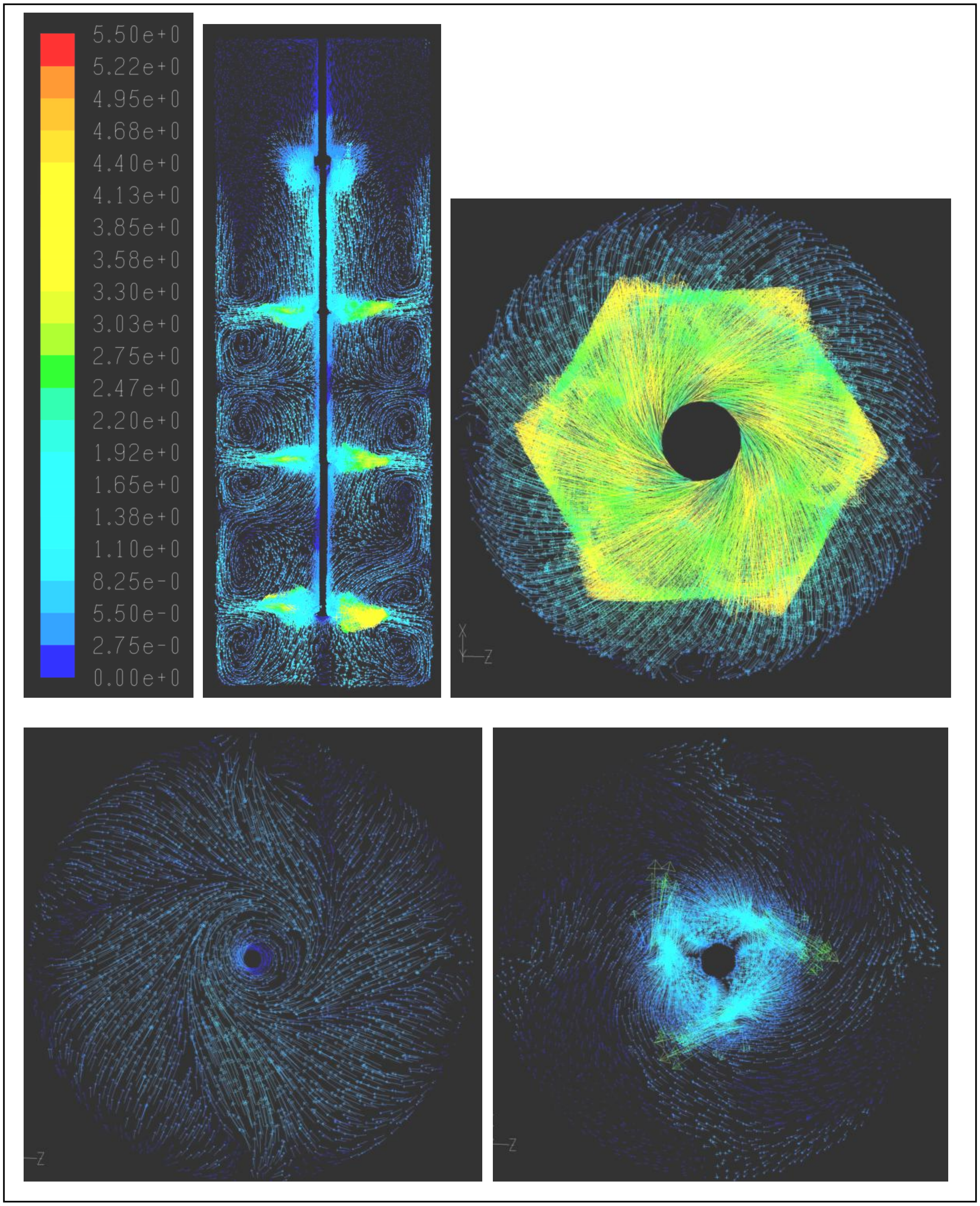

Impeller Configuration	Impeller Diameter (in)	Baffle Type	Mixing Time (sec.)
He3	6.25	Flat	12.1
He3	6.25		
Smith	6.25		
Smith	6.25